Observation of Coherence in the Photosystem II Reaction Center and Chlorophyll a

by

Servet Seckin Senlik

A dissertation submitted in partial fulfillment
of the requirements for the degree of
Doctor of Philosophy
(Physics)
in the University of Michigan
2016

Doctoral Committee:

Associate Professor Jennifer P. Ogilvie, Chair
Professor Eitan Geva
Associate Professor Kevin J. Kubarych
Professor Cagliyan Kurdak
Professor Roseanne J. Sension

2016

For my wife, Ozlem

ACKNOWLEDGEMENTS

I would like to acknowledge everyone who helped me to thrive both academically and personally. I am indebted to my advisor, Prof. Jennifer Ogilvie, for her excellent guidance, positive attitude and patience throughout my time in University of Michigan. She has provided interesting/challenging research problems and insightful discussions about them. I have benefited not only from her academic side, but also from the way she leads a research group. She cares about her students, knows that there is a life outside of the lab and keeps the group spirit high.

I would also like to thank Prof. Eitan Geva, Prof. Kevin Kubarych, Prof. Cagliyan Kurdak and Prof. Roseanne Sension for serving as my committee members and their contributions. I would like to give special thanks to Prof. Cagliyan Kurdak for his availability and willingness for the casual discussions we had about a variety of topics ranging from academic life to summers in Turkey over a cup of coffee.

I would like to thank all the past and present members of the Ogilvie group: Daniel, Frank, Veronica, Andy, Anton, Yassel, Libby, Vivek, Orko, Ying, Riley, Jie, Amar, Dan, Meredith who helped me in many ways both inside and outside of the lab. Daniel and Frank were the senior students when I joined the group and their generosity of sharing their knowledge helped me to understand field in depth and navigate through it quickly. Veronica and I worked together in several projects, and she was such a teammate whom everyone want to work with. Her commitment to the work done was distinctive. In particular, I wish to thank her for her contribution to developing the new methods described in this thesis. I felt very luck to be in the same group with Andy and Anton whenever I used a software/hardware developed by them. Their improvements and willingness for helping in several technical issues made my lab life easier. Although I didn't have an opportunity to work with Libby and Yassel, their tricky questions kept me awake about the fundamentals of the field all the time. My office mates and Dr. side of lab (Vivek, Orko, Ying); I'm very happy to get to know them. Given the limited time we spent in the group together, I appreciate the knowledge

and spirit they brought to lab and office. Yassel, Veronica, Libby, Andy, and Anton were amazing travel mates during our camping trip, which really makes the most joyous part of my time in the Ogilvie Group.

I would like to acknowledge the staff of Physics Department and Graduate School for their invaluable support and assistance, which made my graduate life vastly easier.

I would like to thank Prof. Kenan Gundogdu for his continuous support and motivational talks. He was the first one I knew in the field and showed me how ultrafast spectroscopy could offer the challenges I was looking for and fulfill my scientific curiosity. I would like to thank Prof. Nejat Seyhun for his guidance in my short finance studies to fulfill my curiosity and for giving a project opportunity in the finance field.

Several people I have met during six years in Ann Arbor gave an opportunity to explore my other side. My childhood dreams came true with Group Heritage (Hakan, Emin, Alex, Igor, Yavuzhan, Suleyman). I was the vocal of the group and gave mini-concerts across Michigan. I should admit that being on stage was giving as much fun as running experiments in the lab. I feel very lucky to get to know Mozaik Dance Group (Nilufer, Tayfun, Erdem, Claudia, Ozgun, Hurol, Nesrin, Evrim, Burcin, Ibrahim, Gulen, Arda) for their friendship and learning Artvin Horonu with them. Thank you all Group Heritage and Mozaik Dance Group members. I also thank Tayfun for answering my endless questions about Hittites without loosing his patience.

Sedat Ballikaya has been a great experimental physicist and great friend for several years. I will miss our lunch and coffee breaks around the Randall building. I hope that our friendship will continue to grow. Yassel has been an amazing friend and conference roommate. I wish we had more time to hangout in Ann Arbor, hopefully our paths will cross again.

Ridvan, Mehmet Can, Nisar, Ziah, Alpay, Ahmet, Ibrahim, Mehmet, Alparslan, Vusal, Yasin have been supportive friends since we first met in Ann Arbor. I hope that our friendship will continue to grow. I also thank Ridvan, who was my roommate for several years, for all the endless arguments, joyful trips, and enormous knowledge on technology.

Mustafa, my childhood friend, and his family (F249) have been very supportive since my first

day in Bilkent University. I wish to give my special thanks to them.

Tuncay Ozel, Ahmet Keles, Samed Yumrukcu, and Esat Kondakci have been eminent friends since our undergraduate years in Bilkent University. Their friendship and support since then continued growing and gave me immense comfort throughout my graduate studies. I am especially grateful to Tuncay for his very sincere friendship and sharing his thoughts honestly about both personal and professional issues.

I'm grateful to have a supportive family. My father, brother, parents-in law, aunts, sister-in law, brother-in law, cousins, uncles were always a phone call away and supported me through my PhD.

Finally, I would like to thank my wife, Ozlem, for all the things she brought to my life. I dedicate this thesis to her in our tenth anniversary.

TABLE OF CONTENTS

LIST OF FIGURES

LIST OF TABLES

LIST OF ABBREVIATIONS

2DES Two Dimensional Electronic Spectroscopy

BBO β-barium borate

BRC Bacterial Reaction Center

CCD Charge Coupled Device

Chl a Chlorophyll a

DO Diffractive Optics

DOPA Degenerate Optical Parametric Amplifier

ESA Excited State Absorption

GSB Ground State Bleach

LO Local Oscillator

NOPA Noncollinear Optical Parametric Amplifier

PSI Photosystem I

PSII Photosystem II

PSII RC Photosystem II Reaction Center

SE Stimulated Emission

SI Spectral Interferometry

TA Transient Absorption

TG Transient Grating

TRF Time Resolved Fluorescence

ABSTRACT

Observation of Coherence in the Photosystem II Reaction Center and Chlorophyll a

Chair: Jennifer P. Ogilvie

Oxygenic photosynthesis powers life on Earth by converting solar energy into chemical energy. The primary conversion steps occur in the photosystem II reaction center (PSII RC). Although the PSII RC has been studied by a wide variety of spectroscopic techniques, its design principles are not yet fully understood. In particular open questions remain about its electronic structure and the charge separation mechanism.

Two dimensional electronic spectroscopy (2DES) is a powerful method for investigating the electronic structure of photosynthetic systems. 2DES has improved our ability to excite and observe coherent dynamics in a wide range of systems. Observation of coherent dynamics in photosynthetic systems have generated considerable debate about their physical origin and possible functional relevance. Coherent dynamics in the PSII RC have been observed to persist on a similar timescale to charge separation. The coherences are believed to reflect electronic/vibrational resonances that may be important for charge separation. This thesis aims to understand the physical origin of the coherent dynamics in the PSII RC by comparison studies with the chlorophyll a monomer. In both the PSII RC and chlorophyll a we use 2DES to determine the spectroscopic signatures of the coherent dynamics of several modes. We compare these with the expected signatures within several simple models. We find that the PSII RC can be well described by a vibronic model and chlorophyll a shows deviations from the simple displaced harmonic oscillator.

In an effort to probe the functional importance of the coherent dynamics we seek evidence for coherent dynamics in the production of the charge separated state, probed in the near-infrared anion band region. The spectroscopic signals in this band region are weak, necessitating the development of a more sensitive approach to detecting coherent dynamics. To solve this problem, we have developed an alternative method, called two-color rapid acquisition coherence spectroscopy (T-

RACS). We have applied this method to chlorophyll a and showed dramatic increase in signal to noise and decrease in total experiment time compared to typical 2DES measurements. We demonstrate that T-RACS can distinguish between ground and excited state coherent dynamics, and provide high frequency resolution of the coherent dynamics.

To address the role of coherent dynamics observed in the PSII RC, we have utilized T-RACS to investigate the 790-820 nm region which has anion band markers for charge separation. The kinetics we observe in this region are inconsistent with previous reports using transient absorption spectroscopy with an 820 nm probe. We attribute the discrepancy to the high pulse energies used in the previous experiments. Here, we report observation of coherent dynamics in the 790-820nm spectral region, but require further studies to resolve the anion band contribution and to probe the functional significance of these coherent process.

Chapter 1

Introduction

1.1 Introduction

Photosynthesis is a biological process in which radiant energy from the Sun is converted to biochemical energy in a series of complex events [1]. Plants and many other primary producer organisms of the food chain utilize photosynthesis to generate energy to fuel their vital activities. In turn, a biomass of ~100 billion tons is produced annually, powering the life on Earth [2]. The pause of photosynthesis could severely affect the life on the Earth. For example, the collapse of a massive asteroid ~66 millions years ago hindered photosynthesis and cut the main power line to the Earth, triggering the extinction of dinosaurs and many other species [1].

As humankind pushes the limits of technology and the accessibility to technology increases, the worldwide demand for the energy increases as well. Today, the energy demand is still primarily met by fossil fuels either by their direct use or generating electricity from them. However, consumption of them comes with its own costs, e.g. major environmental problems. For example, when they are burned, the release of CO_2 into the atmosphere causes thickening of the greenhouse gas layer and induces climate change [3]. In addition, their fluctuating prices can destabilize economies, making fossil fuels less than ideal as an energy source. These problems and many more motivate the search and the development of renewable and more ideal energy sources. Sunlight is the most sustainable renewable energy source providing power of ~120000 TW at the Earth's surface, making solar cells an attractive option that is becoming widely adopted [4, 5]. However, efficiently capturing

and storing solar energy by solar cells remains a technical challenge. A recent study compared the solar energy conversion process performed in photosythesis and solar cells, showing that while the overall efficiency of photosynthesis is lower, the quantum efficiency of the initial charge separation steps, defined as the percentage of absorbed photons that give rise to stable photoproducts, is ~100% which is significantly higher than that of solar cells [6, 7]. This remarkably efficient process observed in photosynthesis motivates further research to uncover design principles of photosynthesis. In turn, this knowledge can be translated to improve the performance of solar cells. One should note that improving the overall efficiency of the photosynthesis is not the only major goal for a photosynthetic organism that must reproduce and perform photosynthesis under a wide variety of environmental conditions. Photosynthetic organisms have evolved to respond to a large number of evolutionary processes concurrently.

Photosynthesis is divided into two main categories: oxygenic and anoxygenic photosynthesis. Anoxygenic photosythesis, which doesn't involve oxygen release, is performed by several groups of bacteria: the green sulfur bacteria, the green nonsulfur bacteria, the heliobacteria, and the purple bacteria [1]. Most plants, algae and cyanobacteria perform oxygenic photosythesis in which carbon dioxide (CO_2) and water (H_2O) are used to convert solar energy into chemical energy while oxygen is released as a by-product.

In higher plants, photosynthesis takes place in organelles called chloroplasts. Chloroplasts have an oval shape with a diameter of ~5-8 μm diameter and a thickness of ~1-3 μm, and their number varies between ~10-100 within a cell [8]. They are enclosed with a membrane and filled with stromal fluid. In the stromal fluid, chloroplasts contain a network of nested membranes called thylakoids which have two different types: the grana thylakoids and the stroma thylakoids. Figure 1.1 shows a schematic illustration of a chloroplast with thylakoids. The grana thylakoids are closely spaced and form stacks while the stroma thylakoids connect theses stacks forming the network. These are binding sites for protein-pigment complexes which function in early light dependent reactions and energy conversion processes in photosynthesis. In addition, the nested structure of thylakoids gives rise to an increase in their surface to volume ratio, thereby increasing the amount

of absorbed radiant energy.

Figure 1.2 shows a schematic illustration of a subset of protein-pigment complexes which are bound to thylakoids. Together they form the photosynthetic machinery performing oxygenic photosynthesis with two distinct phases: the light dependent reactions and the dark reactions. The light dependent reactions performed collaboratively by the Photosystem II (PSII), the plastoquinone (PQ), the b_6f cytochrome, plastocyanin (PC) and the Photosystem I (PSI) have three phases: 1. Light absorption and funneling to reaction centers, 2. Primary electron transfer in the reaction centers, and 3. Energy stabilization. The dark reactions are the final steps where the solar energy energy is stored as chemical energy [1]. PSI was discovered first and has been named as the first photosystem. However PSII is responsible for the early light dependent reactions which are the main focus of this thesis.

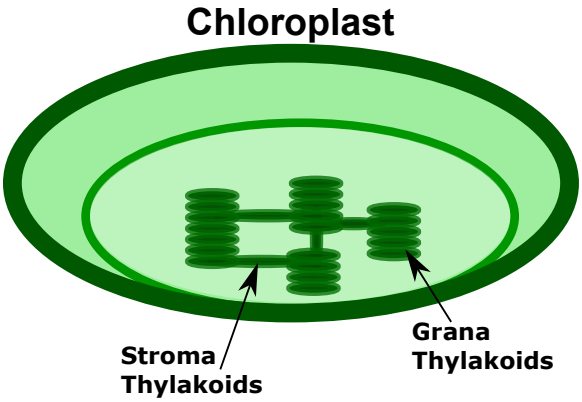

Figure 1.1: A schematic illustration of a chloroplast. The grana and the stroma thylakoids inside the chloroplast are shown. Adapted from [9].

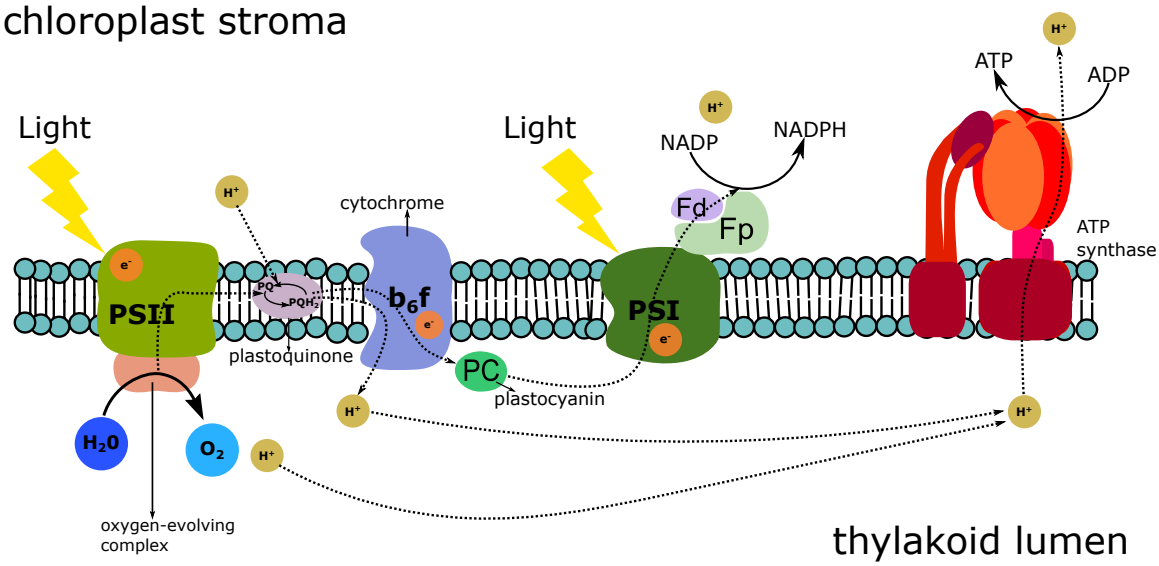

Figure 1.2: A schematic illustration of a subset of Thylakoid protein-pigment complexes: Photosystem II (PSII), Plastoquinone (PQ), Cytochrome b6f complex (Cytb6f), Plastocyanin (PC), Photosystem I(PSI). Graphical representation of protein functions are also shown. Adapted from [10].

1.2 PSII Structure and Function

PSII is a unique protein-pigment complex that converts solar energy to a charge separated state and releases oxygen by oxidizing water. PSII is a trans-membrane protein, located within the thylakoid membrane. PSII consists of a number of major components: CP43 and CP47 antenna proteins, D1 and D2 subunit protein domains that house the reaction center pigments, Cytochrome b559 (Cytb559) and oxygen evolving complex (OEC). In the following, I will discuss the initial phases of photosynthesis to illustrate the significance and functionality of PSII.

Photosynthesis begins with the absorption of sunlight by the light harvesting complex II (LHCII) which is the primary antenna protein complex in higher plants. The absorbed photon creates an excited state that eventually evolves to lower energy states in LHCII. The excitation energy is then transferred to CP43 and CP47 antenna proteins which are closer to the reaction center. After the transfer of energy to D1 and D2 subunits (the main constituents of the reaction center), a series of complex events takes place in the reaction center, and finally creates a charge separated state with a plastoquinone molecule (PQ) being the final electron acceptor. When the plastoquinone molecule is reduced twice, it gets two H^+ (protons) from the stroma, thereby forming plastoquinol (PQH_2). Next, it transports the protons to the thykaloid lumen, while the electrons are passed to cytochrome b6f to continue in the electron transport chain. Simultaneously, following the double reduction of the plastoquinone, the OEC splits water and releases the protons and electrons. The electrons extracted from water splitting are passed to the PSI where $NADP^+$ is converted to NADPH. The proton gradient across the membrane induces a pH gradient which enables ATP synthesis. Finally, through a series of dark reactions, NADPH and ATP are used to convert carbon dioxide to sugar as the final energy storage site.

Within PSII, the photosystem II reaction center (PSII RC) is the single site which is responsible for converting photon energy to a charge separated state which then drives the later stages of photosynthesis such as water splitting, electron transfer and the dark reactions. While the mechanism of photosynthesis has been studied for decades, our understanding of design principles governing the charge separation process in the PSII RC is incomplete. This thesis strives to explain aspects of the

early light dependent reactions taking place within the PSII RC. The following section discusses the structure and functionality of the PSII RC in detail.

1.2.1 PSII RC Structure

The PSII RC houses D1 and D2 protein subunits which together bind 6 chlorophyll a (Chl a) molecules, two pheophytin and two beta carotenes. Figure 1.3 shows the crystal structure of the pigments within the PSII RC. In the figure, each pigment is labeled with respect to the name of the protein to which it is bound (i.e. the last D_1/D_2 part of the labels refer to the subunits). The PSII RC is rotationally symmetric around a twofold axis separating the D1 and D2 subunits. The structure of the PSII RC is similar to its purple bacterial counterpart, the bacterial reaction center (BRC). Despite the two-fold symmetry, charge separation occurs along a single side; D1 side in the PSII RC. The most strongly interacting pair of pigments in the PSII RC are the PD_1 and PD_2 chlorophylls, with a small of inter-molecular distance of ~7 Angstrom [15]. Collectively they form a dimer of chlorophyll known as P680. This dimer is functionally very similar to the "special pair" found in BRCs. $ChlD_1$, $ChlD_2$, Chl_zD_1, and Chl_zD_2 are the other four chlorophylls and $PheoD_1$, $PheoD_2$ are the two pheophytins found in the PSII RC. In general, the pheophytin-a and the Chl a pigments have similar structures. The structure of Chl a is shown in Figure 1.4. Compared to Chl a, pheophytin-a lacks of the central Magnesium atom. Cytochrome b559, another important structure in the PSII RC, is a dimer which is composed of two subunits and a heme cofactor. While the function of Cytochrome b559 has not been fully understood yet, researchers have show that it is not involved in the primary charge separation steps. Its role in protecting the PSII RC against excessive radiant energy is still an area of active research [11, 12]. The PSII RC, which we studied in this work, is purified from the PSII complex following the preparation called d1d2-cyt.b559 [13] and is referred as the Photosystem II D1D2-cyt.b559 Reaction Center or D1D2-cyt.b559.

Among the PSII RC substructures, Chl a is the most abundant pigment in the PSII RCs within the oxygenic photoynthetic organisms. Chl a dominantly determines the spectral properties of the PSII RC, and it deserves to be explained in a separate section.

1.2.2 Chlorophyll a Structure and Spectral Signatures

The six Chl a and two pheophytin-a within the PSII RC are the main pigments which are involved in the conversion of photo excitation energy to charge separation. The chemical formula of Chl a is $C_{55}H_{72}N_4O_5Mg$, and its molecular structure is shown in Figure 1.4. It contains a Mg atom in the center which is surrounded by a chlorin ring and hydrocarbon tail attached to this ring. The Chl a absorption spectrum is dominated by two main absorption bands located in the blue region and the red region of the visible spectrum. The lack of any significant absorption in the wavelength range of ~500-580 nm makes Chl a look green.

A four orbital model can properly describe the spectral properties of Chl a [14]. The two highest occupied molecular orbitals and the two lowest unoccupied orbitals of the chlorin structure within the Chl a are responsible for the formation of the main absorption bands. The transitions with the two lowest energies are called as the Q_x and the Q_y transitions, whereas the highest energy transition is called the Soret band. The absorption peaks of the Soret, the Q_x, and the Q_y bands are located at ~420 nm, ~580 nm, and ~680 nm respectively. The strength of the transition dipole moments for the Soret and Q bands are different, as reflected in the linear absorption spectrum of Chl a at room temperature (Figure 1.5).

The Q_x and the Q_y terminology originates from the orientation of the Chl a molecule and the polarization of incoming light. The transition with the lowest energy is polarized along the y direction of the molecule, that is the absorption would be maximum if the polarization of incoming field is collinear with the y axis of the molecule [1]. The polarization of the Q_x band is not well understood yet while the Soret band exhibits mixed polarization. Figure 1.4 depicts the conventional coordinate system used to describe the Q_x and the Q_y transitions.

Another feature affecting the absorption spectrum is vibrational overtones which produce side peaks on the blue side of the strong absorption bands. These overtones arise from transitions from the lowest vibrational level on the ground electronic state to higher lying vibrational levels on the excited electronic state. This phenomenon, called vibrational progression, is strongly evident in the Q_y band [1].

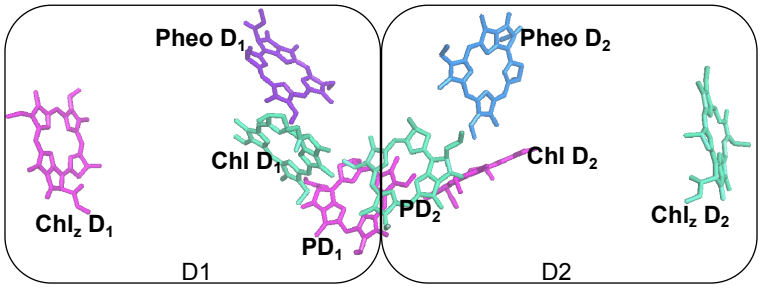

Figure 1.3: The crystal structure of the PSII RC. Two pheophytin and six chlorophyll are shown. Adapted from [15].

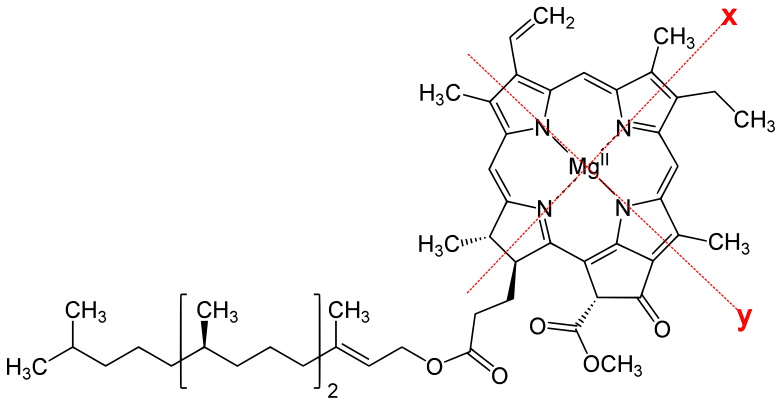

Figure 1.4: The molecular structure of Chl a and the conventional coordinate system to describe the Q_x and Q_y bands. Adapted from [16].

1.2.3 Spectral Signatures of The PSII RC

The spectral properties of the PSII RC are determined by its structure and the constituent pigments within it. In addition to the chlorophyll and pheophytin, with Soret (~420 nm), Q_x (~580 nm), and Q_y (~680 nm) bands, additional carotenoids also absorb in the visible range. Beta carotenes in the PSII RC absorb mainly in the ~400-550 nm making them appear orange. The inter-pigment distances within the PSII RC vary between ~7-70 Angstrom. This tight packing induces coupling between the electronic transitions of individual pigments, resulting in different absorption properties for the PSII RC than those of the individual pigments. Unlike in the case of the monomer, an absorption event in the PSII RC may create a delocalized excitation ("exciton") [17]. This phenomenon, which is described further in Chapter 3, gives rise to unique spectral properties of the PSII RC.

Figure 1.5 shows the absorption spectrum for the PSII RC at room temperature together with the Chl a absorption spectrum. The three absorption bands of Soret, Q_y and Pheophytin Q_x are present in the spectrum. The Q_y(~680 nm) is a widely studied feature as it has spectral signatures related to the charge separation and the energy transfer steps within photosynthesis. The Pheophytin Q_x band, (~544 nm), is an essential band for containing markers for the pheophytin excitation and pheophytin anion formation. Table 1.1 summarizes the absorption bands of the PSII RC observed in visible and near-IR range [18].

Table 1.1: Summary for Spectral Signatures in the PSII RC

PROBE WAVELENGTH (nm)	BAND NAME
400-450nm	Soret region
460nm	$P680^+$, Pheo a^- ion band
544nm	Pheo a Q_x band
660-690nm	Q_y band
735nm	Q_y stimulated emission band
790-820nm	$P680^+$ and Pheo a^- ion band

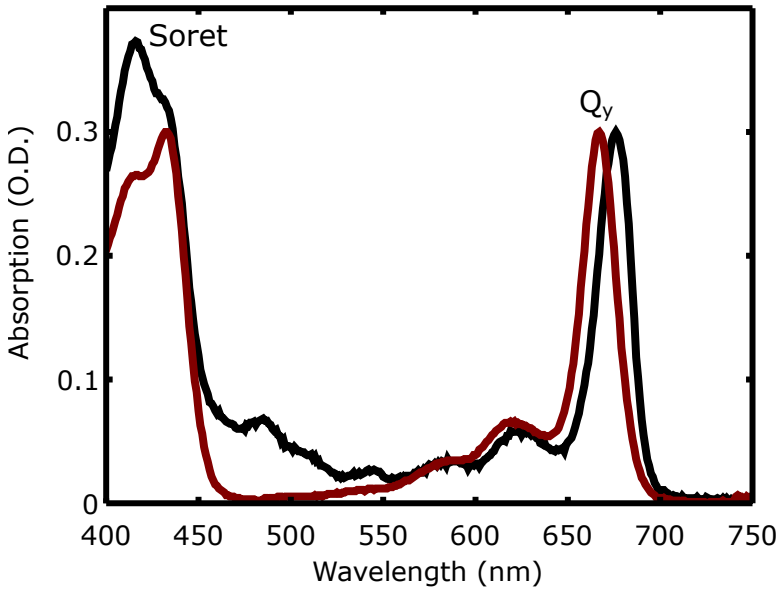

Figure 1.5: Absorption spectrum of Chl a(red) and the PSII RC(black) at room temperature.

1.3 Open Questions in the PSII RC

The PSII RC has been extensively studied utilizing ultrafast spectroscopic methods to probe the relationship between the molecular structure and its function. Particularly, understanding the charge separation pathways and mechanism attracted considerable attention. Time resolved spectroscopy experiments have led to several proposed charge separation mechanisms. The progress in this research area has been extensively reviewed by several researchers [18–20]. Herein, I discuss the time resolved fluorescence and the transient absorption measurements of the main bands of the PSII RC.

Early transient absorption studies of the Q_y band of the PSII RC have identified one ~20-25 ps slow component and ~3 ps fast component [21, 22]. The recent studies have reported the observation of multiple exponential components in the description of observed kinetics (~1.1-2 ps, ~20 ps, ~250 ps and ~nanosecond components) for the Q_y and other bands under several excitation conditions [23]. Time resolved fluorescence studies of the Q_y band reveal information about charge separation with probing the decay of the singlet states to the charge separated states. Studies using a streak camera for increased time resolution identified one 1.5 ps component along with another longer component [24]. Later studies have proposed that the charge separation occurs in $>$30 ps [25].

Transient absorption studies examining the Pheophytin Q_x band identified a ~20 ps component associated with the charge separation [26]. Subsequent studies have identified another component with ~3 ps in addition to the ~20 ps component [24, 27]. More recent studies have observed a ~17 ps component along with a ~3 ps faster component at 77 K [23].

Groot and coworkers identified mid-IR markers of charge separation, reporting a ~0.6-0.9 ps component [28]. Despite the extensive work, the models describing the charge separation pathways are still under question. The most extensive model that takes into account the broadest range of linear and nonlinear spectroscopic data is the two pathway model [23]. In the primary pathway, the initial charge separation occurs between the Chl_{D1} and Phe_{D1} pigments, prior to reaching to the final charge separated state [19, 29], $P^{+}_{D1}Phe^{-}_{D1}$ as shown in Equation 1.1a. In the second pathway

initial charge separation occurs between the P_{D1} and P_{D2} pigments as described by Equation 1.1b.

$$(Chl_{D1}Phe_{D1})^* = Chl^+_{D1}Phe^-_{D1} \longrightarrow P^+_{D1}Phe^-_{D1} \tag{1.1a}$$

$$(P_{D1}P_{D2}Chl_{D1})^* = P^-_{D1}P^+_{D2} \longrightarrow P^+_{D1}Chl^-_{D1} \longrightarrow P^+_{D1}Phe^-_{D1} \tag{1.1b}$$

Figure 1.6 shows the two pathways for the charge separation discussed above. In addition to the previous extensive efforts made to unveil the charge separation pathways in the PSII RC, further experimental and theoretical work remains to be done for a deeper understanding. For example, the anion bands, centered at ~460 nm and ~790-820 nm, involve markers for the charge separated state, and should be further investigated utilizing the new ultrafast spectroscopy methods which were unavailable when it was previously studied.

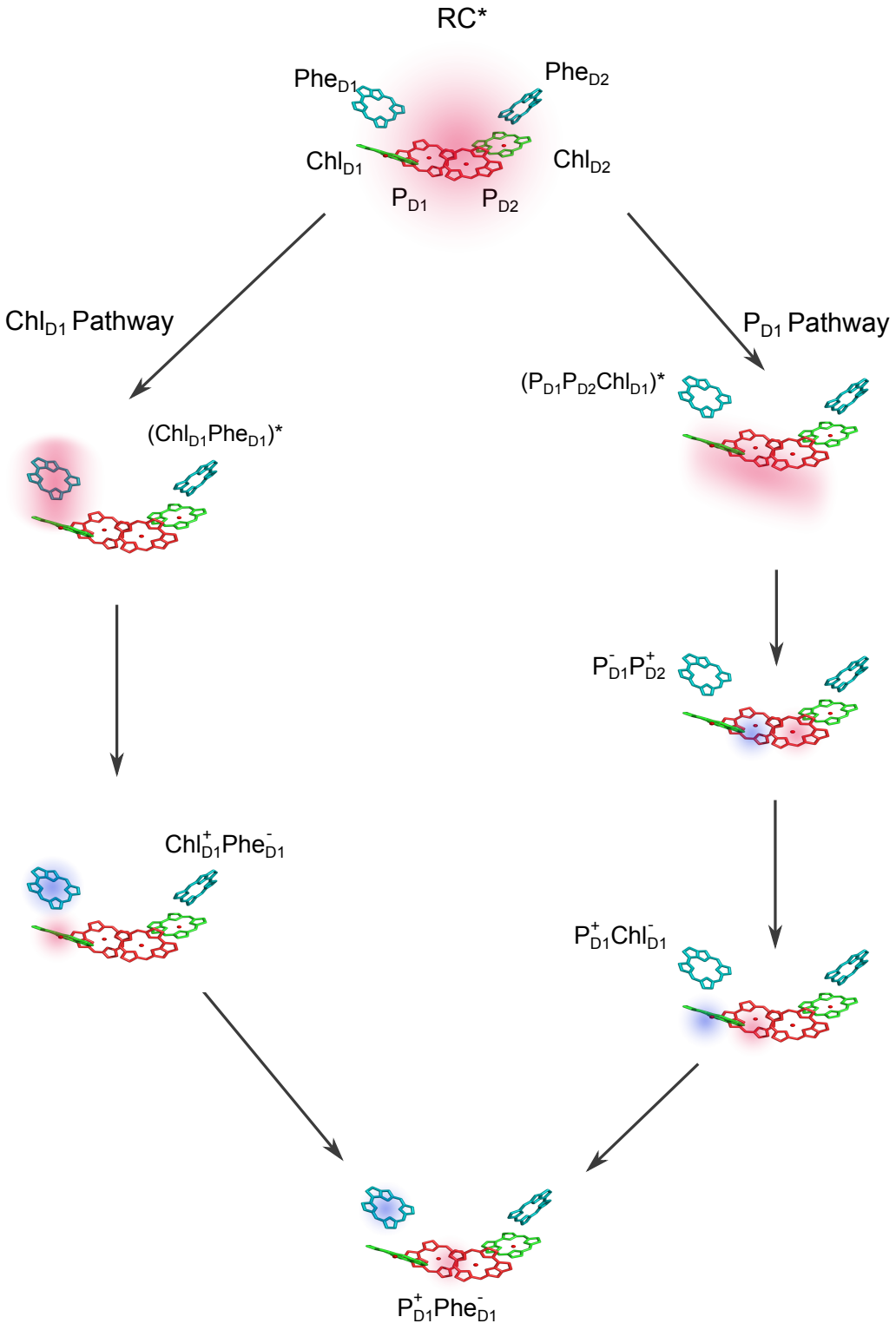

Figure 1.6: Two different pathways proposed for the primary charge separation. Adapted from [23]. (Courtesy of A.Loukianov)

1.4 Coherent Dynamics in the PSII RC

The understanding of how excitation energy flows within photosynthetic systems is of significant importance and has attracted considerable attention. Photosynthetic energy transfer was described by Forster theory [30] which was accurate up to a certain extent. In this approach, the excitations are assumed to be localized on each pigment within the photosynthetic apparatus, and the energy transfer occurs in the form of incoherent hopping from one pigment to another.

The enhancement of the ultrafast spectroscopic methods over the last two decades enabled the preparation of coherent states and the study of their dynamics. The spectral signatures of the coherent dynamics are the oscillations present in the amplitude of the spectroscopic signal, and they will be referred as "coherent dynamics" and "coherence" in short throughout this thesis. Coherent dynamics in photosynthetic systems have been seen to persist on a time scale that is comparable to the time spans of the energy and the charge transfer steps motivating the research for understanding their functionality and origin. According to current theories, the origin of these oscillations is either electronic (the coherence is between different excitonic electronic states), or vibrational (the coherence is between different vibrational states), or vibronic which is a mixture of the previous two.

Vos and coworkers first reported the observation of coherent dynamics in bacterial reaction centers (BRC) utilizing pump probe spectroscopy, and explained their origin as being vibrational [31–34]. The following studies of the same era verified their observation, and reported the existence of similar coherences [35–37]. These early works triggered many theoretical and experimental studies aiming to explain the functionality of these coherences [38–42].

Recent enhanced ultrafast spectroscopy methods have improved our ability to probe coherent dynamics. In 2007, Engel and coworkers were the first to report the existence of long lived coherences, which they identified as of electronic origin, in Fenna-Matthews-Olson complex utilizing two dimensional electronic spectroscopy(2DES) [43]. Their work demonstrated the capability and the strength of 2DES for identifying the signatures of coherent dynamics. The similarity between the timescales of coherent dynamics and the energy transfer steps also motivated considerable work

to explore their potential functionality. 2DES has now been used to observe coherent dynamics in a wide range of systems: Dye molecules and aggregates [44–48]. Photosynthetic antennae and reaction centers (including the PSII RC) [49–56]. Quantum dots and organic photovoltaic materials [57, 58]. In addition, many theoretical works have endeavored to describe the origin of these coherent dynamics and their potential functionality, which is still controversial [59–62].

Coherent dynamics in the PSII RC is the main focus of this thesis. An improved characterization of its coherent dynamics could enrich our understanding of inter and intra molecular coupling, charge separation, and energy transport within the PSII RC. This thesis compares the coherent dynamics observed in the Chl a and in the PSII RC in an effort to better understand the physical origin of the coherent dynamics. It also describes the development of a new spectroscopic method for rapid and high signal-to-noise observation of coherent dynamics. It then uses the new method to study coherent dynamics in the anion band in an effort to understand the functionality of the coherent dynamics in charge separation within the PSII RC.

1.5 Outline of Thesis

The remaining of this thesis is outlined as follows: Chapter 2 presents the theory of the 2DES and describes the experimental setup that we used to perform the 2DES measurements reported herein. Chapter 3 compares the coherent dynamics observed in the PSII RC and in Chl a. In Chapter 4, I report a new experimental method called two-color rapid data acquisition coherence spectroscopy (TRACS) which enables rapid and high signal-to-noise observation of coherent dynamics. We used Chl a to demonstrate the applicability and the capability of the method. Chapter 5 presents the TRACS studies and the transient absorption studies performed on the anion band of the PSII RC. Finally, Chapter 6 presents the summary of the work presented here and outlook for the next phase of the research.

References

[1] Robert E. Blankenship. *Molecular Mechanisms of Photosynthesis*, pages i–vii. Blackwell Science Ltd, (2008).

[2] Christopher B. Field, Michael J. Behrenfeld, James T. Randerson, and Paul Falkowski. Primary production of the biosphere: Integrating terrestrial and oceanic components. *Science*, **281**:237–240, (1998).

[3] M. I. Hoffert, K. Caldeira, G. Benford, D. R. Criswell, C. Green, H. Herzog, A. K. Jain, H. S. Kheshgi, K. S. Lackner, J. S. Lewis, H. D. Lightfoot, W. Manheimer, J. C. Mankins, M. E. Mauel, L. J. Perkins, M. E. Schlesinger, T. Volk, and T. M. L. Wigley. Advanced technology paths to global climate stability: Energy for a greenhouse planet. *Science*, **298**:981–987, (2002).

[4] Nathan S. Lewis and Daniel G. Nocera. Powering the planet: Chemical challenges in solar energy utilization. *Proceedings of the National Academy of Sciences of the United States of America*, **103**:15729–15735, (2006).

[5] James Barber. Photosynthetic energy conversion: natural and artificial. *Chemical Society Reviews*, **38**:185–196, (2009).

[6] Robert E. Blankenship, David M. Tiede, James Barber, Gary W. Brudvig, Graham Fleming, Maria Ghirardi, M. R. Gunner, Wolfgang Junge, David M. Kramer, Anastasios Melis, Thomas A. Moore, Christopher C. Moser, Daniel G. Nocera, Arthur J. Nozik, Donald R. Ort, William W. Parson, Roger C. Prince, and Richard T. Sayre. Comparing photosynthetic and photovoltaic efficiencies and recognizing the potential for improvement. *Science*, **332**: 805–809, (2011).

[7] C. A. Wraight and R. K. Clayton. The absolute quantum efficiency of bacteriochlorophyll photooxidation in reaction centres of rhodopseudomonas spheroides. *Biochimica Et Biophysica Acta*, **333**:246–260, (1974).

[8] Rob Phillips Ron Milo. *Cell Biology by the Numbers*. Garland Science Taylor and Francis Group, (2015).

[9] Public Domain. Thylakoid membrane of chloroplasts, (2009). URL `https://upload.wikimedia.org/wikipedia/commons/a/a6/Chloroplast_II.svg`.

[10] Public Domain. Thylakoid membrane of chloroplasts, (2009). URL `https://commons.wikimedia.org/wiki/File:Thylakoid_membrane.svg`.

[11] Hsiu-An Chu and Yi-Fang Chiu. The roles of cytochrome b(559) in assembly and photoprotection of photosystem ii revealed by site-directed mutagenesis studies. *Frontiers in Plant Science*, **6**:1261, (2015).

[12] Vincent P. McNamara, Fayyaz S. Sutterwala, Himadri B. Pakrasi, and John Whitmarsh. Structural model of cytochrome b(559) in photosystem ii based on a mutant with geneticallyfusedsubunits. *Proceedings of the National Academy of Sciences of the United States of America*, **94**:14173–14178, (1997).

[13] Peter J. Leeuwen, Maaike C. Nieveen, Erik Jan Meent, Jan P. Dekker, and Hans J. Gorkom. Rapid and simple isolation of pure photosystem ii core and reaction center particles from

spinach. *Photosynthesis Research*, **28**:149–153.

[14] Martin Gouterman. Spectra of porphyrins. *Journal of Molecular Spectroscopy*, **6**:138–163, (1961).

[15] Yasufumi Umena, Keisuke Kawakami, Jian-Ren Shen, and Nobuo Kamiya. Crystal structure of oxygen-evolving photosystem ii at a resolution of 1.9[thinsp]a. *Nature*, **473**:55–60, (2011).

[16] Public Domain. (2009).

[17] Leonas Valkunas Herbert van Amerongen, Rienk van Grondelle. *Photosynthetic Excitons*. WORLD SCIENTIFIC, (2011).

[18] Scott R. Greenfield and Michael R. Wasielewski. Excitation energy transfer and charge separation in the isolated photosystem ii reaction center. *Photosynthesis Research*, **48**:83–97, (1996).

[19] Ryszard Jankowiak. Probing electron-transfer times in photosynthetic reaction centers by hole-burning spectroscopy. *The Journal of Physical Chemistry Letters*, **3**:1684–1694, (2012).

[20] T. Renger and E. Schlodder. Primary photophysical processes in photosystem ii: bridging the gap between crystal structure and optical spectra. *Chemphyschem*, **11**:1141–53, (2010).

[21] M. R. Wasielewski, D. G. Johnson, M. Seibert, and Govindjee. Determination of the primary charge separation rate in isolated photosystem ii reaction centers with 500-fs time resolution. *Proc Natl Acad Sci U S A*, **86**:524–8, (1989).

[22] Thomas Rech, James R. Durrant, D. Melissa Joseph, James Barber, George Porter, and David R. Klug. Does slow energy transfer limit the observed time constant for radical pair formation in photosystem ii reaction centers? *Biochemistry*, **33**:14768–14774, (1994).

[23] Elisabet Romero, Ivo H. M. van Stokkum, Vladimir I. Novoderezhkin, Jan P. Dekker, and Rienk van Grondelle. Two different charge separation pathways in photosystem ii. *Biochemistry*, **49**:4300–4307, (2010).

[24] Brent Donovan, Larry A. Walker, Daniel Kaplan, Marcel Bouvier, Charles F. Yocum, and Roseanne J. Sension. Structure and function in the isolated reaction center complex of photosystem ii. 1. ultrafast fluorescence measurements of psii. *The Journal of Physical Chemistry B*, **101**:5232–5238, (1997).

[25] Laurie M. Yoder, Allwyn G. Cole, and Roseanne J. Sension. Structure and function in the isolated reaction center complex of photosystem ii: energy and charge transfer dynamics and mechanism. *Photosynthesis Research*, **72**:147–158, (2002).

[26] Gary Hastings, James R. Durrant, James Barber, George Porter, and David R. Klug. Observation of pheophytin reduction in photosystem two reaction centers using femtosecond transient absorption spectroscopy. *Biochemistry*, **31**:7638–7647, (1992).

[27] David R. Klug, Thomas Rech, D. Melissa Joseph, James Barber, James R. Durrant, and George Porter. Primary processes in isolated photosystem ii reaction centres probed by magic angle transient absorption spectroscopy. *Chemical Physics*, **194**:433–442, (1995).

[28] Marie Louise Groot, Natalia P. Pawlowicz, Luuk J. G. W. van Wilderen, Jacques Breton, Ivo H. M. van Stokkum, and Rienk van Grondelle. Initial electron donor and acceptor in isolated photosystem ii reaction centers identified with femtosecond mid-ir spectroscopy. *Proceedings*

of the National Academy of Sciences of the United States of America, **102**:13087–13092, (2005).

[29] A. R. Holzwarth, M. G. Mller, M. Reus, M. Nowaczyk, J. Sander, and M. Rgner. Kinetics and mechanism of electron transfer in intact photosystem ii and in the isolated reaction center: Pheophytin is the primary electron acceptor. *Proceedings of the National Academy of Sciences*, **103**:6895–6900, (2006).

[30] Th. Forster. Energiewanderung und fluoreszenz. *Naturwissenschaften*, **33**:166–175.

[31] M. H. Vos, F. Rappaport, J. C. Lambry, J. Breton, and J. L. Martin. Visualization of coherent nuclear motion in a membrane-protein by femtosecond spectroscopy. *Nature*, **363**:320–325, (1993).

[32] M H Vos, M R Jones, C N Hunter, J Breton, and J L Martin. Coherent nuclear dynamics at room temperature in bacterial reaction centers. *Proceedings of the National Academy of Sciences*, **91**:12701–12705, (1994).

[33] Christian Rischel, Diane Spiedel, Justin P. Ridge, Michael R. Jones, Jacques Breton, Jean-Christophe Lambry, Jean-Louis Martin, and Marten H. Vos. Low frequency vibrational modes in proteins: Changes induced by point-mutations in the protein-cofactor matrix of bacterial reaction centers. *Proceedings of the National Academy of Sciences of the United States of America*, **95**:12306–12311, (1998).

[34] M. H. Vos, J. C. Lambry, S. J. Robles, D. C. Youvan, J. Breton, and J. L. Martin. Direct observation of vibrational coherence in bacterial reaction centers using femtosecond absorption spectroscopy. *Proceedings of the National Academy of Sciences of the United States of America*, **88**:8885–8889, (1991).

[35] S. Sprlein, W. Zinth, and J. Wachtveitl. Vibrational coherence in photosynthetic reaction centers observed in the bacteriochlorophyll anion band. *The Journal of Physical Chemistry B*, **102**:7492–7496, (1998).

[36] Robert J. Stanley and Steven G. Boxer. Oscillations in the spontaneous fluorescence from photosynthetic reaction centers. *The Journal of Physical Chemistry*, **99**:859–863, (1995).

[37] A. M. Streltsov, T. J. Aartsma, A. J. Hoff, and V. A. Shuvalov. Oscillations within the bl absorption band of rhodobacter sphaeroides reaction centers upon 30 femtosecond excitation at 865 nm. *Chemical Physics Letters*, **266**:347–352, (1997).

[38] Vladimir I. Novoderezhkin, Andrey G. Yakovlev, Rienk van Grondelle, and Vladimir A. Shuvalov. Coherent nuclear and electronic dynamics in primary charge separation in photosynthetic reaction centers: a redfield theory approach. *The Journal of Physical Chemistry B*, **108**:7445–7457, (2004).

[39] R. Almeida and R. A. Marcus. Dynamics of electron transfer for a nonsuperexchange coherent mechanism. 2. numerical calculations. *The Journal of Physical Chemistry*, **94**:2978–2985, (1990).

[40] R. A. Marcus and R. Almeida. Dynamics of electron transfer for a nonsuperexchange coherent mechanism. 1. *The Journal of Physical Chemistry*, **94**:2973–2977, (1990).

[41] John N. Gehlen, Massimo Marchi, and David Chandler. Dynamics affecting the primary charge transfer in photosynthesis. *Science*, **263**:499–502, (1994).

[42] John M. Jean, Graham R. Fleming, and Richard A. Friesner. Classical and quantum models of activationless reaction dynamics. *Berichte der Bunsengesellschaft fr physikalische Chemie*, **95**:253–258, (1991).

[43] Gregory S. Engel, Tessa R. Calhoun, Elizabeth L. Read, Tae-Kyu Ahn, Tomas Mancal, Yuan-Chung Cheng, Robert E. Blankenship, and Graham R. Fleming. Evidence for wavelike energy transfer through quantum coherence in photosynthetic systems. *Nature*, **446**:782–786, (2007).

[44] Patrick E. Tekavec, Jeffrey A. Myers, Kristin L. M. Lewis, and Jennifer P. Ogilvie. Two-dimensional electronic spectroscopy with a continuum probe. *Optics Letters*, **34**:1390–1392, (2009).

[45] Alexandra Nemeth, Franz Milota, Tomas Mancal, Vladimir Lukes, Juergen Hauer, Harald F. Kauffmann, and Jaroslaw Sperling. Vibrational wave packet induced oscillations in two-dimensional electronic spectra. i. experiments. *Journal of Chemical Physics*, **132**, (2010).

[46] Alexandra Nemeth, Franz Milota, Tomas Mancal, Vladimir Lukes, Juergen Hauer, Harald F. Kauffmann, and Jaroslaw Sperling. Vibrational wave packet induced oscillations in two-dimensional electronic spectra. i. experiments. *Journal of Chemical Physics*, **132**, (2010).

[47] Alexei Halpin, Philip J. M. Johnson, Roel Tempelaar, R. Scott Murphy, Jasper Knoester, Thomas L. C. Jansen, and R. J. Dwayne Miller. Two-dimensional spectroscopy of a molecular dimer unveils the effects of vibronic coupling on exciton coherences. *Nature Chemistry*, **6**: 196–201, (2014).

[48] Franz Milota, Valentyn I. Prokhorenko, Tomas Mancal, Hans von Berlepsch, Oliver Bixner, Harald F. Kauffmann, and Juergen Hauer. Vibronic and vibrational coherences in two-dimensional electronic spectra of supramolecular j-aggregates. *Journal of Physical Chemistry A*, **117**:6007–6014, (2013).

[49] Gabriela S. Schlau-Cohen, Tessa R. Calhoun, Naomi S. Ginsberg, Elizabeth L. Read, Matteo Ballottari, Roberto Bassi, Rienk van Grondelle, and Graham R. Fleming. Pathways of energy flow in lhcii from two-dimensional electronic spectroscopy. *Journal of Physical Chemistry B*, **113**:15352–15363, (2009).

[50] Elizabeth L. Read, Gregory S. Engel, Tessa R. Calhoun, Tomas Mancal, Tae Kyu Ahn, Robert E. Blankenship, and Graham R. Fleming. Cross-peak-specific two-dimensional electronic spectroscopy. *Proceedings of the National Academy of Sciences of the United States of America*, **104**:14203–14208, (2007).

[51] Gregory D. Scholes, Graham R. Fleming, Alexandra Olaya-Castro, and Rienk van Grondelle. Lessons from nature about solar light harvesting. *Nature Chemistry*, **3**:763–774, (2011).

[52] Elisabetta Collini, Cathy Y. Wong, Krystyna E. Wilk, Paul M. G. Curmi, Paul Brumer, and Gregory D. Scholes. Coherently wired light-harvesting in photosynthetic marine algae at ambient temperature. *Nature*, **463**:644–U69, (2010).

[53] Hohjai Lee, Yuan-Chung Cheng, and Graham R. Fleming. Coherence dynamics in photosynthesis: Protein protection of excitonic coherence. *Science*, **316**:1462–1465, (2007).

[54] Franklin D. Fuller, Jie Pan, Andrius Gelzinis, Vytautas Butkus, S. Seckin Senlik, Daniel E. Wilcox, Charles F. Yocum, Leonas Valkunas, Darius Abramavicius, and Jennifer P. Ogilvie.

Vibronic coherence in oxygenic photosynthesis. *Nature Chemistry*, **6**:706–711, (2014).

[55] Elisabet Romero, Ramunas Augulis, Vladimir I. Novoderezhkin, Marco Ferretti, Jos Thieme, Donatas Zigmantas, and Rienk van Grondelle. Quantum coherence in photosynthesis for efficient solar-energy conversion. *Nature Physics*, **10**:677–683, (2014).

[56] Sebastian Westenhoff, David Palecek, Petra Edlund, Philip Smith, and Donatas Zigmantas. Coherent picosecond exciton dynamics in a photosynthetic reaction center. *Journal of the American Chemical Society*, **134**:16484–16487, (2012).

[57] Elisabetta Collini and Gregory D. Scholes. Coherent intrachain energy migration in a conjugated polymer at room temperature. *Science*, **323**:369–373, (2009).

[58] Yin Song, Scott N. Clafton, Ryan D. Pensack, Tak W. Kee, and Gregory D. Scholes. Vibrational coherence probes the mechanism of ultrafast electron transfer in polymerfullerene blends. *Nat Commun*, **5**, (2014).

[59] Akihito Ishizaki and Graham R. Fleming. Theoretical examination of quantum coherence in a photosynthetic system at physiological temperature. *Proceedings of the National Academy of Sciences*, **106**:17255–17260, (2009).

[60] Vivek Tiwari, William K. Peters, and David M. Jonas. Electronic resonance with anticorrelated pigment vibrations drives photosynthetic energy transfer outside the adiabatic framework. *Proceedings of the National Academy of Sciences of the United States of America*, **110**: 1203–1208, (2013).

[61] M. B. Plenio and S. F. Huelga. Dephasing-assisted transport: quantum networks and biomolecules. *New Journal of Physics*, **10**:113019, (2008).

[62] Patrick Rebentrost, Masoud Mohseni, and Aln Aspuru-Guzik. Role of quantum coherence and environmental fluctuations in chromophoric energy transport. *The Journal of Physical Chemistry B*, **113**:9942–9947, (2009).

Chapter 2

Principles of Two Dimensional Electronic Spectroscopy

This chapter presents the fundamentals of two dimensional electronic spectroscopy (2DES). First, I will discuss the limitations of linear spectroscopy methods and our motivation for using 2DES. Next, I will introduce 2DES and discuss the 2D spectra for simple systems. I will continue with the theoretical foundation of 2DES where I discuss nonlinear polarization, the density matrix and Feynman diagrams. Lastly, I will describe the experimental setup used to collect the data presented in this thesis.

2.1 The Motivation for 2DES

In general, spectroscopy aims to characterize physical systems by probing the interaction between the applied electromagnetic field and the system. Different spectroscopy techniques provide insight regarding the different properties of the system. The success of a spectroscopy technique is determined by its ability to explain the measured data accurately using a theoretical model. When a spectroscopic measurement is explained by multiple theoretical models, another technique is needed to assess the correct one among those models [1].

Linear absorption spectroscopy is a widely used technique that measures the light absorbed by the sample as a function of frequency or wavelength. It is usually the first technique used to characterize the energy level structure and the optical transitions of a system. The major drawback

of this technique is that it can measure very similar absorption profiles for systems which are described by completely different models. For clarification, I will demonstrate two scenarios where different models can be used to explain the same features observed in a given absorption spectra. The first one is intended to explain the physical origins of two separate peaks in the absorption spectra depicted in Figure 2.1a. A mixture of non-interacting A and B molecules or a quantum coupled system can have the same absorption profiles. The energy level structures of these models are depicted in Figure 2.1b and 2.1c.

The second scenario discusses the origin of the broad lineshapes shown in Figure 2.2a and 2.2b. Two different mechanisms can be used to explain this feature: 1. Homogeneous broadening. 2. Inhomogeneous broadening. Homogeneous broadening is a result of irreversible relaxation in a single optical transition, where the lineshape is modeled with a Lorentzian profile and its width is given by $1/\tau_{lifetime}$. In contrast, inhomogeneous broadening is result of the distribution of different absorption frequencies. In the condensed phase, molecules in slightly different environments have slightly shifted transition frequencies, and summation of all these yield an inhomogeneously broadened absorption peak.

In both scenarios, linear absorption spectroscopy fails to distinguish the two very different models and to assign a unique physical origin to the features seen in the spectrum. The reason is the linearity of the absorption measurement since this technique involves two light-matter interactions, the first one is the primary input light field and the second is the signal emission. Linear absorption spectroscopy, as well as other linear methods, are not able to follow dynamics, which is essential to resolve the problems described above. In contrast, nonlinear spectroscopy techniques employ multiple light-matter interactions and are capable of following system dynamics. Thus, nonlinear spectroscopy has a great potential in solving problems such as those described above.

Several types of nonlinear spectroscopy methods have been used to study the molecular processes for decades [2]. The transient absorption method has been the most popular one with its ability to resolve femtosecond dynamics. However, particularly in condensed phase, spectral congestion and short timescales for the molecular processes hinder achieving the desired spectral

and the temporal resolution concurrently by the transient absorption spectroscopy. The Q_y band in the PSII RC is a good example for spectral congestion. This band is heavily populated with pigments which have similar overlapping absorption features. In this band obtaining a spectral resolution that can differentiate between those signals is a challenging problem. In transient absorption spectroscopy, spectral resolution can be increased by decreasing the bandwidth of pump pulse. However, this results in longer pulse duration in turn decreasing the temporal resolution. For example, the initial photoreactions occuring in the PSII RC have broad timescales ranging from femtoseconds to several picoseconds. To resolve molecular dynamics in this system with the highest temporal and spectral resolution is not achievable by transient absorption spectroscopy. In this regard, two dimensional electronic spectroscopy (2DES) is a promising technique for studying molecular dynamics by providing both high spectral and temporal resolution, and it is described in the following section [3, 4].

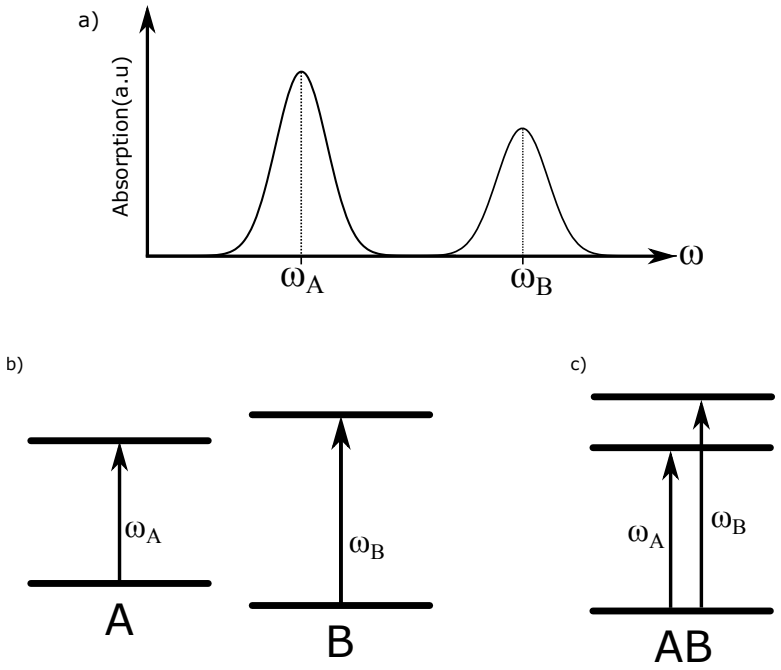

Figure 2.1: a)Linear absorption measurement of an unknown system. b) Energy level structure of a mixed system with two non interacting molecules. c) Energy level structure of a quantum coupled system.

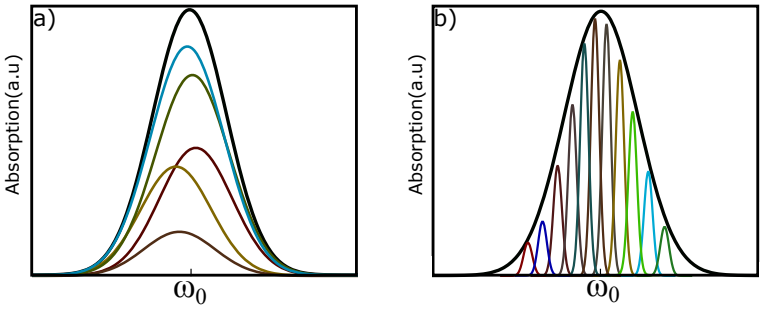

Figure 2.2: Linear absorption profiles showing broad lineshape due to two different physical mechanisms: a) Homogeneous broadening. b) Inhomogeneous broadening

2.2 Theory of Two Dimensional Electronic Spectroscopy

Two dimensional electronic spectroscopy is a three pulse scattering experiment which resolves two frequency axes, related to absorbed and later emitted light, dynamically as a function of interpulse waiting time. The pulse sequence for 2DES is shown in Figure 2.3. The sample is stimulated by two pulses (pump pulse-1/pump pulse-2) with a varying inter pulse time delay, t_1, and a third pulse (probe pulse) probes the induced changes in the system after a time delay t_2 (waiting time) which is measured from the time of the interaction between the second pulse and the system. The emitted signal is typically measured in the frequency domain similar to frequency resolved transient absorption spectroscopy, yielding the "detection frequency", ω_3, directly. The measurement is repeated for varying t_1 values, and the resulting signal is numerically Fourier transformed along t_1, yielding the "excitation frequency" axis, ω_1. The final presentation of the measured data is in the form of a two dimensional (2D) correlation map for a single waiting time ,t_2. Measurements performed at different waiting times provide insight into the dynamics of the system [4].

2DES and transient absorption spectroscopy are conceptually very similar; both methods employ pump and probe pulses to investigate the system dynamics as a function of waiting time. The critical major difference is that 2DES employs a second pump pulse to resolve the excitation axis which cannot be resolved in transient absorption spectroscopy. This additional information enables higher spectral resolution with respect to excitation frequency without sacrificing time resolution unlike in transient absorption spectroscopy. A 2DES measurement can be thought of as a correlation measurement showing how a frequency in the excitation axis is related to a frequency in the detection axis.

2DES resolves the problem of distinguishing homogeneous vs. inhomogeneous broadening discussed in Section 2.1. Figure 2.4 shows a schematic illustration of a 2D spectrum for an isolated molecule with single electronic excitation at different waiting times, t_2. At early waiting times, the antidiagonal linewidth of the peak characterizes homogeneous broadening properties while the diagonal linewidth characterizes inhomogeneous broadening properties. Figure 2.4b shows the spectrum of the same system at longer waiting times; when spectral diffusion has led to loss

of correlation between the excitation and the detection axes in the inhomogeneously broadened system.

In addition, 2DES provides an enhanced capability to investigate quantum coupled systems. Figure 2.5a and Figure 2.5b shows 2D spectra, and energy level diagrams for two different systems which exhibit the same linear absorption spectra. The cross peaks in 2D spectrum shown in Figure2.5b are indicators for the existence of coupling in the system. These peaks are also used to probe the coherent dynamics in the system, which will be discussed in the following section.

To understand the physical origins of the signals and how the response function is related to the system, we will use a density matrix formalism and diagramatic perturbation theory which has been explained in detail elsewhere[1, 2, 4].

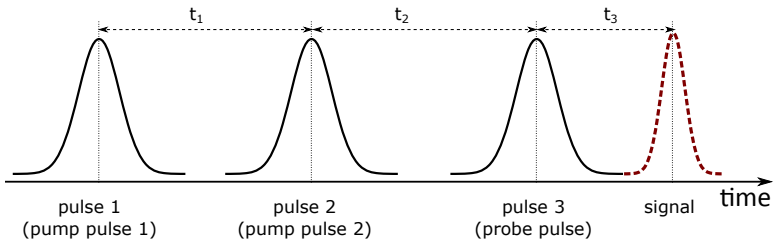

Figure 2.3: The input pulse sequence for two dimensional electronic spectroscopy. Definition of time variables and the pulses.

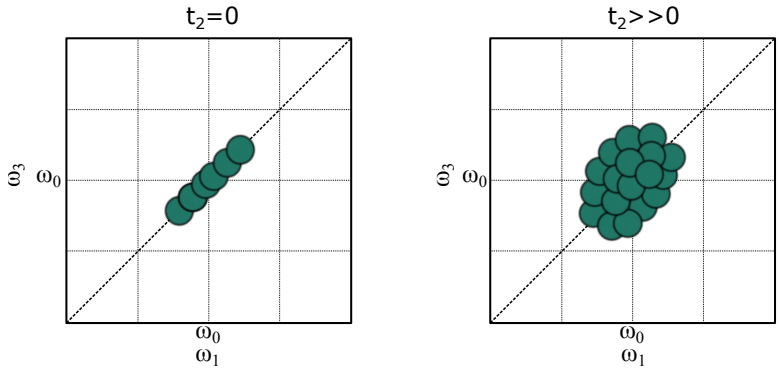

Figure 2.4: The schematic illustration of 2D spectra at different waiting times, showing evolution of a broadened lineshape: a) Inhomogeneously broadened lineshape at t_2=0. b) Inhomogeneously broadened lineshape at later waiting time $t_2 >> 0$

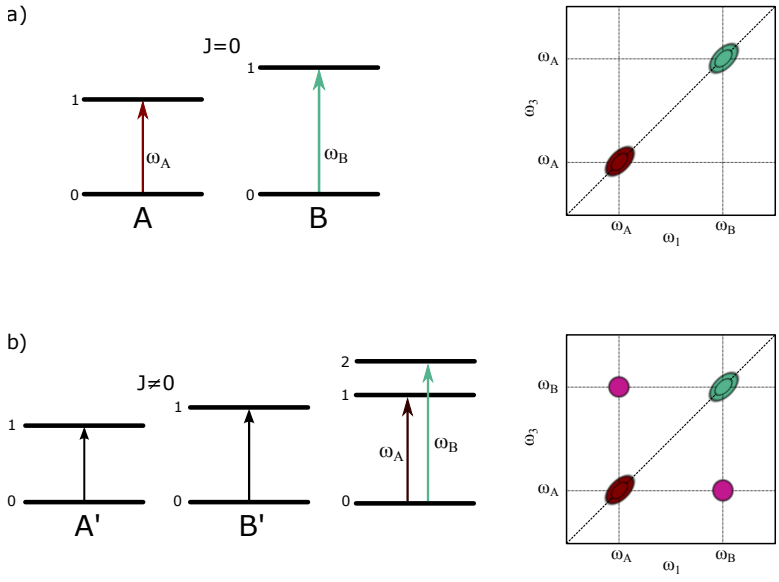

Figure 2.5: The schematic illustration of 2D spectra for two different systems. a) Two uncoupled two-level systems giving rise to diagonal peaks but no cross-peaks. b) A coupled quantum three level system, exhibiting diagonal and cross peaks.

2.2.1 Nonlinear Polarization

Optical spectroscopy techniques are based on probing the induced polarization changes in a system under controlled light-matter interactions. The polarization is typically not measured directly, but the electric field radiated by the system due to the induced polarization is measured. However, understanding of the polarization is crucial to gain physical insight about the system. When the light-matter interactions are in the weak regime, the induced polarization can be described using using the perturbation theory as follows:

$$P(t) = P^{(1)}(t) + P^{(2)}(t) + P^{(3)}(t) + ... \tag{2.1}$$

where $P^{(n)}(t)$ is the polarization induced after the nth light matter interaction [2]. The name and the order of spectroscopy is related to probed polarization term, $P^{(n)}$. For example, linear absorption spectroscopy probes the $P^{(1)}(t)$ term and reveals absorption properties of the system. Whereas, 2DES probes the $P^{(3)}(t)$ term which is described by the convolution of system response function, $S^{(3)}$, and incoming electric fields of the three input pulses:

$$\begin{aligned} P^{(3)}(t) = &\int_0^\infty dt_3 \int_0^\infty dt_2 \int_0^\infty dt_1 S^{(3)}(t_1, t_2, t_3) \\ &E_1(t - t_1 - t_2 - t_3) E_2(t - t_2 - t_3) E_3(t - t_3) \end{aligned} \tag{2.2a}$$

$$E_i(t) = A_i(t) e^{-i\omega_i t + i\overrightarrow{k_1}\overrightarrow{r} + i\varphi_i(t)} + c.c \tag{2.2b}$$

where E_i refers to the interacting electric fields, and subscript i indicates the interaction order of the pulses as depicted in Figure 2.3. Two dimensional electronic spectroscopy aims to characterize the third order response function of a system in the frequency domain, $S^{(3)}(\omega_1, \omega_2, \omega_3)$. The consecutive measurements performed by varying inter pulse delays and Fourier transform of the measured signal along the appropriate time axes yield the response function.

The wavelengths of the pulses used in 2DES vary between ~400-800 nm. Therefore, $\overrightarrow{k_i} \cdot \overrightarrow{r} >> 1$ condition is satisfied for 2DES measurements which indicates that the emitted signals are highly

directional enabling spatial isolation of the emitted signals. Thus, we utilize phase matching to isolate signals based on their propagation direction. The three input fields contribute to the signal direction with either +k_i or -k_i, forming $2^3 = 8$ possibilities for the signal directions. The dominant signals in 2DES are described as:

$$k_s = \pm k_1 \pm k_2 \pm k_3 \tag{2.3a}$$

$$k_R = -k_1 + k_2 + k_3 \tag{2.3b}$$

$$k_{NR} = k_1 - k_2 + k_3 \tag{2.3c}$$

The signals propagating along k_R and k_{NR} are called rephasing and nonrephasing signals respectively. This terminology comes from the difference in the evolution of signal phase during t_1 and t_3 intervals. The phase acquired during the t_1 interval is reversed during the t_3 interval in the rephasing signal unlike the nonrephasing one. The phase of rephasing and nonrephaing signals are related to the phase of input pulses as described below:

$$\phi_R = -\phi_1 + \phi_2 + \phi_3 \tag{2.4a}$$

$$\phi_{NR} = \phi_1 - \phi_2 + \phi_3 \tag{2.4b}$$

where ϕ_i refers to the phase of the pulses, and subscript i indicates the interaction order of the pulses.

2.2.2 Density Matrix

The density matrix is a very powerful formalism used to describe open and closed quantum systems. It also has the flexibility to describe an ensemble of mixed states. Time evolution of the density matrix is given by the Liouville equation, and the solution to it provides information regarding the time evolution of system in response to the light-matter interactions. The density matrix of a three level system shown as in Figure 2.6a is determined by eigenstates $(|a\rangle, |b\rangle, |c\rangle)$

and density matrix operator ρ, and given as below:

$$\begin{bmatrix} \langle a|\,\rho\,|a\rangle & \langle b|\,\rho\,|a\rangle & \langle c|\,\rho\,|a\rangle \\ \langle a|\,\rho\,|b\rangle & \langle b|\,\rho\,|b\rangle & \langle c|\,\rho\,|b\rangle \\ \langle a|\,\rho\,|c\rangle & \langle b|\,\rho\,|c\rangle & \langle c|\,\rho\,|c\rangle \end{bmatrix} \tag{2.5}$$

The density matrix elements include all the possible inner products of bras and kets. The diagonal elements, $\langle a|\,\rho\,|a\rangle$, $\langle b|\,\rho\,|b\rangle$, $\langle c|\,\rho\,|c\rangle$, are known as populations, and the off diagonal elements are known as the coherences. Coherent states refer to superpositions of different eigenstates of the system.

In each light-matter interaction the dipole operator acts on the density matrix, alternately creating coherences or populations. The excitation field properties such as polarization, direction, bandwidth of the input pulses, and the system properties such as dipole strength and eigenstate energies determine which changes in the density matrix can take place. For example, when the transition wavelength between two eigenstates, ($|a\rangle$ and $|b\rangle$), falls within the pulse bandwidth, a single pulse interaction can turn a population (e.g. $\langle a|\,\rho\,|a\rangle$) a coherence (e.g. $\langle a|\,\rho\,|b\rangle$ or $\langle b|\,\rho\,|a\rangle$). In this formalism one interaction can make one change which is either on the bra or the ket.

Figure 2.6b illustrates one possible evolution of the density matrix for a three level system shown in Figure 2.6a during 2DES measurements. The system is assumed to be in its ground state before the excitation. Among many possible pathways, only the two (a population state and a coherence state during the waiting time, t_2) are given in the shown density matrix evolution. The corresponding signal positions in the 2D spectrum is shown in Figure 2.6c.

The spectroscopic signatures of a coherence and a population are significantly different. When a system is in a coherence during the time interval between subsequent interactions, the signal amplitude oscillates as a function of inter pulse time delays, with an oscillation frequency proportional to the energy difference between the two eigenstates. The coherences occuring during t_1 and t_3 determines the signal peak position in 2D spectrum. In the example given above, the two signals have coherences with identical energy differences, and their peak positions are located at the same

frequency value, ω_1=$E_b/\hbar$, on the excitation axis. In contrast, during t_3 interval, they have different coherences with different energy difference resulting in different peak positions on the detection axis, ω_3=$E_b/\hbar$ and ω_3=$E_c/\hbar$. The coherences observed during waiting time, t_2, waiting time are of particular importance in this thesis, where their frequency, phase and function are investigated. The spectral signature of a coherence during the waiting time is sinusoidal modulations in the signal amplitude, whereas a population does not have these modulations. In general the spectral signatures of the coherences and the populations are mixed throughout the 2D spectrum, necessitating advanced analysis techniques to extract information about the coherences. I will discuss coherences observed in the PSII RC and Chl-a in more detail in the following chapters.

The third-order response function, the $S^{(3)}$ term in Equation 2.2a, is defined as the expectation value of the dipole operator 2.2a on the system state after all the light-matter interactions occurred in 2DES, and describe by the following equation [2]:

$$S^{(3)}(t_3,t_2,t_1) = (\frac{i}{\hbar})^3\theta(t_3)\theta(t_2)\theta(t_1)\sum_{\alpha=1}^{4} R_\alpha(t_3,t_2,t_1) - R_\alpha^\star(t_3,t_2,t_1) \tag{2.6a}$$

$$R_1(t_3,t_2,t_1) = V(t_1)V(t_1+t_2)V(t_1+t_2+t_3)V(0)\rho(-\infty) \tag{2.6b}$$

$$R_2(t_3,t_2,t_1) = V(0)V(t_1+t_2)V(t_1+t_2+t_3)V(t_1)\rho(-\infty) \tag{2.6c}$$

$$R_3(t_3,t_2,t_1) = V(0)V(t_1)V(t_1+t_2+t_3)V(t_1+t_2)\rho(-\infty) \tag{2.6d}$$

$$R_4(t_3,t_2,t_1) = V(t_1+t_2+t_3)V(t_1+t_2)V(t_1)V(0)\rho(-\infty) \tag{2.6e}$$

where $\rho(-\infty)$ stands for the initial state of the system before any excitation, V_i ($i = 1,2,3$) is the dipole operator which modifies the density matrix after the i^{th} interaction, $G(t_i)$ ($i = 1,2,3$) is the Green function which defines the free propagation during the t_i ($i = 1,2,3$) interval, V_s is the final interaction operator for the signal emission, and $\theta(t_i)$ is the Heaviside function. There are $2^3 = 8$ subcomponents of the response function, and the half of these components are complex conjugates of the other half.

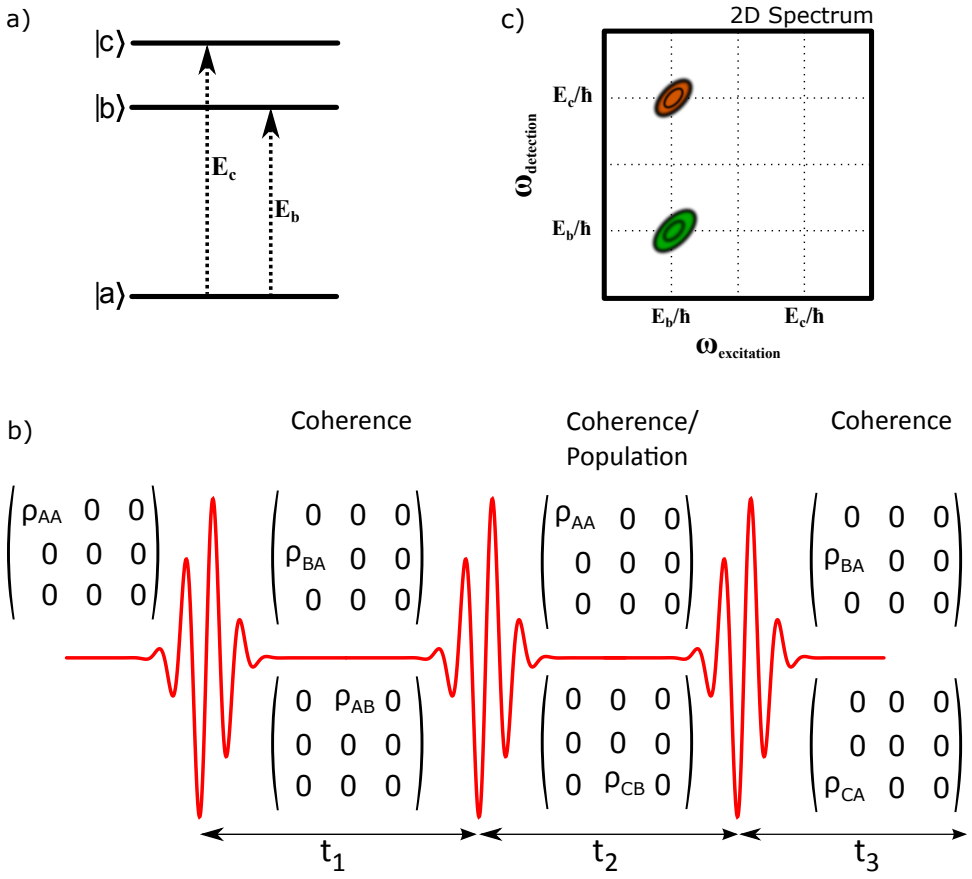

Figure 2.6: a) The energy level structure of a three level system. b) Evolution of the density matrix of the same system during 2DES measurements (only a subset of signals are shown). c) The 2D spectrum showing the signals associated to the pathways shown in the density matrix.

2.2.3 Diagramatic Perturbation Theory

The nonlinear response functions and density matrix formalism are very powerful to formulate molecular dynamics and simulate light-matter interactions. However, when multiple states contribute to signals with varying directions and frequencies, this formalism is rather difficult to interpret. Diagramatic Perturbation Theory (DPT) provides an easier way to keep track of the system and light-matter interactions. DPT is also helpful to categorize signal origins such as ground state, excited state, and stimulated emission etc.

In the following, I will review the double sided Feynman diagrams, which are widely used in this field. Feynman diagrams describe how density matrix elements evolve during the experiment.

A Feynman diagram is composed of bras, kets, inward arrows, and outward arrows. Figure 2.7a shows a Feynman diagram for a two level system. We can summarize the rules and how to read a Feynman diagram in six steps: 1.Bras and kets represent the density matrix elements. 2.The initial state is written at the bottom of diagram. 3.Time evolution is always upwards. 4.Light-matter interactions are described by the inward or outward arrows. 5.The system evolves freely between these interactions. 6.Each arrow describes either a positive or a negative contribution to signal direction as well as to the signal frequency. Additional detail is given in Figure 2.7.

Figure 2.8 shows the Feynmann diagrams corresponding to the response functions. R_1 and R_4 generate nonrephasing signal along k_{NR}=k_1-k_2+k_3, and at ω_{NR}=ω_1-ω_2+ω_3. R_2 and R_3 generate rephasing signal along k_R=-k_1+k_2+k_3, and at ω_R=-ω_1+ω_2+ω_3. R_2 and R_3 terms evolve conjugate phases during t_1 and t_3 interval, whereas R_1 and R_4 terms evolve in same direction during t_1 and t_3 interval.

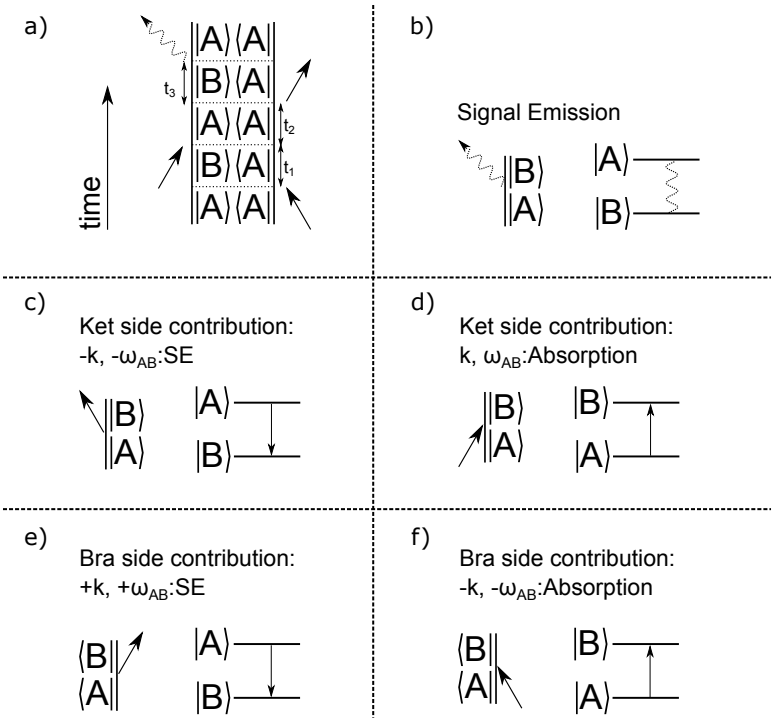

Figure 2.7: Feynman Diagram Tutorial. Adapted from [1].

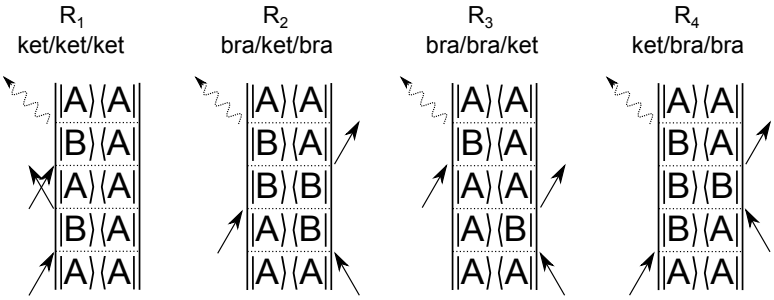

Figure 2.8: The Feynman Diagrams associated to response functions described in Equations 2.6b-2.6e. Adapted from [1].

2.3 Experimental Implementations of 2DES

In this section, I will present the experimental apparatus used to measure the data presented in this thesis. There are two essential components of this experimental setup which are the light sources and the 2DES spectrometer.

2.3.1 Light sources

The laser sources used in the experiments were derived from a Ti:Sapphire oscillator (MaiTai SP) seeding a regenerative amplifier to produce 40 fs pulses centered at 800 nm (Spectra Physics Spitfire Pro) running at 500 Hz. The 800 nm light is fed into two noncollinear optical parametric amplifiers (NOPA) and a degenerate optical parametric amplifier(DOPA).

NOPA operation principle is based on difference frequency generation (DFG) and second harmonic generation (SHG). SHG is a nonlinear process where two photons with the same energy is converted to a single photon with higher energy. The sum of incoming photon energies are equal to the energy of the generated photon. DFG is, similarly,a nonlinear process where a high energy photon, called the pump photon, is converted into two photons, called seed and idler. The sum of seed and idler photon energy is equal to the pump photon energy [5]. Both processes needs a nonlinear medium for phase matching and energy conservation. β-barium borate (BBO), a common nonlinear medium, is used to implement DFG and SHG in NOPA designs [6, 7].

We have two home built NOPAs delivering pulses centered from 480 nm to 680 nm with ~80-100 nm bandwidth in our lab. The layout for the NOPA is shown in Figure 2.9. The Ti:sapphire laser output at 800 nm which feeds the NOPA is split into two beams. The first beam is sent through a 0.5 mm thick BBO crystal to generate beams centered at 400 nm, pump beam where the conversion efficiency is ~20%. The second beam is focused onto 3 mm thick C-axis cut sapphire plate to generate the white light (seed beam). White light is collimated to ~2 mm beam size using a 1 inch focal length off axis parabolic mirror. The pump beam is split into two beams (Pump I, Pump II) to be used for amplification in two crystals (NOPA I, NOPA II). The pump beam and seed

beam are temporally and spatially overlapped in NOPA crytstal I. The crossing angle between the beams and the crystal rotation is optimized for the desired central wavelength and bandwidth. The amplified seed beam and pump beam (Pump II) are then focused onto NOPA crytsal II to increase output power and stability. Lenses of 25 cm and 75 cm focal length are used to focus pump-I and pump-II beams respectively. Lens positions are adjusted to focus beams in front of the crystals to prevent damage and increase the output mode quality. The temporal overlap between pump beams and seed beam is controlled with 90 degree prisms on each pump beam path. Two NOPAs are used to collect data represented in Chapter 3 and 4.

The operation principle of the DOPA is similar to the NOPA. The DOPA delivers pulses centered at ~800 nm with ~150-200 nm bandwidth. The DOPA can be viewed as two separate OPAs operating at different central wavelengths. In the first stage, broadband pulses centered at ~1.3 μm are generated. In the second stage, the 1.3 μm light is used to generate a white light seed which is stable at 800nm [8]. This seed is amplified in the second stage [8]. The DOPA is used to collect data presented in Chapter 5.

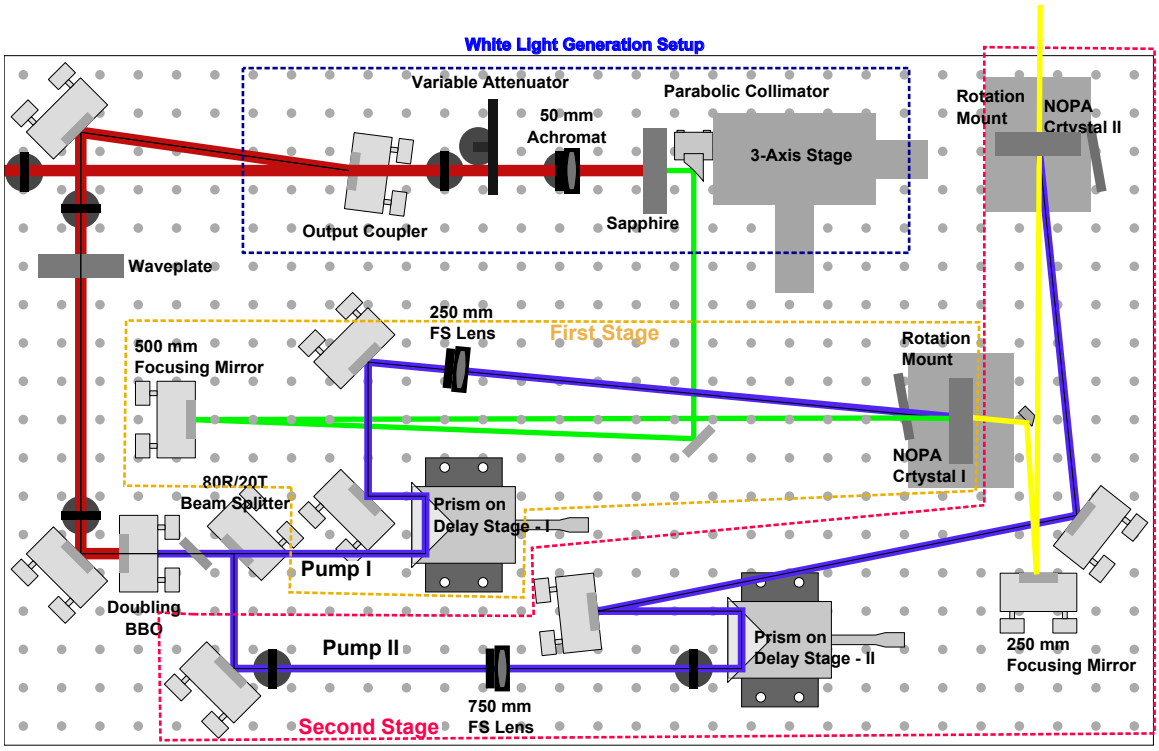

Figure 2.9: The schematic presentation of home built NOPA used in this study. The first and second stage of the NOPA is emphasized by enclosing the related optics. The pump beams, the white light seed and amplified output are shown as blue, green and yellow lines respectively. The thick red line shows the Ti:Sapphire laser output. Adapted from [9].

2.3.2 2DES Spectrometer

Over the last decade, there were several experimental demonstrations of 2DES, each with its own advantages and drawbacks [3, 10, 11, 11–21]. The design principles of different approaches seek the optimization of different experimental parameters: increasing the signal to noise and the phase stability, decreasing the cost and complexity of the experimental apparatus, increasing the setup capability to work within different spectral regions. These methods, in general, differ in their methods of the input pulse sequence creation, inter-pulse time delay scanning and the signal detection scheme. Herein, we focus on the two widely used experimental setups among the 2DES community: diffractive optics based box-CARS (noncollinear) setup and pulse shaping based pump-probe (collinear) setup.

The pulse shaping based pump-probe setup is depicted schematically in Figure 2.10a. An acousto-optic pulse shaper is employed to create the pump pulse pair and control inter-pump pulse delay, t_1. Two pump pulses have the identical propagation direction across the experimental setup. A retro reflector in the probe path is employed to delay the probe pulse and control the waiting time, t_2. Next, the pump and the probe beams are focused onto the sample to generate the third order signals (rephasing and nonrephasing signals) [14, 22, 23]. In this geometry, the propagation directions of the rephasing and the nonrephasing signals, which are given by Equation 2.3b-2.3c are identical to that of the probe signal since the two pump pulses have the same propagation direction (k_1=k_2). The rephasing and nonrephasing signal are captured simultaneously and can be isolated using the phase cycling technique. The phase cycling technique relies on the presence of a difference in the phases of these different signals, which are given by Equation 2.4a-2.4b; measurements performed by varying the pump pulse phase can yield the desired isolation. Acousto-optic pulse shapers are capable of controlling the input pump pulse phase, enabling phase cycling [22, 23]. The two main advantages of this setup are its relatively easy alignment, and its capability of measuring both the rephasing and nonrephasing signals simultaneously. The major drawback is the signal propagation direction which is collinear with the probe pulse propagation direction, imposing a limit to the signal to noise of the measurement. The allowed maximum probe pulse intensity used to boost the

signal amplitude is limited by the upper limit detector dynamic range (i.e. the detector started to saturate after a certain probe pulse intensity). The high cost of the acousto-optic pulse shapers is another drawback for this setup.

The diffractive optics based box-CARS setup is schematically depicted in Figure 2.11a. The pump and probe beams are focused on a transmissive grating, and all the diffraction orders other than ± 1 orders are blocked after the grating [12, 13]. The inter-pump pulse delay, t_1, is achieved by placing thin wedge pairs which are mounted on motorized linear stages in each pump beam path (± 1 orders). The position of these pairs are scanned such that the optical path length of one pump pulse is increased/decreased with respect to that of the other pump pulse, enabling t_1 control. The probe beam incident on the diffractive optics also creates two diffraction orders; one of them is used as the probe pulse, whereas the other is used as a local oscillator [13]. In the diffractive optics based box-CARS setup, the three input pulses travel along the three corners of a square, whereas the measured signal and the local oscillator travels along the fourth corner. The local oscillator is delayed with respect to the probe pulse to heterodyne the signal, and it is attenuated to avoid detector saturation and adjust its amplitude to optimize signal to noise ratio. For visualizing the signal propagation, the propagation directions of the input pulses and signals are described by the unit vectors in Cartesian cordinates(x,y,z) as below:

$$k_1 = (1,-1,1) \quad k_2 = (1,1,1) \quad k_3 = (-1,-1,1), \quad k_S = (-1,1,1) \tag{2.7a}$$

$$\begin{aligned} k_R &= -k_1 + k_2 + k_3 \\ &= (-1,1,1) \end{aligned} \tag{2.7b}$$

$$\begin{aligned} k_{NR} &= k_1 - k_2 + k_3 \\ &= (-1,-3,1) \end{aligned} \tag{2.7c}$$

where k_1, k_2, k_3, k_S refer to the directions of the first pump pulse, the second pump pulse, the probe pulse, and the measured signal respectively. k_R and k_{NR} refer to the propagation direction of the rephasing and the nonrephasing signal generated. Figure 2.11b shows a schematic illustration of

the beam propagation geometry before and after the sample in the three dimensional view. In this pulse sequence, when the pump pulse with k_1 interact with system before the pump pulse with k_2, the rephasing signal is in the measured signal direction (k_S=k_R). In case of the interaction of the pump pulse with k_2 is the first, the nonrephasing is in the measured signal direction (k_S=k_{NR}). The interaction order can be easily controlled by adjusting the relative wedge positions. One should note that rephasing and nonrephasing signals cannot be captured simultaneously in this experimental setup. The local oscillator is mixed with the signal to characterize the amplitude and phase of the rephasing/nonrephasing signal using spectral interferometry [24]. The major advantage of this method is its capability of spatially isolating the signal from the input pulses, except the local oscillator. This enables a background free detection scheme, that is there is no probe pulse propagating collinearly with the signal. This capability enables us to increase signal to noise by increasing the probe pulse power without saturating the camera and by amplifying the signal by heterodyne detection. The imperfect calibration of motorized stages, which is the relation between wedge positions and t_1 delay, and mechanical instabilities from moving parts are the major drawbacks, since they may cause artifacts in the measured signal. Moreover, two separate measurements are required to capture both the rephasing and the nonrephasing signals, increasing the total experiment time. In addition, the alignment of this setup is significantly more difficult compared then the pulse shaping based pump-probe setup.

Many other methods such as single shot based and fluorescence detection based approaches are available for 2DES measurements. The description and comparison of these methods are beyond the scope of this thesis, and can be found in recent review studies of 2DES [25].

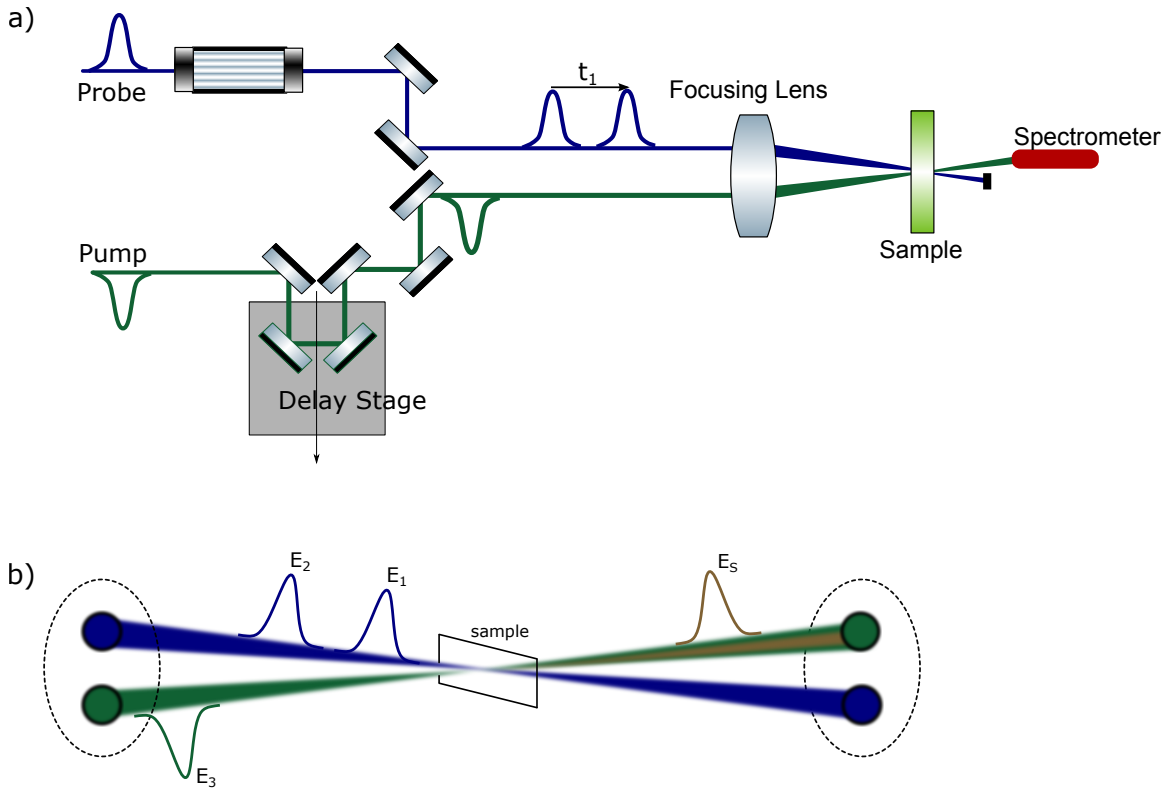

Figure 2.10: (a) The 2DES setup based on the pulse shaping based pump-probe approach. Adapted from [25]. (b)The side view of input beams around the sample. The blue beam represents the pump beam, having two pump pulses, and the green beam represents the probe pulse. Note that the signal (brown beam) is collinear with the probe beam.

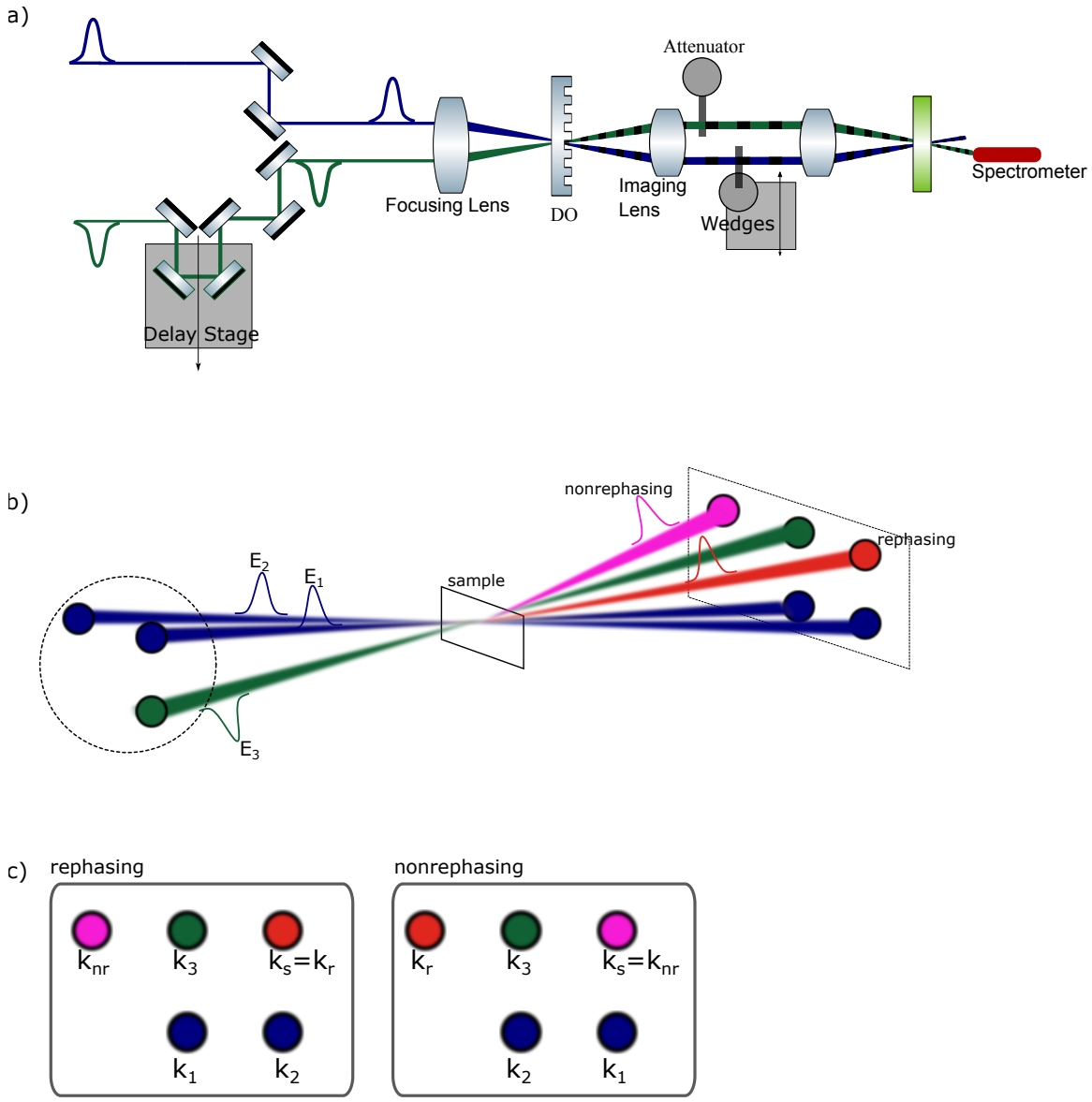

Figure 2.11: a) The 2DES Setup utilizing on diffractive optics based box-CARS approach. Adapted from [25]. b) The side view of input beams around the sample. Pump beams (blue beams) and probe beam (green beam) are focused onto sample. The interaction order is given by the pulses shown on the beams. Rephasing signal and nonrephasing signal emerge along different directions, red beam and magenta beam respectively. c) The propagation direction of input pulses and signals are shown on the the square plane for two different interaction orders. The box labeled with rephasing(nonrephasing) show the cases for rephasing(nonrephasing) signals travellin along the fourth corner of the box.

2.3.2.1 Experimental Apparatus

In my experiments, I used a hybrid diffractive optics and pulse shaping based setup which is recently developed in the Ogilvie Lab [26]. This approach takes the advantages of both methods. Figure 2.12a shows a schematic illustration of this experimental setup. An acousto-optic pulse shaper (Dazzler, Fastlite) is used to create pump pulse pairs, and diffractive optics is used to create the box-CARS configuration. The pump pulses are delivered from NOPA-I, and pre-compressed by a homemade grism which is a combination of prisms and gratings to compress the pulses. The Dazzler creates a pulse pair with the desired inter-pulse time delay, t_1, and a desired relative phase difference for phase-cycling. The probe pulse is delivered from NOPA-II and is compressed by a separate grism. A retroreflector on a motorized linear stage in the probe path is used to control waiting time, t_2. Both the pump and the probe beams are focused onto diffractive optics using a 50 cm focal length mirror. The employed diffractive optic is a transmissive grating made of fused silica, and it is optimized for the ± 1 diffraction orders. All but the ± 1 orders are blocked to prevent unwanted higher order signals, and unblocked orders are focused onto the sample using a 25 cm focal length mirror. The generated signal along the local oscillator direction (described in Section 2.3.2) is measured.

The major difference between a typical diffractive optics based box-CARS setup and our setup is the number of pump pulses in the pump beams after the diffractive optics. In the box-CARS setup described in Section 2.3.2, there is only one pump pulse on each pump beam, and the time delay, t_1, is introduced by having wedges. In contrast, in our setup, the pump beam which is focused onto diffractive optics contains two pump pulses created by the Dazzler. These pulses will be represented by P^A and P^B in the rest of this chapter. The generated ± 1 diffraction orders of the incoming pump beam contains this pulse pair as well, making four pulses in total (two pulse on each diffraction order). These pulses are represented by $P^A_{-1}, P^B_{-1}, P^A_{+1}, P^B_{+1}$ where the A, B superscripts refer to either of the pulses created by the Dazzler, and $+1, -1$ refer to the diffraction order. One should remember that P^A_{+1} and P^B_{+1} pulses (P^A_{-1} and P^B_{-1}) propagate along the same direction. Similarly, P^A_{-1} and P^A_{+1} (P^B_{-1} and P^B_{+1}) are identical pulses (having the same phase and

amplitude) but differing in their propagation direction.

The rephasing and nonrephasing signals we are interested in are generated by the pairwise interaction of the pump pulses on the different diffraction orders and the probe pulse. The interaction sequence for the rephasing and nonrephasing signals are given by $P^A_{-1}, P^B_{+1}, P_{Probe}$ and $P^A_{+1}, P^B_{-1}, P_{Probe}$ respectively. In the following, I will discuss the propagation directions of the signals for this hybrid setup. The propagation directions for the input beams in the hybrid setup are described by $k_{P_{+1}} = (1,1,1)$, $k_{P_{-1}} = (1,-1,1)$, $k_{Probe} = (-1,1,1)$, similarly in Section 2.3.2. Using this notation and the interaction sequences given above, we determine the propagation directions of the rephasing and nonrephasing signals as such:

$$\begin{aligned} k^{Sig}_{Rephasing} &= -k_1 + k_2 + k_3 \\ &= -k_{P^A_{-1}} + k_{P^B_{+1}} + k_{Probe} \\ &= -(1,-1,1) + (1,1,1) + (-1,-1,1) \\ &= (-1,1,1) \end{aligned} \tag{2.8}$$

$$\begin{aligned} k^{Sig}_{NonRephasing} &= k_1 - k_2 + k_3 \\ &= +k_{P^A_{+1}} - k_{P^B_{-1}} + k_{Probe} \\ &= +(1,1,1) - (1,-1,1) + (-1,-1,1) \\ &= (-1,1,1) \end{aligned} \tag{2.9}$$

Both the rephasing and the nonrephasing signal travel along the fourth corner of the square, and they are captured simultaneously by the detector. Unfortunately, there are other third order signals generated in the same propagation direction as that of the rephasing and the nonrephasing signals. Figure 2.13 is a schematic representation of the signals generated by different pulse sequences. The $P^A_{-1}, P^A_{+1}, P_{Probe}$ and $P^B_{-1}, P^B_{+1}, P_{Probe}$ pulse sequence creates two transient grating signals in the detection direction k_{signal}. The transient grating signals remain unchanged for varying t_1 values, whereas the rephasing and the nonrephasing signals change as a function of t_1. Fortunately, the phases of these signals depend on the phases of P^A and P^B in different ways; and their phases are

described by the following equations:

$$\begin{aligned}
\phi_{TG_1} &= -\phi_{P^A_{-1}} + \phi_{P^A_{+1}} + \phi_{Probe} \\
\phi_{TG_2} &= -\phi_{P^B_{-1}} + \phi_{P^B_{+1}} + \phi_{Probe} \\
\phi_R &= -\phi_{P^A_{-1}} + \phi_{P^B_{+1}} + \phi_{Probe} \\
\phi_{NR} &= \phi_{P^A_{+1}} - \phi_{P^B_{-1}} + \phi_{Probe}
\end{aligned} \tag{2.10}$$

Based on their different phase dependencies, we use phase cycling to isolate the rephasing, the nonrephasing and the transient grating signals. We employ the Dazzler to rotate the phases of P^A and P^B by e^{ix} and e^{iy} respectively. These phase rotations do not cause any changes in the phase of the transient grating signals, whereas the phases of the rephasing and nonrephasing signals are changed. Here, I would like to remind the reader one more time that a single measurement contains a mixture of these three signals which are measured simultaneously. Three successive measurements performed with different phase rotations, $(x_i, y_i; i = 1, 2, 3)$, provide a system of linear equations with three unknowns which are these signals. The solution to this system of linear equations enables us to isolate the transient grating signal (S_{TG}), the rephasing signal (S_R), and the nonrephasing signal (S_{NR}) which is given by the following equation:

$$\begin{bmatrix} S_{TG} \\ S_R \\ S_{NR} \end{bmatrix} = \begin{bmatrix} 1 & e^{i(x_1-y_1)} & e^{-i(x_1-y_1)} \\ 1 & e^{i(x_2-y_2)} & e^{-i(x_2-y_2)} \\ 1 & e^{i(x_3-y_3)} & e^{-i(x_3-y_3)} \end{bmatrix} \begin{bmatrix} S_1 \\ S_2 \\ S_3 \end{bmatrix} \tag{2.11}$$

where $S_i, i = 1, 2, 3$ refer to the signals obtained from successive measurements. We implement the phase rotation(e^{ix}, e^{iy}) profile below for the three measurements:

$$\{(x_1, y_1), (x_2, y_2), (x_3, y_3)\} = \{(0, 0), (0, \frac{2\pi}{3}), (0, \frac{4\pi}{3})\} \tag{2.12}$$

While the three measurements with the given phase profiles are sufficient to isolate the signals, another set of three successive measurements are performed to suppress the interference scattering terms between the pump pulses, the probe pulse and the measured signal. The phase profiles for the second set are π shifted versions of the first set, given by the following equation:

$$\{(x_4, y_4), (x_5, y_5), (x_6, y_6)\} = \{(\pi, \pi), (\pi, \frac{5\pi}{3}), (\pi, \frac{7\pi}{3})\} \tag{2.13}$$

That is, we implement six phase cycles per single t_1 point. The interference scatter term between the pump pulses is measured as the probe being blocked by a mechanical shutter (Thorlabs SH05). This terms is subtracted from the signal to improve the signal quality. The duty cycle is set to 90% to achieve a reasonable suppression of the scatter terms. The entire experiment yielding a full 2D spectrum for a given waiting time, t_2, is completed by measuring the signal at $t_1 = (0, 10, 20..., 400fs)$ values. The signal is measured by a CCD camera in the frequency domain, yielding the "detection axis" (ω_3), and the entire signal is Fourier transformed along the t_1 axis, yielding the "excitation axis" (ω_1). Finally, the measurements performed at different t_2 values yield a data structure which describes the system dynamics.

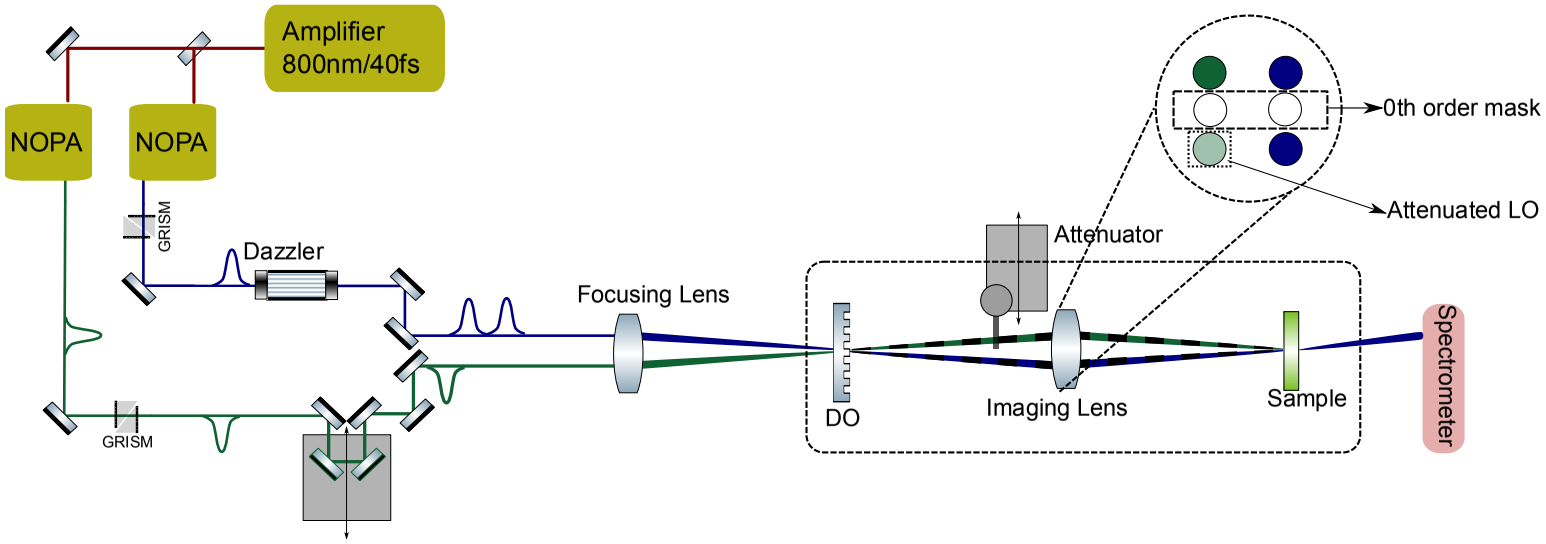

Figure 2.12: The schematic presentation (top view) of the hybrid diffractive optics and pulse shaping based 2DES setup used in this work. The imaging(focusing) lens corresponds to a focusing mirror in the actual setup [26].

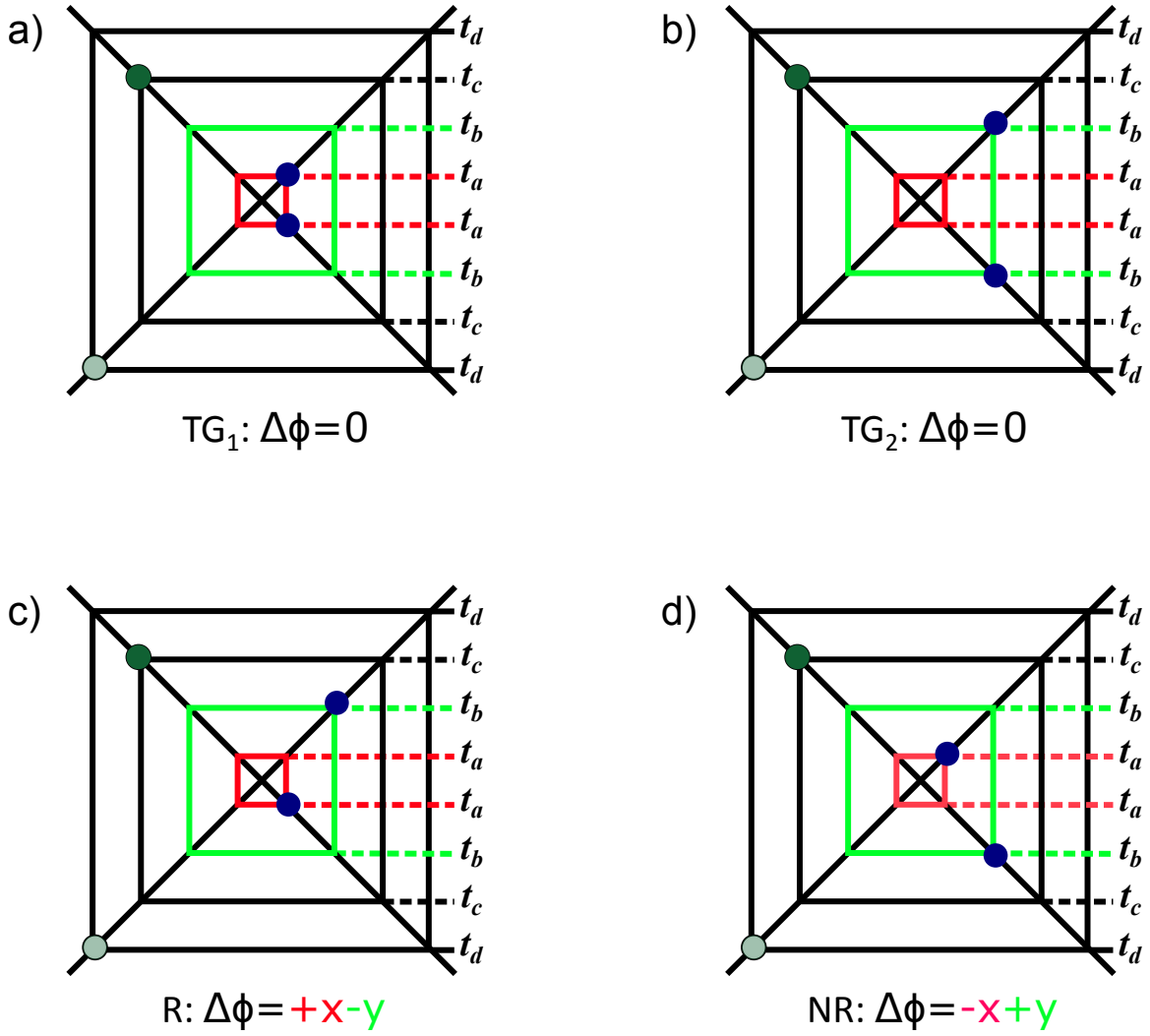

Figure 2.13: The pulse sequences for the signals detected in the hybrid setup with the appropriate time ordering for the two transient grating signals, the rephasing and the nonrephasing signal are shown. The phase applied to the pump pulse pair are labeled with red (x) and green (y) lines [26].

2.3.2.2 Detection Scheme and Phasing

In this section, I will describe how we heterodyne the signal with the local oscillator, and the way we use spectral interferometry to characterize the phase and amplitude of the signal [24]. The local oscillator is allowed to pass through the 1 mm thick fused silica, and it is τ delayed with respect to signal. The imaging mirror is patterned such that the metal coating on the region where the local oscillator is incident is removed. This mirror is employed as a neutral density filter to attenuate the local oscillator. There are no additional optics needed to combine the local oscillator and the signal before they are measured by the detector, since they are collinear. The measured spectrum is a linear combination of the signal and the local oscillator as described by the following equations:

$$\begin{aligned} E_{measured} &= |E_{signal} + E_{LO}e^{-i\omega\tau}|^2 \\ &= |E_{signal}|^2 + |E_{measured}|^2 + S(\omega) \qquad (2.14a) \\ S(\omega) &= Real\{2E_{signal}E_{measured}e^{i\omega\tau}\} \qquad (2.14b) \end{aligned}$$

where E_{LO} and E_{signal} are the electric fields of the local oscillator and the signal respectively. The $S(\omega)$ term represents the fringes on the measured spectrum, where the fringe separation is proportional to τ. The constant terms and $S(\omega)$ given in Equation 2.14a, are isolated by Fourier transforming the measured signal, $E_{measured}$, along the ω axis. Fourier transform yields a pseudo time axis, where the constant terms are centered at $t = 0$. Fourier transform of $S(\omega)$ yields two functions which are time reversed with respect to each other, and given by the following equation:

$$FT\left[S(\omega)\right] = f(t-\tau) + f(-t-\tau) \qquad (2.15)$$

We single out the peak centered at $t = \tau$ by applying a super Gaussian filter and inverse Fourier transforming from pseudo time axis to original ω axis. We isolate the signal through its proper division by the local oscillator and subtracting the contribution of the $e^{(i\omega\tau)}$ term given in $S(\omega)$.

The following equation describes these steps:

$$E(\omega) = \frac{F_{SG}\left[FT\left[S(\omega)\right]\right] e^{(-i\omega\tau)}}{E^{*}_{LO}} \tag{2.16}$$

For visualizing the analysis steps described above, I generated synthetic data representing the signal and the local oscillator with an intensity ratio (signal/local oscillator) of 0.25. The τ is set to $250fs$. Figure 2.14 shows the steps for the calculation described above.

Spectral interferometry enables us to determine the relative phase between the signal and the local oscillator. However, the presence of the delay plate and the patterned region on the imaging mirror induces an uncertainty in the phase between the probe and the local oscillator [3]. This uncertainty is removed by the "global phasing" procedure, and the absolute phase of 2D spectrum is obtained. In the global phasing procedure, we phase the transient grating signal against the transient absorption spectrum which are measured at the same waiting time, t_2. For our experimental setup, we calculate the transient grating signal by adding the rephasing and the nonrephasing signals measured at t_1=0, whereas the transient absorption signal is measured separately within the same setup. We block one of the pump beams and the local oscillator to transform 2DES setup to the transient absorption setup. Both 2DES and the transient absorption measurements are performed consecutively without changing the sample position. The phasing procedure makes the real part of the transient grating signal equal to the transient absorption signal through multiplying it by a complex valued polynomial. This procedure aims to to find the complex valued polynomial satisfying this equality. Finding this polynomial is a minimization problem with an objective function given as below:

$$\begin{aligned} F &= Re\{A_{TG}(\omega-\omega_0)e^{i\theta(\omega)} - A_{TA}(\omega-\omega_0)\} \\ \theta(\omega) &= \phi_0 + (\omega-\omega_0)\phi_1 + (\omega-\omega_0)^2\phi_2 \end{aligned} \tag{2.17}$$

where A_{TG} and A_{TA} are the frequency resolved transient grating signal and the transient absorption signal respectively, and $\theta(\omega)$ is the unknown polynomial. In our model, a second order polyno-

mial in frequency describes the $\theta(\omega)$. The first order term, ϕ_1, can be interpreted as a correction accounted for the τ delay. The constant term (ϕ_0) and the second order term (ϕ_2) describe overall phase corrections. We solve for the unknown parameters of $\theta(\omega)$ using a nonlinear least squares algorithm.

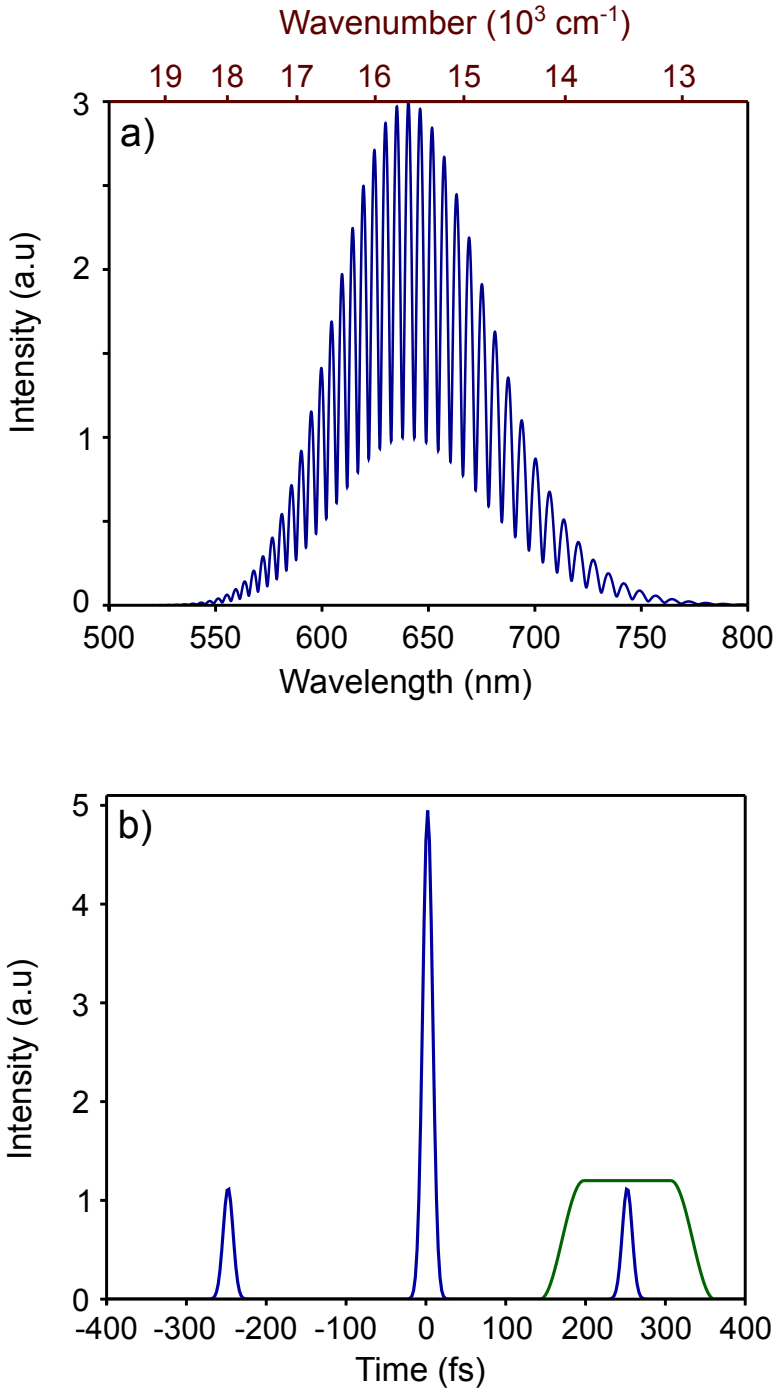

Figure 2.14: a) Spectral interferogram generated by synthetic data. b) The time domain trace of the inverse Fourier transform of the spectral interferogram in a (blue curve). Filter used to isolate the desired signal (green curve).

2.4 Experiment

We performed experiments on the PSII RC and Chl-a to collect the data presented in this thesis. The PSII RC sample is extracted from spinach following the protocol described in [27]. Further details about the extraction procedure can be found in [28]. The extracted sample is also referred to as the D1-D2-cyt b559. The sample is prepared in a solvent of buffer and glycerol at a 2:1 ratio(v/v). For Chl-a measurements, samples are derived from Anacystis nidulans algae purchased from Sigma Aldrich. Chl-a sample is prepared in a solvent of isopropanol and glycerol at a 1:1(v/v) ratio. The optical density of the PSII RC and Chl-a samples are ~0.29 and ~0.3 respectively. Both samples are kept in 380 μm thick sample cell and measurements are performed at 77K in an Oxford Microstat cryostat. I will provide detailed descriptions regarding the conditions of each experiment within the relevant chapters.

References

[1] Andrei Tokmakoff. *Nonlinear and Two Dimensional Spectroscopy Notes*. (2014).

[2] S. (Shaul) Mukamel. *Principles of nonlinear optical spectroscopy*. Oxford University Press, New York, (1995).

[3] David M. Jonas. Two-dimensional femtosecond spectroscopy. *Annual Review of Physical Chemistry*, **54**:425–463, (2003).

[4] Jennifer P. Ogilvie and Kevin J. Kubarych. *Chapter 5 Multidimensional Electronic and Vibrational Spectroscopy: An Ultrafast Probe of Molecular Relaxation and Reaction Dynamics*, volume Volume 57, pages 249–321. Academic Press, (2009).

[5] Robert W. Boyd. *Nonlinear Optics, Third Edition*. Academic Press, (2008).

[6] T. Wilhelm, J. Piel, and E. Riedle. Sub-20-fs pulses tunable across the visible from a blue-pumped single-pass noncollinear parametric converter. *Optics Letters*, **22**:1494–1496, (1997).

[7] M. Bradler, P. Baum, and E. Riedle. Femtosecond continuum generation in bulk laser host materials with sub-j pump pulses. *Applied Physics B*, **97**:561–574, (2009).

[8] A. M. Siddiqui, G. Cirmi, D. Brida, F. X. Krtner, and G. Cerullo. Generation of 7 fs pulses at 800 nm from a blue-pumped optical parametric amplifier at degeneracy. *Optics Letters*, **34**: 3592–3594, (2009).

[9] Franklin D. Fuller. *Observation of Coherences*. Thesis, (2014).

[10] John D. Hybl, Allison W. Albrecht, Sarah M. Gallagher Faeder, and David M. Jonas. Two-dimensional electronic spectroscopy. *Chemical Physics Letters*, **297**:307–313, (1998).

[11] Peifang Tian, Dorine Keusters, Yoshifumi Suzaki, and Warren S. Warren. Femtosecond phase-coherent two-dimensional spectroscopy. *Science*, **300**:1553–1555, (2003).

[12] M. L. Cowan, J. P. Ogilvie, and R. J. D. Miller. Two-dimensional spectroscopy using diffractive optics based phased-locked photon echoes. *Chemical Physics Letters*, **386**:184–189, (2004).

[13] T. Brixner, T. Mancal, I. V. Stiopkin, and G. R. Fleming. Phase-stabilized two-dimensional electronic spectroscopy. *Journal of Chemical Physics*, **121**:4221–4236, (2004).

[14] Erik M. Grumstrup, Sang-Hee Shim, Matthew A. Montgomery, Niels H. Damrauer, and Martin T. Zanni. Facile collection of two-dimensional electronic spectra using femtosecond pulse-shaping technology. *Optics Express*, **15**:16681–16689, (2007).

[15] Joshua C. Vaughan, T. Hornung, K. W. Stone, and Keith A. Nelson. Coherently controlled ultrafast four-wave mixing spectroscopy. *The Journal of Physical Chemistry A*, **111**:4873–4883, (2007).

[16] Patrick F. Tekavec, Geoffrey A. Lott, and Andrew H. Marcus. Fluorescence-detected two-dimensional electronic coherence spectroscopy by acousto-optic phase modulation. *The Journal of Chemical Physics*, **127**:214307, (2007).

[17] Ulrike Selig, Florian Langhojer, Frank Dimler, Tatjana Lhrig, Christoph Schwarz, Bjrn Gieseking, and Tobias Brixner. Inherently phase-stable coherent two-dimensional spec-

troscopy using only conventional optics. *Optics Letters*, **33**:2851–2853, (2008).

[18] Alexandra Nemeth, Jaroslaw Sperling, Jrgen Hauer, Harald F. Kauffmann, and Franz Milota. Compact phase-stable design for single- and double-quantum two-dimensional electronic spectroscopy. *Optics Letters*, **34**:3301–3303, (2009).

[19] Elad Harel, Andrew F. Fidler, and Gregory S. Engel. Real-time mapping of electronic structure with single-shot two-dimensional electronic spectroscopy. *Proceedings of the National Academy of Sciences*, **107**:16444–16447, (2010).

[20] Franz Milota, Craig N. Lincoln, and Jrgen Hauer. Precise phasing of 2d-electronic spectra in a fully non-collinear phase-matching geometry. *Optics Express*, **21**:15904–15911, (2013).

[21] Pooja Tyagi, Jonathan I. Saari, Brenna Walsh, Amin Kabir, Vincent Crozatier, Nicolas Forget, and Patanjali Kambhampati. Two-color two-dimensional electronic spectroscopy using dual acousto-optic pulse shapers for complete amplitude, phase, and polarization control of femtosecond laser pulses. *The Journal of Physical Chemistry A*, **117**:6264–6269, (2013).

[22] Jeffrey A. Myers, Kristin L. M. Lewis, Patrick F. Tekavec, and Jennifer P. Ogilvie. Two-color two-dimensional fourier transform electronic spectroscopy with a pulse-shaper. *Optics Express*, **16**:17420–17428, (2008).

[23] Sang-Hee Shim, David B. Strasfeld, Yun L. Ling, and Martin T. Zanni. Automated 2d ir spectroscopy using a mid-ir pulse shaper and application of this technology to the human islet amyloid polypeptide. *Proceedings of the National Academy of Sciences*, **104**:14197–14202, (2007).

[24] L. Lepetit, G. Chriaux, and M. Joffre. Linear techniques of phase measurement by femtosecond spectral interferometry for applications in spectroscopy. *Journal of the Optical Society of America B*, **12**:2467–2474, (1995).

[25] Franklin D. Fuller and Jennifer P. Ogilvie. Experimental implementations of two-dimensional fourier transform electronic spectroscopy. *Annual Review of Physical Chemistry*, **66**:667–690, (2015).

[26] Franklin D. Fuller, Daniel E. Wilcox, and Jennifer P. Ogilvie. Pulse shaping based two-dimensional electronic spectroscopy in a background free geometry. *Optics Express*, **22**: 1018–1027, (2014).

[27] Peter J. Leeuwen, Maaike C. Nieveen, Erik Jan Meent, Jan P. Dekker, and Hans J. Gorkom. Rapid and simple isolation of pure photosystem ii core and reaction center particles from spinach. *Photosynthesis Research*, **28**:149–153.

[28] Kristin Lee Morgenstern Lewis. *Two-Dimensional Electronic Spectroscopy of the Photosystem II D1D2-cyt.b559 Reaction Center Complex: Experiment and Simulation*. Thesis, (2012).

Chapter 3

Comparison of Coherent Dynamics in PSII RC and Chlorophyll a

This chapter presents 2DES studies of the PSII RC and chlorophyll a (Chl a) with a focus on coherent dynamics. This work is a continuation of the doctoral work of Franklin Fuller [1], with whom I published our observation of coherence in the PSII RC [2]. Our goal is to better understand the origin of coherent dynamics in the PSII RC by making a side by side comparison with Chl a. First, I will review an electronic dimer model (EDM), which has pure electronic coherence and a system of displaced harmonic oscillators (DHO) exhibiting pure vibrational coherence. Next, I will use diagrammatic perturbation theory to compare the experimental measurements with the theoretical models for the EDM, DHO as well as with a vibronic model. Having established the expected spectral signatures of coherent dynamics within these simple models, I compare coherent dynamics in the PSII RC and Chl a. Additionally, I briefly discuss the numerical simulations performed by our collaborators at Vilnus University on the PSII RC and Chl a to explain the origin and functionality of the coherent dynamics observed in these systems.

3.1 Electronic Dimer Model

The optical properties of a complex system depend on the the interaction between molecules and the intra-molecular/inter-molecular distance and orientation. When inter-molecular distances are comparable to the intra-molecular distances (tight packaging of molecules), the coupling between

the molecules can be significant, leading to delocalized eigenstates of the system commonly called excitons. Excitonic coupling modifies the optical properties of the system, causing splitting of absorption peaks and modifying peak in a manner that depends on the coupling strength and the relative orientation of the transitions dipoles. While excitonic coupling can be generalized to describe systems with large number of interacting molecules, herein we will focus on the electronic dimer model (EDM) with two molecules which are coupled to each other.

The EDM is a relatively simple system for understanding the electronic dynamics in the absence of a vibrational bath, and assumes that fast vibrations do not affect the electronic energy transfer [3]. The EDM was used to explain the coherent dynamics observed by Fleming and coworkers [4] in the Fenna-Matthews-Olson complex. The main motivation for using this model was its ability to calculate the electronic coherence dephasing times of the coherent dynamics they have observed. In the EDM model, two molecules, A and B, are coupled to each other electronically with coupling strength given by J. We start from a site basis to describe the two coupled chromophores, and show that electronic coupling gives rise to excitons delocalized on these chromophores. Here we assume molecule A and B have different ground states (G_1 and G_2), and single excited states (E_1 and E_2). Figure 3.1(a) shows the energy level diagram for the case where there is no coupling; the transition energies are given by ϵ_1 and ϵ_2 for A and B molecules. When a coupling J is introduced, the resulting energy level structure is described the excitonic basis $\{G, A, B, F\}$ as shown in Figure 3.1(b). The energies of these states are given by $\{0, \frac{1}{2}(\epsilon_1+\epsilon_2) - \triangle E_{EDM}, \frac{1}{2}(\epsilon_1+\epsilon_2) + \triangle E_{EDM}, \epsilon_1+\epsilon_2\}$ where $\triangle E_{EDM} = \sqrt{(\epsilon_1-\epsilon_2)^2 + 4J^2}$.

There are several methods used to calculate the absorption spectrum and the third order signal for the EDM, however we will not review the details of these calculations, instead we will use DPT to enumerate the oscillating contributions of the rephasing and nonrephasing 2D spectrum, as shown in Figure 3.2. One should note that the rephasing (nonrephasing) 2D spectrum has cross (diagonal) peaks with oscillatory behavior in the absence of excited state absorption (ESA). The anharmonicity of the second excited state informs about the exact location of the other peaks (involving ESA), which is typically blue shifted from the main absorption peak in the PSII RC and

Chl a.

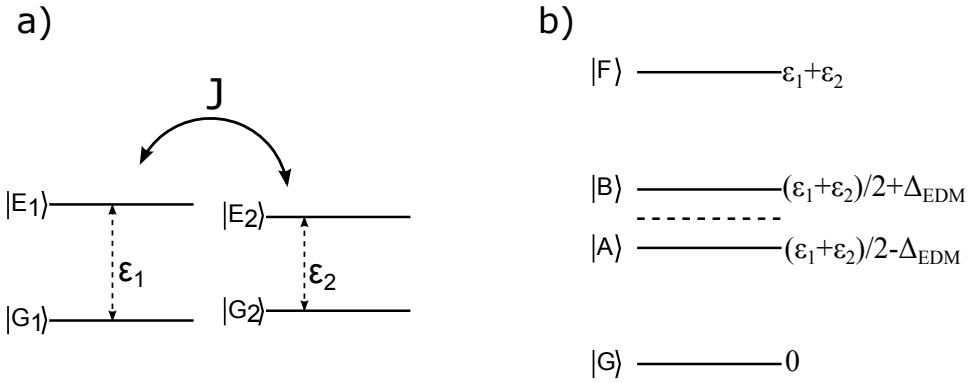

Figure 3.1: (a) Energy level diagram for two uncoupled chromophores. $G_{1(2)}$ and $E_{1(2)}$ are ground and excited electronic states respectively for molecule A(B). (b) Energy level diagram for Electronic Dimer Model with coupling constant J.

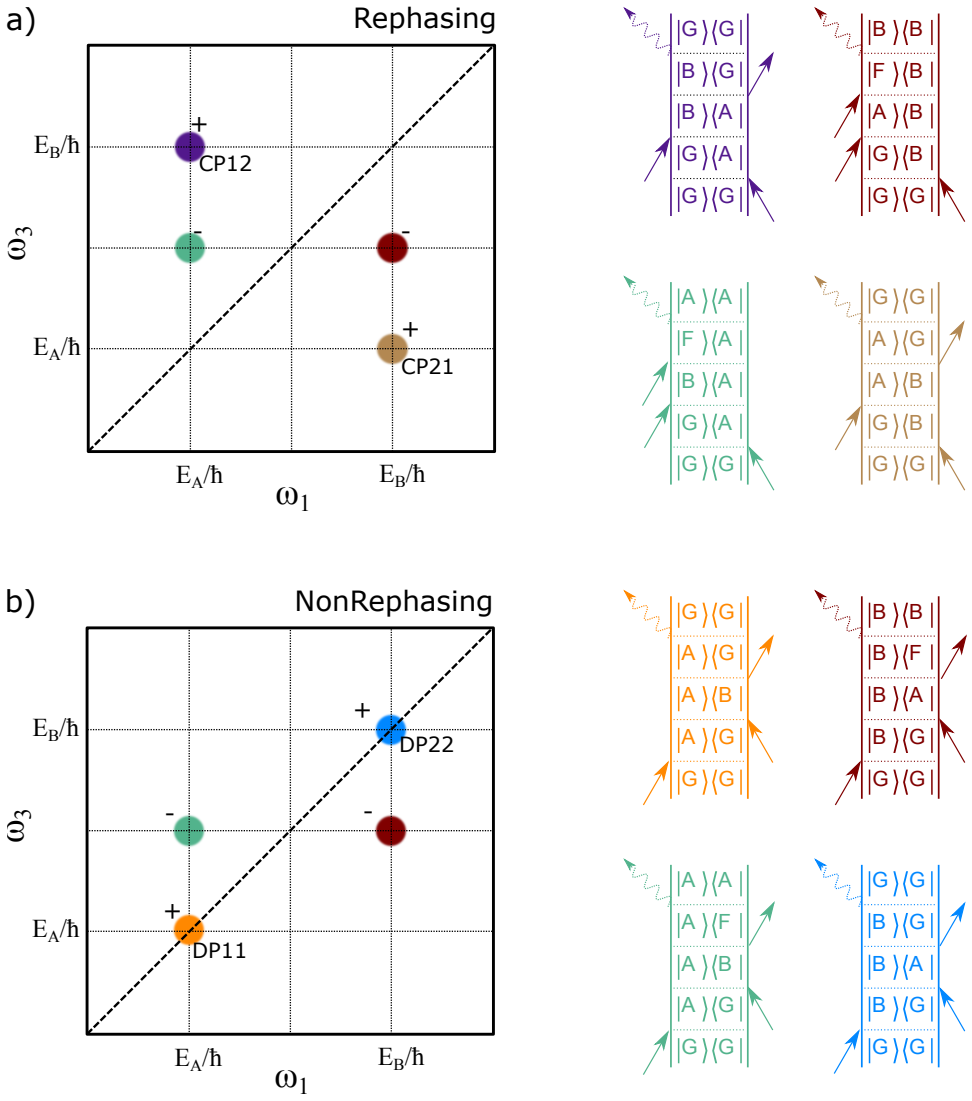

Figure 3.2: A subset of Feynman diagrams of the Electronic Dimer Model (EMD) which exhibit coherences during the t_2 interval. Peak positions predicted by diagrams are represented in Rephasing(a) and NonRephasing(b) 2D spectra. The relative phase of the oscillations predicted by the EDM is marked next to peak positions. The phase shift between "-" peaks and "+" peaks is π.

3.2 Displaced Harmonic Oscillator

The Displaced Harmonic Oscillator (DHO) is a generic model used to explain vibrational and electronic dynamics in single isolated molecules [3, 5]. The DHO rests on the Born-Oppenheimer timescale separation of fast electronic and slow nuclear motions. It is also used to explain absorption and fluorescence properties of single chromophores. In this model, the system is represented by two electronic states (ground and excited state) which are coupled to a single vibrational mode of frequency ω_0. This coupling makes the potential energy surface of both ground and excited state harmonic where the excited state energy surface is shifted by a Franck Condon dimensionless displacement d along the nuclear coordinate q. Eigenstates on both surfaces are represented by a one dimensional quantum oscillator model where the oscillator frequency is equal to vibrational mode included in the model. Then the eigenbasis is given by: $\{|g_m\rangle, |e_n\rangle, m, n = 0, 1, 2..\infty\}$ with eigenenergies $\{\epsilon_{g_m} = (m + 1/2)\hbar\omega_0, \epsilon_{e_n} = \omega_{eg} + (n + 1/2)\hbar\omega_0\}$ where ω_{eg} is the transition energy between the ground and the excited electronic states without any vibrational coupling.

The shift of the excited state in nuclear coordinates introduces unique absorption properties in this model. It breaks the symmetry between ground and excited state wavefunctions, that is $|g_m\rangle$ is not orthogonal to $|e_n\rangle$ and allowing transitions from $|g_m\rangle$ to $|e_n\rangle$. The absorption spectrum is dominated by the transition: $|g_0\rangle \rightarrow |e_0\rangle$ at ω_{eg} due to small displacement d. Other transitions will have smaller amplitude and be shifted by ω_0 compared to the main transition leading to a series of side peaks next to the main peak called a vibronic progression.

Within the DHO model the energy levels are equally spaced at ω_0 on both the ground and the excited states. This equal spacing creates signals oscillating at ω_0 at different locations in the 2D rephasing and nonrephasing spectra. Following the approach of Butkus et al, we employ DPT to identify the pathways describing oscillatory behavior in the rephasing and the nonrephasing signals [6]. We restricted the possible contirbutions by including only the first excited vibrational states on the ground and the excited state energy surfaces: $|g_0\rangle$,$|g_1\rangle$,$|e_0\rangle$,$|e_1\rangle$ in the model. Moreover, we assumed that the system is in the ground state $|g_0\rangle$ before any excitation. The excitation bandwidth is selected such that it allows any possible transitions from the ground to the excited state energy

surface or vice versa. Transitions between two vibrational states on a single electronic surface (ground or excited) are not within the excitation bandwidth.

Figure 3.4 shows the Feynman diagrams contributing to the oscillating signals in the rephasing and the nonrephasing 2D spectra. Both the rephasing and nonrephasing spectra are asymmetric with respect to the diagonal axis, where the rephasing has a "chair" pattern and the nonrephasing has an inverted "chair" pattern. There are eight Feynman pathways contributing to the oscillating signals where the half of them have signals from vibrational coherence on the ground state and the other half have signals from vibrational coherence on the excited state. CP12 (LP10) and LP10 (CP12) have signals from the vibrational coherence on the excited and ground state energy surfaces respectively in the rephasing (nonrephasing) spectra.

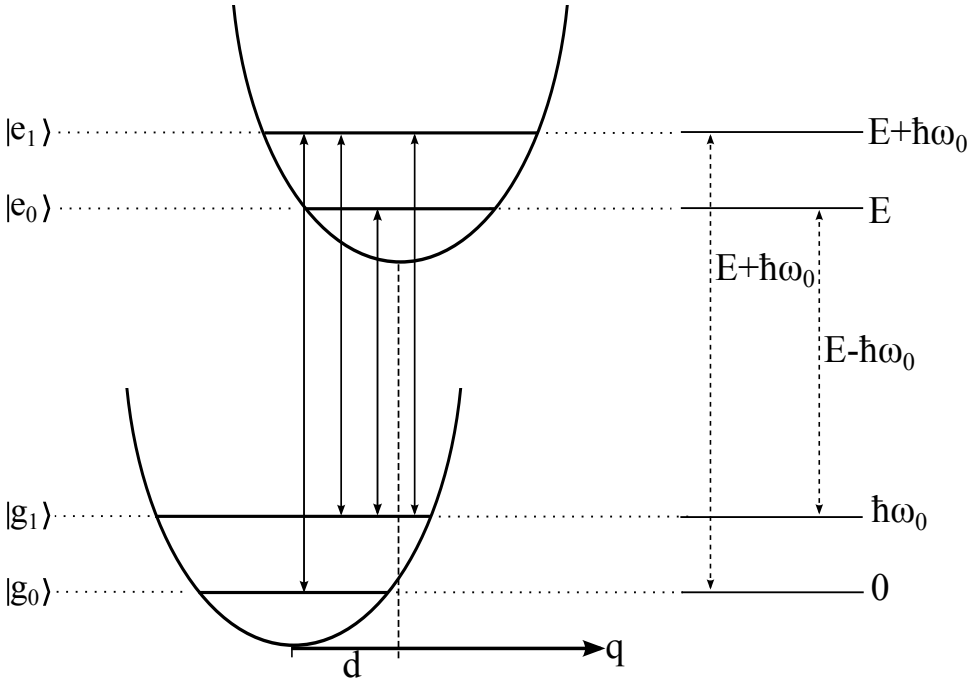

Figure 3.3: Energy level structure for the displaced harmonic oscillator model. q is the nuclear coordinate. Only first and second vibrational levels are shown on both ground and excited potential energy surfaces. Arrows show the allowed transitions. A simplified energy diagram is represented on the right side. Adapted from [3, 5].

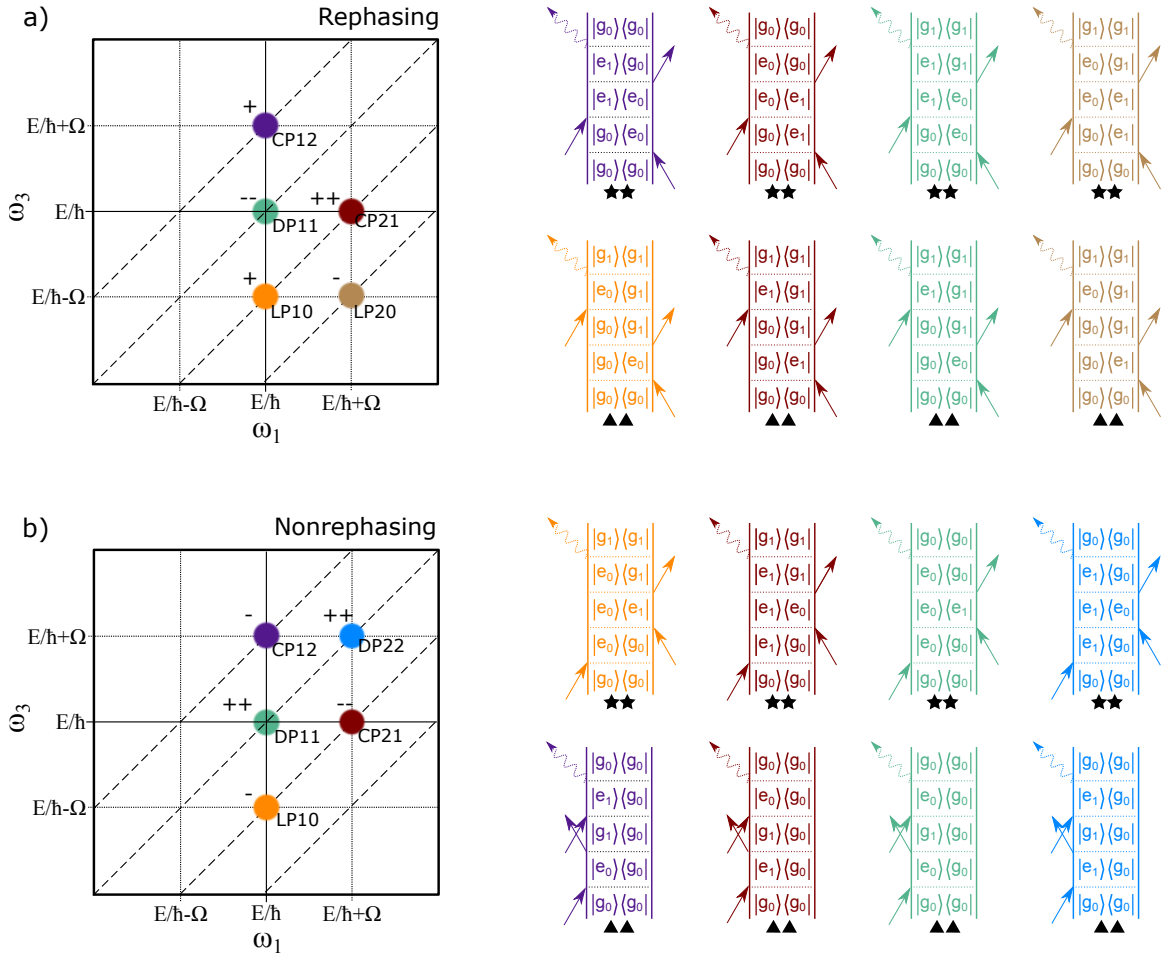

Figure 3.4: Feynman diagrams of Displaced Harmonic Oscillator which has coherences during the t_2 interval. Peak positions predicted by diagrams are represented in Rephasing (a) and NonRephasing (b) 2D spectra. The relative phase of the oscillations predicted by model is marked next to peak positions. The phase shift between "-" peaks and "+" peaks is π. Double star (★★) and double triangle (▲▲) marks the diagrams having coherences on the ground and excited state during the t_2 interval respectively. Adapted from [3, 5].

3.3 Phase Variations of Coherences

In the previous section, we used diagramatic perturbation theory (DPT) to find out the peaks which oscillate during the t_2 interval for the DHO and the EDM. Here we will show how the phase of these peaks differs and their overall effect on the 2D spectra. The transitions between the states are described by Lorentzian line shape functions, then we can formulate the response function in Equation 2.2 as:

$$S_{2D}(\omega_1, t_2, \omega_3) = \sum_n \pm A_n \theta(t_2) \frac{e^{-\gamma_2 t_2 - i\varepsilon_2 t_2}}{(\gamma_1 + i(\varepsilon_1 - \hbar\omega_1))(\gamma_3 + i(\varepsilon_3 - \hbar\omega_3))} \tag{3.1}$$

where A_n is a complex quantity with contributions from transition dipole moments and electric fields, $\theta(t_2)$ is a heaviside step function, ε_n and γ_n are transition energies and decay constants of the n^{th} transition respectively [3]. $\pm$ shows the signal type, which is + for ground state bleach and stimulated emission, and is - for excited state absorption. The real part of S_{2D} for a single pathway is given by:

$$\begin{aligned} S_{2D,n}(\omega_1, t_2, \omega_3) &= \frac{A_n e^{-\gamma_2 t_2}}{\sqrt{(\gamma_1^2 + \Delta_1^2)(\gamma_3^2 + \Delta_3^2)}} cos(\varepsilon_2 t_2 + \varphi) \\ \varphi &= Arg[(\gamma_1 - i\Delta_1)] + Arg[(\gamma_3 - i\Delta_3)] \\ \Delta_n &= \varepsilon_n - \hbar\omega_n \quad n = 1, 3 \end{aligned} \tag{3.2}$$

The $cos(\varepsilon_2 t_2 + \varphi)$ term in Equation 3.2 describes the oscillatory behavior observed in our 2D spectra, and φ represents phase variations among (ω_1, ω_3) pairs. The relative phases of the peaks for the DHO and the EDM estimated by DPT are given in Figure 3.4 and Figure 3.2. This relation is valid only for the points where $\Delta_{1,3} = 0$. The contribution from a single pathway, $S_{2D,n}$, produces varying amplitude and phase in the 2D spectrum, and the summation of different pathway contributions yields phase differences ranging from 0 to π.

A number of experimental and theoretical studies have reported phase differences between the oscillatory peaks. Butkus and co-workers used DPT to predict 0 and π phase shifts between

the oscillatory peaks [3]. Engel and co-workers reported experimental verification of the phase differences which are neither 0 nor π [7]. Later, various models accounting for the interaction between the electronic and the vibrational states have been shown to cause phase shifts between 0 and π [8, 9].

3.4 A Vibronic Model

The EDM and DHO are two popular models that have been used to explain coherent dynamics observed in 2D spectra. A more appropriate model for photosynthetic systems is a vibronic model in which the electronic excitations are coupled to intramolecular vibrations. The influence of electronic and vibrational coherent dynamics on each other and the coupling between these resonances have been investigated [8]. It is clear that vibronic models cannot be simply explained by the superposition of vibrational and electronic models. Herein, we use the simplest vibronic model in which an electronic dimer is coupled to a single vibrational mode to predict the coherent spectral signatures in the 2D spectrum that arise due to vibronic coupling. Figure 3.5 shows the evolution of energy structure of two uncoupled monomers to that of a vibronic model in three steps: 1.Two uncoupled monomers, 2. Electronic Dimer Model, 3. The dimer coupled to a vibrational model. To reduce the complexity of 2D spectra we limit the number of vibrational levels on each electronic level to one. Figure 3.6 shows a subset of Feynman diagrams predicted by this model and the 2D rephasing signal generated by these diagrams. Vibronic models have significant potential to explain complex phase and amplitude relations of coherent dynamics throughout the 2D spectra [8].

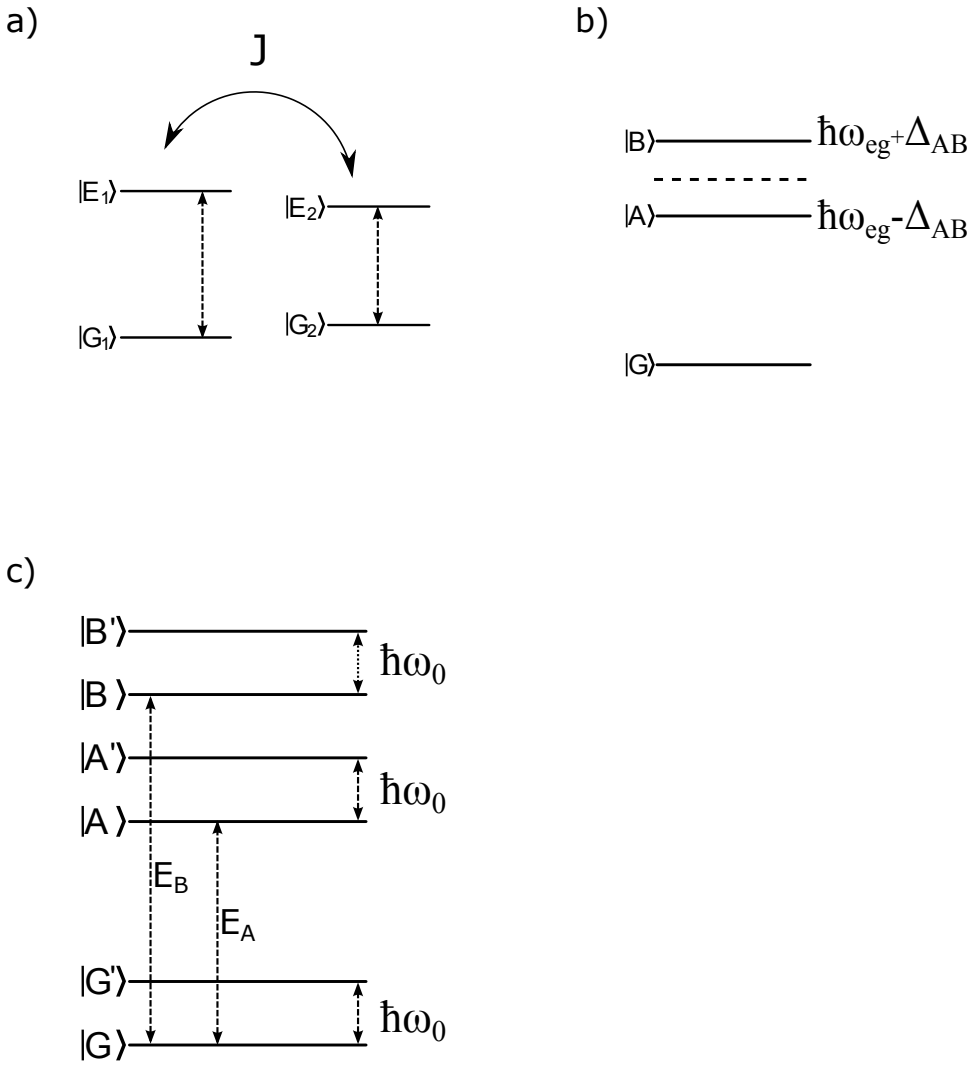

Figure 3.5: (a) Energy level diagram for two uncoupled chromophores. $G_{A(B)}$ and $E_{A(B)}$ are ground and excited electronic states respectively for molecule A(B). (b) Energy level diagram for Electronic Dimer Model with coupling constant J. (c) Energy level diagram for an Electronic Dimer coupled to single vibrational mode (vibronic model)

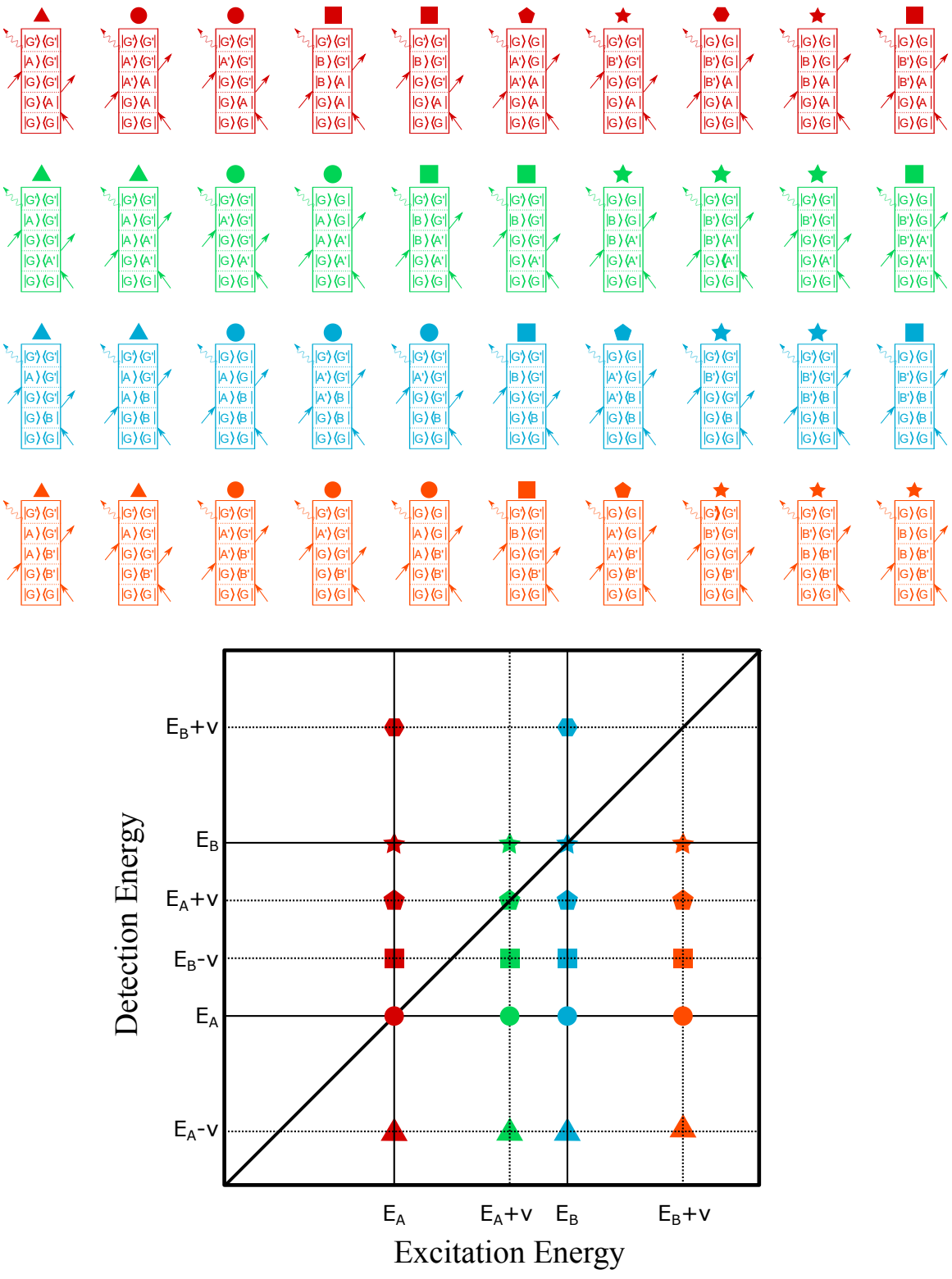

Figure 3.6: A subset of Feynman diagrams for an electronic dimer with single vibrational state on each electronic state. The rephasing spectra shows the contributions of each pathway with a shape and color code.

3.5 Experimental Observations of Coherences

We performed 2DES experiments on the PSII RC and Chl a using the experimental setup described in Chapter 2. For all the experiments described here, the pump and probe NOPAs were tuned to a central wavelength of 660 nm and 650 nm, respectively. The pump and probe NOPAs delivered 7 nJ and 10 nJ pulses at the sample cell. These energies correspond to less than 4% excitation per reaction center in PSII RC sample to avoid exciton annihilation effects [10, 11].

After compression the pump and probe were 12 and 15 fs in duration. We scanned t_1 delay with 10fs steps through $0 \leq t_1 \leq 390 fs$ for each 2D measurement while t_1 was phase-locked at 660 nm. We used a six-phase-cycling scheme to isolate rephasing and nonrephasing signals and to suppress various interference scatter terms. We averaged the signal for 750 msec per t_1 delay, requiring 30sec for a single 2D spectrum. The waiting time, t_2, was scanned through $80 \leq t_2 \leq 1920$ fs with a 10 fs interval. Measurements done at earlier times, t_2 <80 fs were not used to avoid coherent artifacts due to pulse overlap. A mechanical chopper in the probe path suppresses pump scatter terms with a duty cycle of 90%. The total data acquisition time was ~90min and the sample was not moved during measurements. We kept the experimental scheme same for the PSII RC and Chl a measurements. Changes in the NOPA spectrum from day to day were negligible. Figure 3.7 show the absorptive 2D spectrum of the PSII RC and Chl a at t_2=300 fs waiting time.

The 2D spectra measured at $t_2 = 80, 90, ..., 1920$ fs, form a three dimensional data stack: $S(\omega_1, t_2, \omega_3)$. To extract the information about coherent dynamics in the system we fit dominant population dynamics in this 3D data stack. The time trace for each pixel at 2D spectra was allowed to fit exponential functions with the same decay time τ_n but varying linear coefficients $a_{m,n}$. The equation for fitting is given by:

$$s_m(t_2) = \sum_n a_{m,n} \exp(-t_2/\tau_n) \tag{3.3}$$

where m denotes the number corresponding to a given (ω_1, ω_3) point in the 2D spectrum. We used non-linear least squares to choose the best model among models with different exponential

decay components. Nonlinear least squares is a widely used approach to fit observations to models which are not linear with respect to independent parameters. The approach is based on minimizing residuals which are the difference between observations and a model function. Here we also vary the number of exponential decays to select the best model which gives minimum residuals. We choose to fit all pixels to the same exponential decays instead of fitting each pixel independently. Once the fit is optimized we use it to subtract the population kinetics from the overall signal. The remaining signal is Fourier transformed along t_2 axis to isolate weak oscillatory signals, producing a three dimensional frequency solid, $S(\omega_1, \omega_2, \omega_3)$, which has rich information about coherence frequency content, amplitude and phase. To reveal the frequency of the oscillations present during the t_2 time interval, we take the Frobenius norm of the 3D frequency solid, summing over the absolute magnitude, squared, of each 2D point (ω_1, ω_3) and then taking the square root:

$$A_{Frobenius}(\omega_2) = \sqrt{\sum_{i=1} \sum_{j=1} (\mid S(\omega_{1,i}, \omega_2, \omega_{3,j})) \mid^2} \tag{3.4}$$

$A_{Frobenius}$ is a summary of frequency amplitude information throughout the entire 2D spectrum.

A different representation of the 3D frequency solid is looking at the real part of 2D spectra at different ω_2 values which shows the distribution of the oscillations throughout the 2D spectrum. This representation is called a "Fourier Maps" or "Amplitude Coherence Map" and is useful to compare with the generic models we introduced in Sections 3.1 and 3.2. A similar representation can be made to observe the distribution of the phase of oscillations throughout the 2D spectrum, yielding "Phase Coherence Map", Figure 3.8 depicts the post data processing steps.

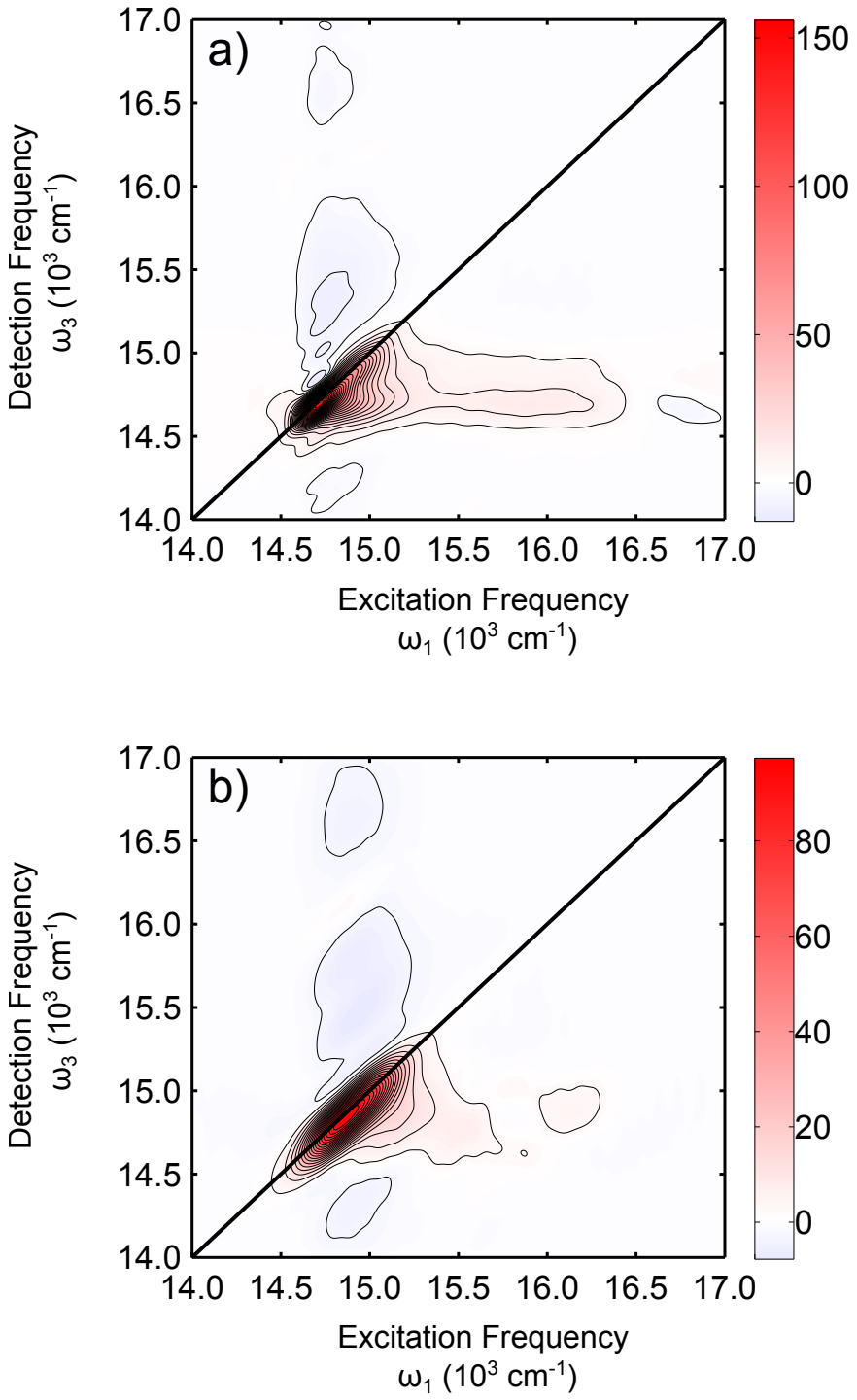

Figure 3.7: Real absorptive 2D spectra at t_2=300fs (a) PSII RC (b) Chl a.

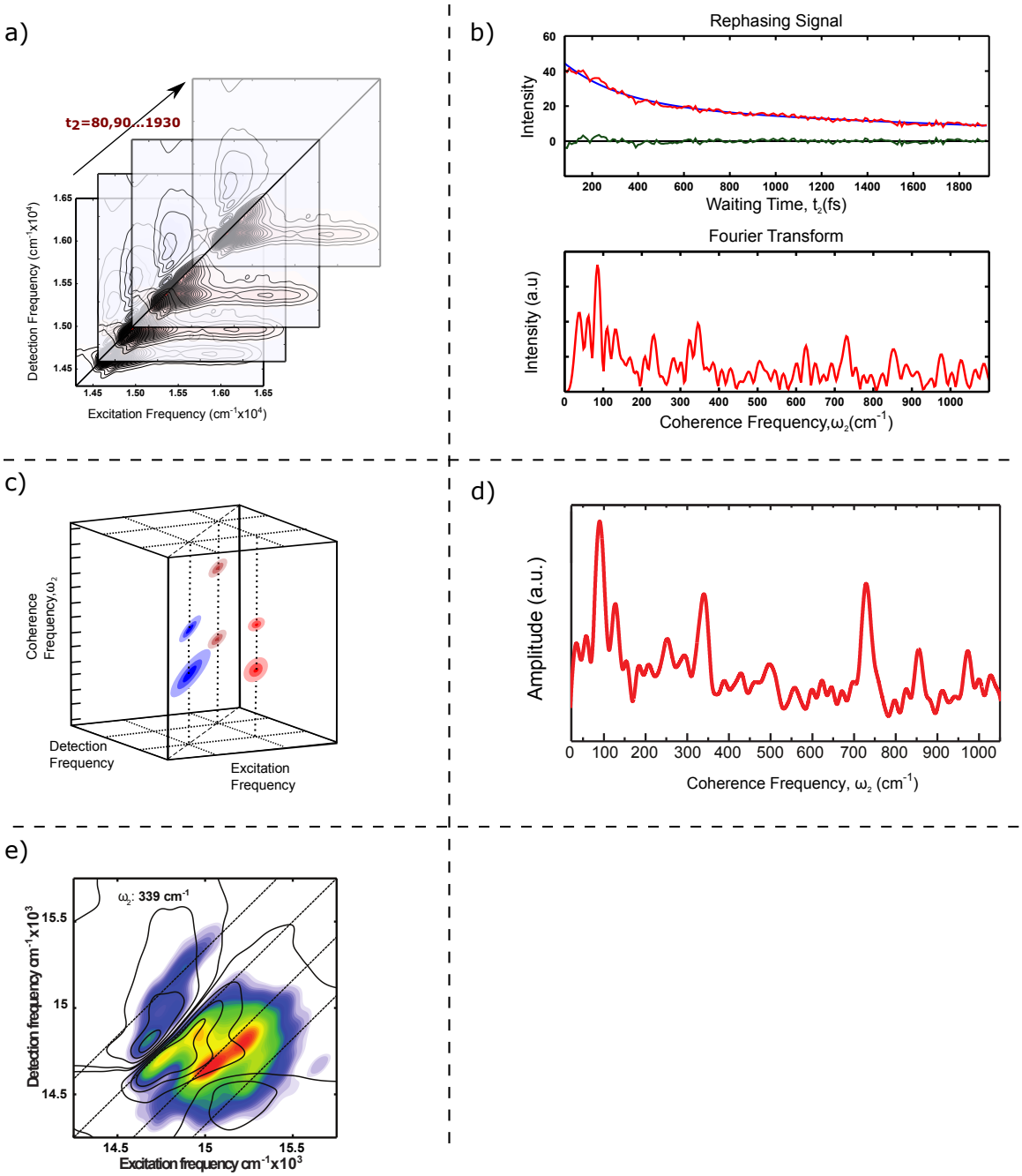

Figure 3.8: Post data processing steps: (a) Collecting of 2D spectra at different t_2 values. (b) Fitting the population kinetics to each (ω_1, ω_3) point in 2D spectra and extracting frequency content. (c) Generating the 3D data structure, $S_{2D}(\omega_1, \omega_2, \omega_3)$ (d) Summary spectrum I: Frobenius Spectra, (e) Summary spectrum II: Coherence amplitude maps, generated from $S_{2D}(\omega_1, \omega_2, \omega_3)$. 2DES data on PSII RC is used to produce figures in (a),(b),(d),(e).(Courtesy of V.Policht, Figure 3.8c)

3.6 Comparison of Coherent Dynamics

The Frobenius spectra for the PSII RC and Chl a are shown in Figure 3.9(e). Exciton difference frequencies from the Novoderezhkin and Gelzinis excitonic model for the PSII RC, as well as vibrational frequencies reported for these systems are also shown in Figure 3.9. The majority of the observed modes in both systems are similar to the exciton difference frequencies and vibrational frequencies. Here we focus on three dominant modes ω_2=~240,340,740 cm^{-1} observed both in PSII RC and Chl a, studying similarities and differences between these modes.

The amplitude coherence map at ~740 cm^{-1} for the PSII RC and Chl a are shown in Figure 3.10c and 3.10d respectively. They both look similar and show vibrational character, with peak positions in agreement with the chair diagram for the DHO model. The amplitude of LP10 is significantly lower in PSII RC and CP21 is shifted slightly upwards in Chl a.

The phase coherence maps for the PSII RC and Chl a show greater deviations for ~740 cm^{-1} within the DHO model. A vibrational mode is expected to have CP21 and LP10 oscillate in phase, while LP20 and DP11 and LP20 and CP12 should oscillate out of phase. We calculated the phase of each peak by averaging over a $\Delta_{\omega 1}, \Delta_{\omega 3}$ (10 cm^{-1} $\times$ 10 cm^{-1}) region around the peak position to make a more accurate comparison and report these values in Table 3.1 and Table 3.2. Chl a shows vibrational character in phase coherence maps also. The phase on diagonal lines also show differences throughout the coherence maps. The phase on d$--$ changes slightly, LP10 and CP21 oscillate with a 0.25π relative phase shift. The phase difference between LP10 and LP is 0.8π. The phase shift between LP20 and CP12 is expected to be π while it is found to be 0.64π. The phase shift is also different than the expected one for CP12 and DP11 pair. It is found to be 0.56π instead of π shift. This can be partially explained by the excited state absorption feature around CP12 position.

The phase variation on $d--$ is larger in the PSII RC. LP10 and CP21 oscillate with a 0.43π shift. LP10 and LP20 has a 0.48π shift, while CP12 and LP20 has a 0.36π shift. The deviation from the vibrational model can be explained by the presence of excited state absorption at CP12 peak, distortions due to sample geometry, and laser intensity differences across the spectrum.

The amplitude coherence maps for ~240 cm^{-1} and ~340 cm^{-1} modes look quite different for Chl a and PSII RC, Figure 3.11 and Figure 3.12. For Chl a, we expect both modes would have vibrational character due to monomeric structure of it. However we observe three significant features centered between diagonal lines and the amplitudes are not centered on the expected peak positions. The features between $d-$ and $d--$ are not explained by the DHO model. The coupling between Q_x and Q_y band in Chl a could cause deviations from purely vibrational behavior but there is no study yet to support this interpretation.

The amplitude coherence maps for ~240 cm^{-1} and ~340 cm^{-1} modes for the PSII RC show significant amplitude on $d-$ which cannot be explained by purely electronic coherence. The significant amplitude between $d+$ and d in both maps cannot be understood by purely vibrational coherence, but is consistent with a vibronic model. The spectral overlap between peaks is reduced in the ~340 cm^{-1} mode so the peaks on $d--$ are more isolated compared to those for the ~240 cm^{-1} mode. The intensity difference among the peaks may be explained by different transition dipole strengths.

The phase coherence maps of Chl a for ~240 cm^{-1} and ~340 cm^{-1} modes look very similar. In both cases, the phase is mostly constant along the diagonal lines. LP10 and LP20 oscillate with $0.71(0.80)\pi$ phase shift in the ~240(340) cm^{-1} mode. The difference between CP12 and LP20 is $0.60(0.59)\ \pi$, while it is $0.12(0.16)\pi$ in ~240(340) cm^{-1} mode.

PSII RC phase coherence map for ~240 cm^{-1} and ~340 cm^{-1} modes also show features which are not explained by a pure vibrational or electronic model. For example, the phase of the feature between d and $d-$ in the ~240 cm^{-1} map is shifted by $\sim\pi$ with respect to the phase of CP12. The ~340 cm^{-1} mode shows significant variations in phase on $d-$ and there is a 0.46π shift between LP10 and LP20.

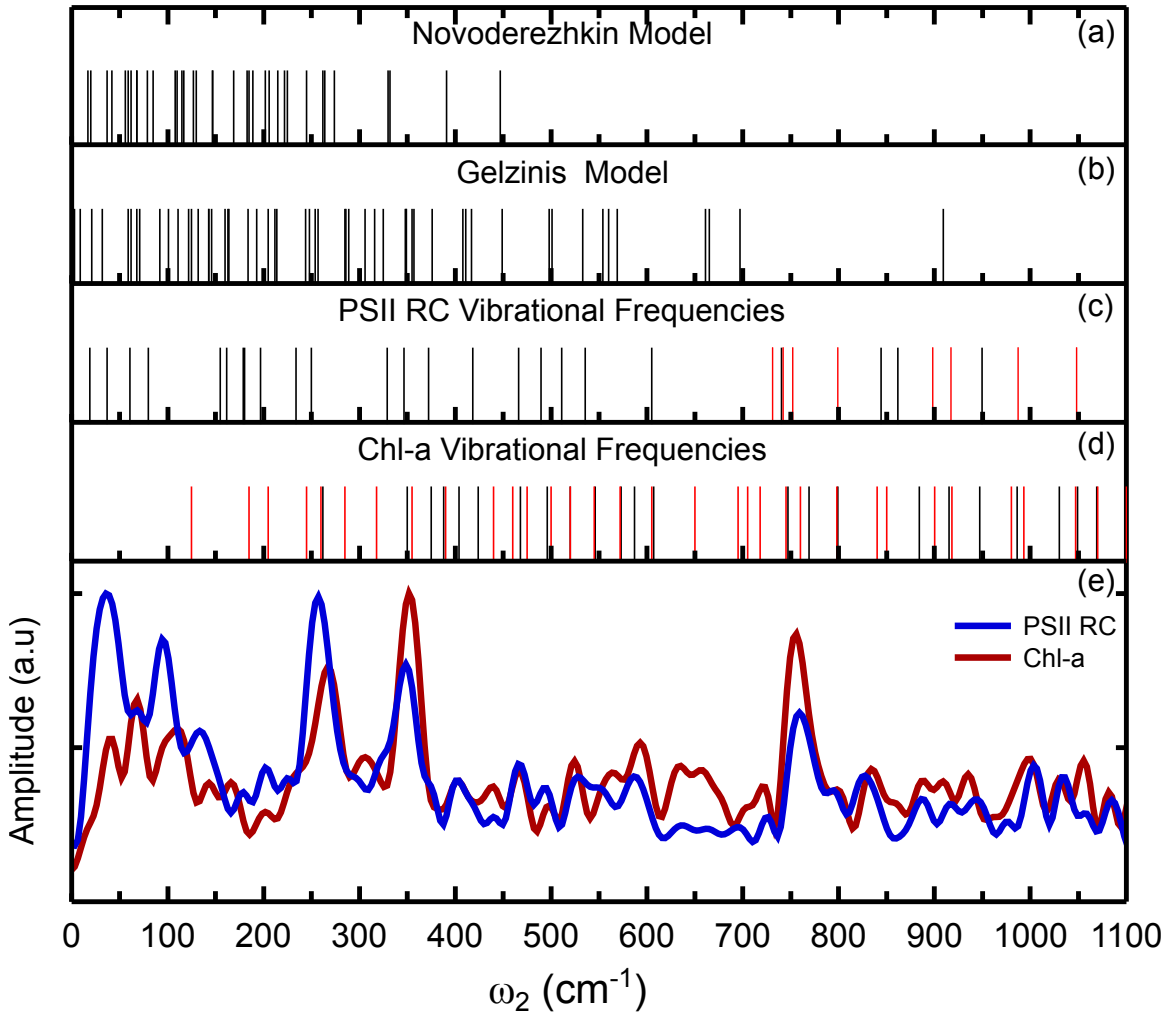

Figure 3.9: Exciton difference frequencies in PSII RC:(a)Novoderezkhin model [12]. (b)Gelzinis model [13]. (c)Vibrational frequencies in PSII RC: Modes reported by fluorescence line narrowing (black) and surface enhanced Raman experiments(red) [14, 15]. (d)Vibrational frequencies in Chl a: Modes reported by fluorescence line narrowing(black) and surface enhanced Raman experiments(red) (e) Frobenius Spectra for PSII RC and Chl a.

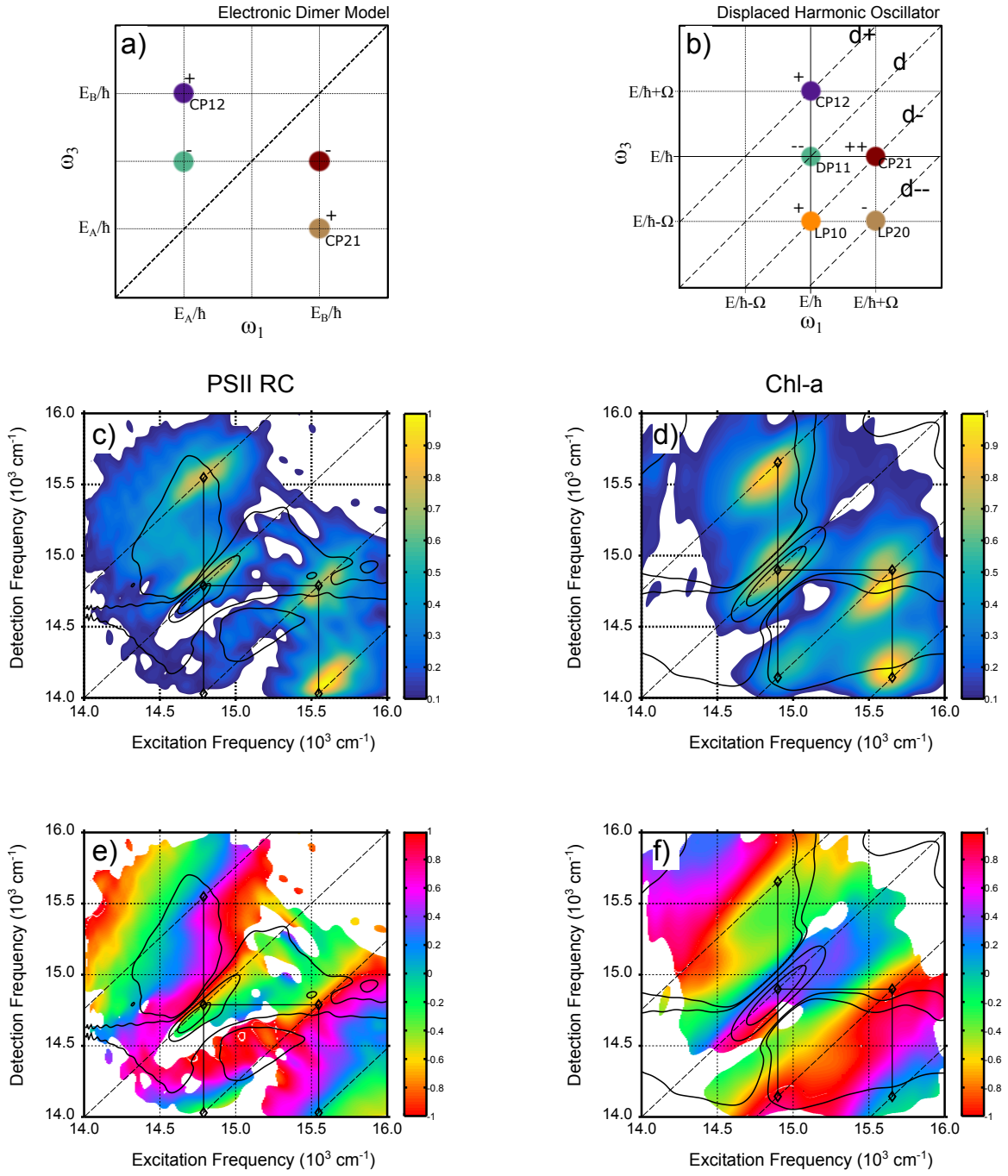

Figure 3.10: (a) Cartoon rephasing coherence map for Electronic Dimer model. (b) Cartoon rephasing coherence map for Displaced Harmonic Oscillator model. Rephasing amplitude coherence maps for ω_2=~740 cm^{-1} mode: (c) PSII RC. (d) Chl a. Rephasing phase coherence maps for ω_2=~740 cm^{-1} mode: (e) PSII RC. (f) Chl a.

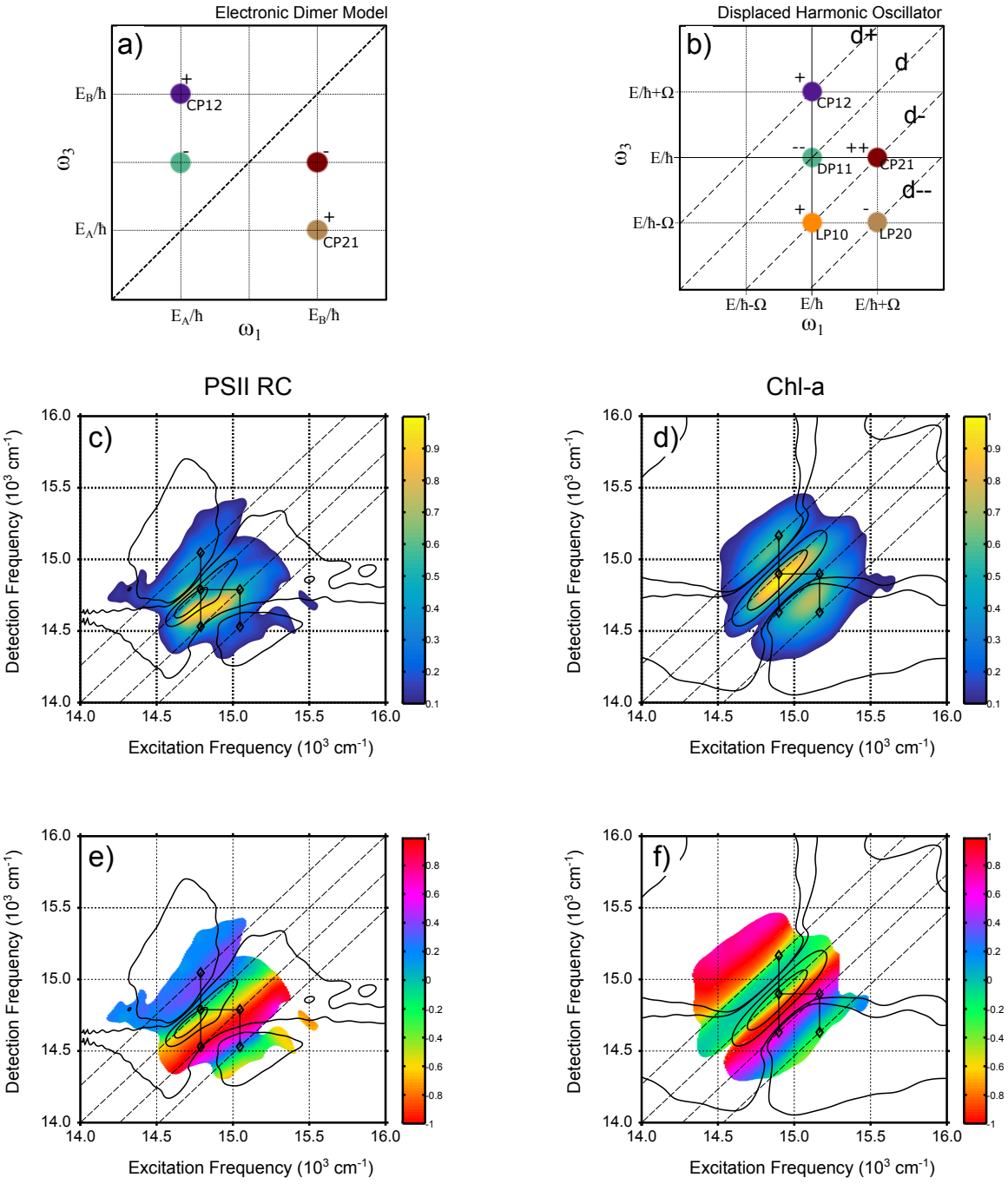

Figure 3.11: (a) Cartoon rephasing coherence map for Electronic Dimer model. (b) Cartoon rephasing coherence map for Displaced Harmonic Oscillator model. Rephasing amplitude coherence maps for ω_2=~240 cm^{-1} mode: (c) PSII RC. (d) Chl a. Rephasing phase coherence maps for ω_2=~240 cm^{-1} mode: (e) PSII RC. (f) Chl a.

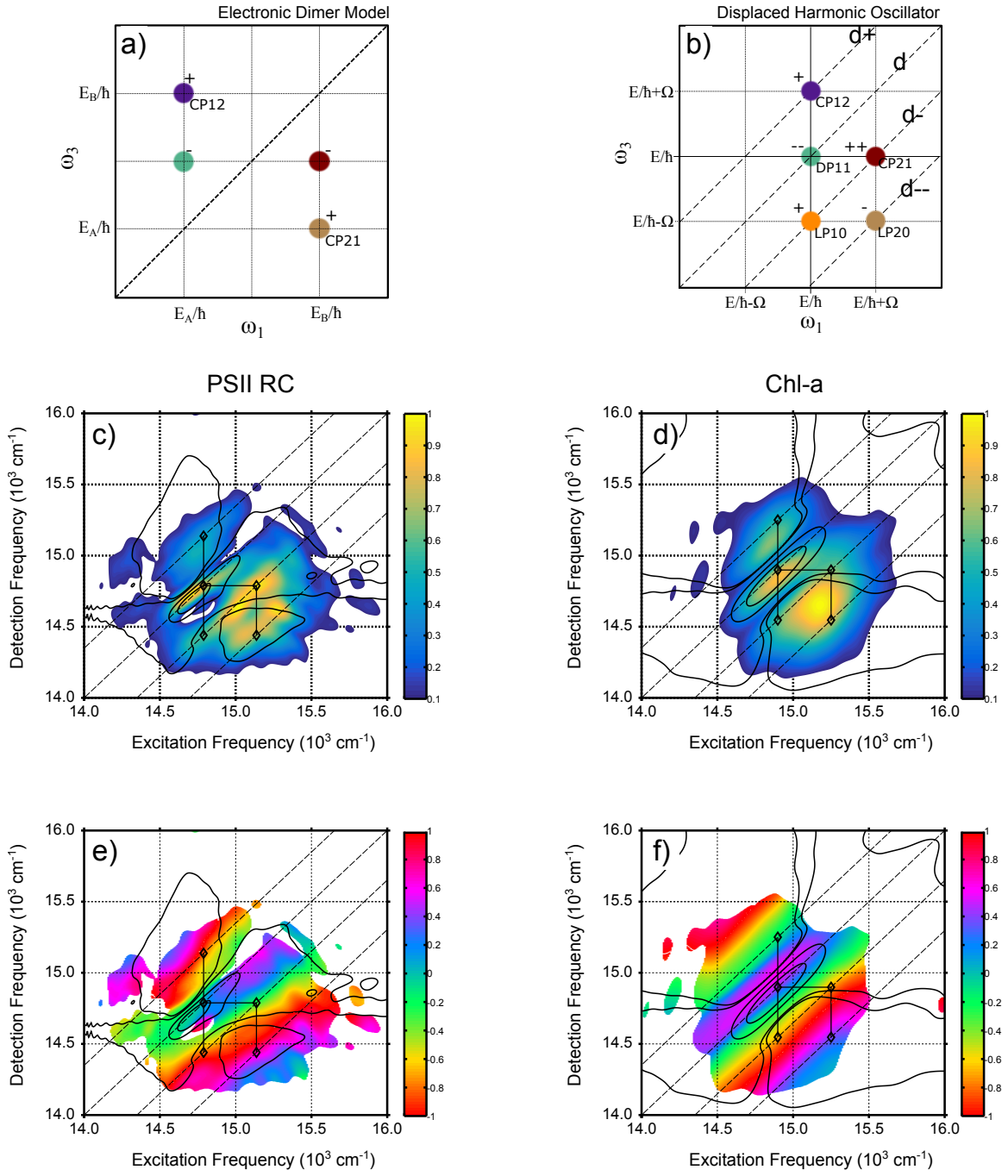

Figure 3.12: (a) Cartoon rephasing coherence map for Electronic Dimer model. (b) Cartoon rephasing coherence map for Displaced Harmonic Oscillator model. Rephasing amplitude coherence maps for ω_2=~340 cm^{-1} mode: (c) PSII RC. (d) Chl a. Rephasing phase coherence maps for ω_2=~340 cm^{-1} mode: (e) PSII RC. (f) Chl a.

Chl a	240 cm^{-1} (π)	340 cm^{-1} (π)	740 cm^{-1} (π)
DP11	-0.03	0.50	0.054
CP12	0.96	-0.55	-0.92
LP10	-0.92	-0.33	-0.77
CP21	-0.80	-0.17	-0.51
LP20	0.36	0.85	0.42

Table 3.1: The phases of different peaks throughout the phase coherence maps of Chl a. The values are shown for three dominant modes divided by π.

PSII RC	240 cm^{-1} (π)	340 cm^{-1} (π)	740 cm^{-1} (π)
DP11	-0.10	0.04	-0.62
CP12	0.33	-0.85	0.39
LP10	0.93	-0.81	-0.43
CP21	-0.83	-0.27	-0.87
LP20	0.14	0.72	0.04

Table 3.2: The phases of different peaks throughout the phase coherence maps of the PSII RC. The values are shown for three dominant modes divided by π

3.7 Simulations

We have collaborated with the Abramavicius Group for theoretical simulations of the PSII RC and Chl a to investigate the origins of the coherent dynamics in these systems. This section will disclose our simulation results on Chl a for the first time, whereas the simulations regarding the PSII RC as a part of our earlier study [2] but will be briefly summarized here for convenience.

The P_{D1} and P_{D2} pigment pair has the largest electronic coupling within the PSII RC, thus this pair has been chosen to capture any relevant contributions to the PSII RC coherent dynamics. In simulations, this pigment pair is modeled as a special dimeric pair which is coupled to discrete vibrational modes using the approach developed by Butkus and co-workers [3, 6]. For comparison of the experimental results with theory, coherence maps are generated from the calculated 2DES signals. The details of the model and the method for calculations are beyond the scope of this

thesis and can be found in [2] and [3, 6, 16, 17] respectively.

Figure 3.13a shows the simulated amplitude coherence map for the ω_2~740 cm^{-1} mode under the condition that this mode is coupled to the dimeric pair. The vibronic model involving a high frequency mode (e.g ~740 cm^{-1}) is expected to exhibit vibrational characteristic ("chair" pattern in the amplitude coherence maps). Both the experimental (Figure 3.10c) and simulated (Figure 3.13a) amplitude coherence maps are in agreement with this expectation and show vibrational spectral signatures. We also examined the case when the dimeric special pair is coupled to the ~240 cm^{-1} and ~340 cm^{-1} modes. The simulated amplitude coherence maps are shown in Figure 3.13b and Figure 3.13c for ω_2~340 cm^{-1} and ω_2~240 cm^{-1} modes respectively. The experimental results and the simulations are in very good agreement, and both suggest these two modes have vibronic origins. A more detailed discussion about the simulated amplitude coherence maps under different coupling conditions can be found in our recent study [2].

Additionally, we have performed theoretical simulations on Chl a based on the approach developed by Butkus and co-workers [6]. The model includes a monomer which is described by an energy level composed of one ground state, two excited state levels, and one double-excited state level. The DHO is used to simulate the Q_x and Q_y transitions in the absence of coupling between these transitions. The monomer is coupled to the environment (the vibrational modes) which is described by the spectral density function:

$$C''(\omega) = C''_{fast}(\omega) + C''_{slow}(\omega) + C''_{Q_y}(\omega) + C''_{Q_x}(\omega) \tag{3.5a}$$

$$C''_{fast/slow}(\omega) = \lambda_{fast/slow}\frac{\omega}{\omega_\nu}exp(\frac{-\omega}{\omega_\nu}). \tag{3.5b}$$

Here, $C''_{fast}(\omega)$ and $C''_{slow}(\omega)$ describe the homogeneous and inhomogeneous broadening respectively. In the simulations ω_ν is 500 cm^{-1} (0.1 cm^{-1}) for C''_{fast} (C''_{slow}). $C''_{Q_y}(\omega)$ and $C''_{Q_y}(\omega)$ identify the vibrational modes coupled to the monomer, and are given as:

$$C''_{Q_y/Q_x}(\omega) = \sum_i \frac{4\omega^3\omega_{\nu i}\gamma_i s_i}{(\omega^2 + \omega^2_{\nu i} + \gamma_i)^2 - 4\omega^2\omega^2_{\nu i}} \tag{3.6a}$$

where s_i, $\omega_\nu i$, and γ_i are the intensity, frequency and the damping rate for the i-th vibrational mode respectively.

Figure 3.14 shows the simulated amplitude coherence maps for Chl a. The amplitude coherence map for the ω_2~740 cm^{-1} mode is in good agreement with the experimental one, as shown in Figure 3.10d. They both exhibit the "chair" pattern which is a characteristic of vibrational coherence. On the other hand, simulated amplitude coherence maps for the ω_2~340 cm^{-1} and ω_2~240 cm^{-1} modes also show significant amplitude between the d- and d- - lines. A similar behavior is present in the experimental coherence maps for these modes. While the DPT doesn't predict oscillatory peaks between d- and d- - for the displaced harmonic oscillator, one should note that the spectral overlap can alter the "chair" pattern significantly for low frequency modes.

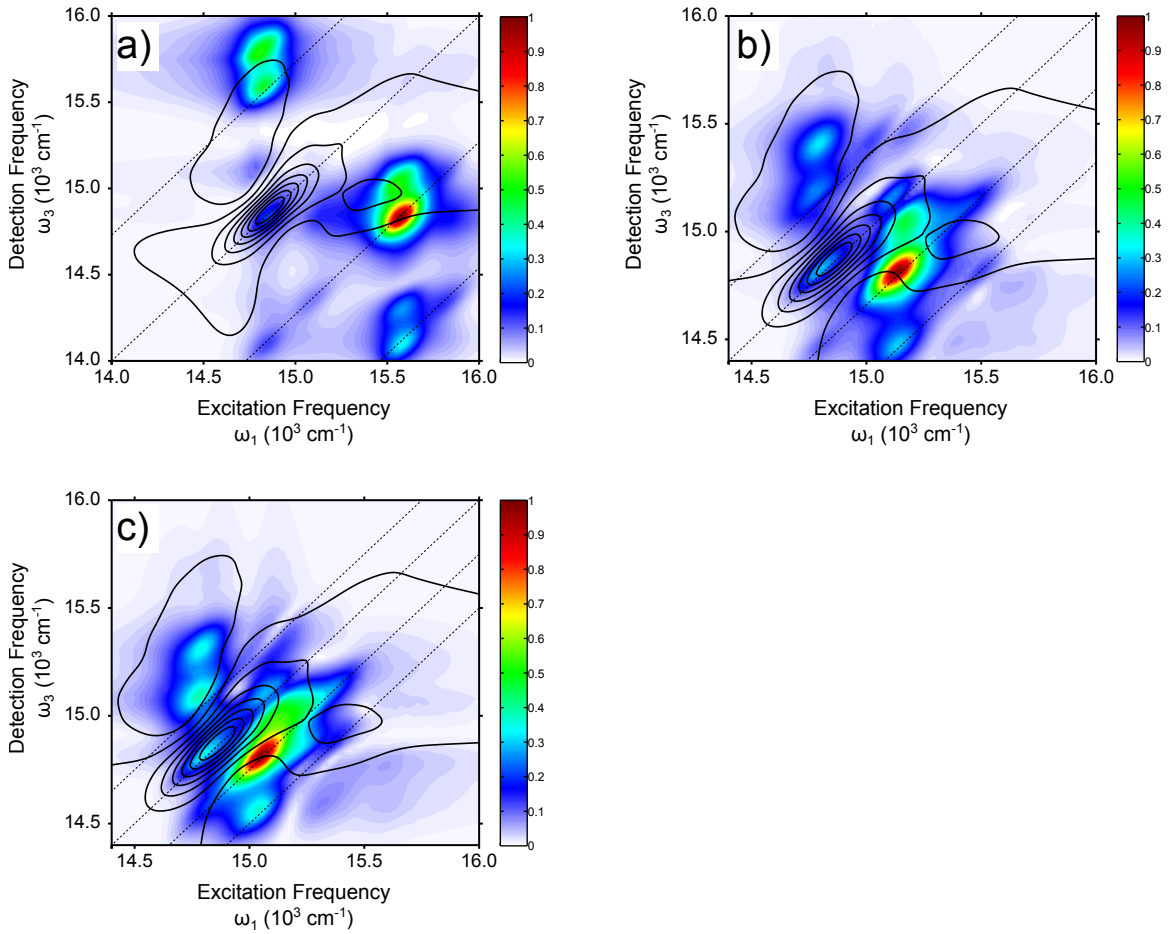

Figure 3.13: a) Simulated amplitude coherence maps for the special pair dimer model coupled to ~740 cm^{-1} vibrational mode at ω_2=~740 cm^{-1}. Simulated amplitude coherence maps for the special pair dimer model coupled to ~240 cm^{-1} and ~340 cm^{-1} vibrational modes at b) ω_2=~340 cm^{-1} and c) ω_2=~240 cm^{-1}. The dotted black lines presents the diagonal and parallel lines offset from the diagonal by $\pm\omega_2$ and $2\omega_2$. Black contours show the real rephasing 2D spectrum averaged over waiting time t_2.

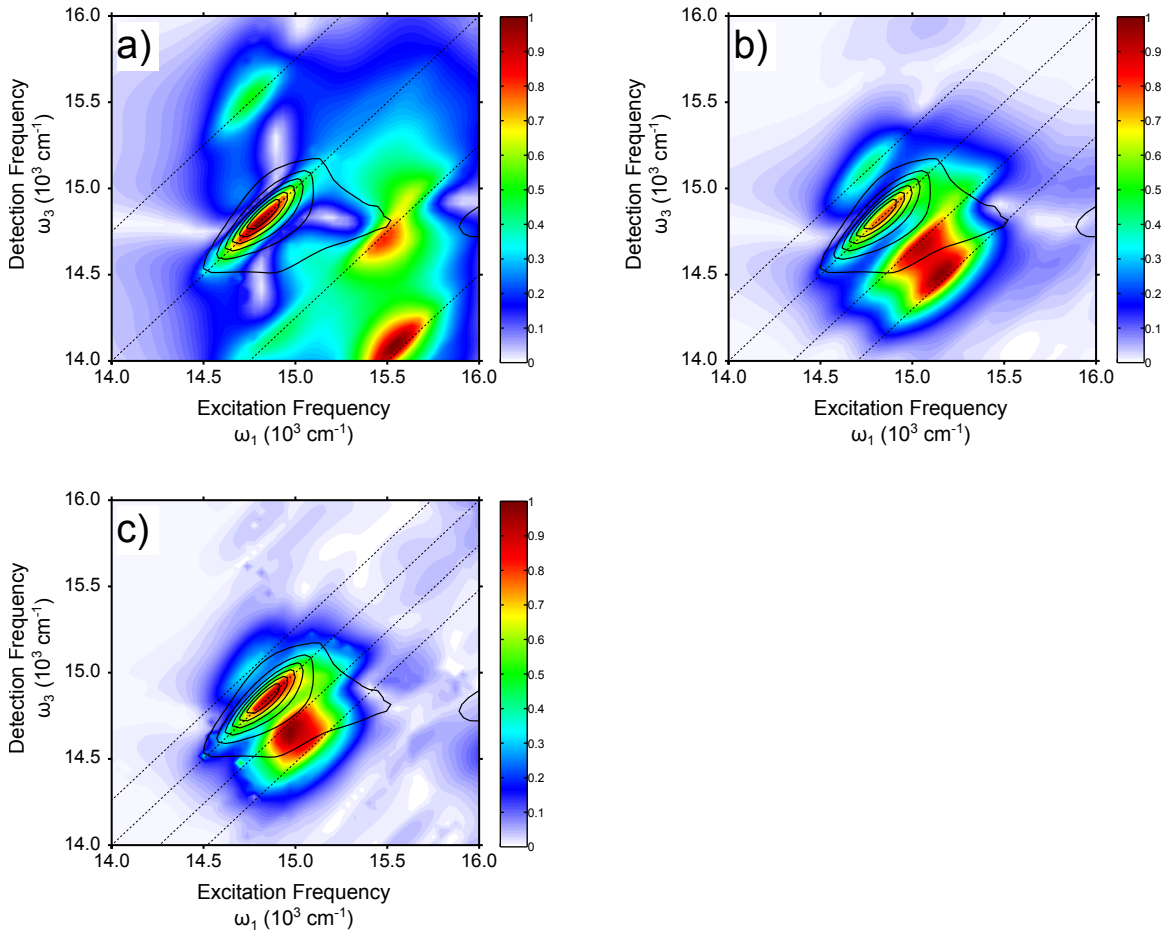

Figure 3.14: Simulated amplitude coherence maps for the Chl a coupled to vibrational modes at a) ω_2=~740 cm^{-1}, b) ω_2=~340 cm^{-1}, c) ω_2=~240 cm^{-1}. The dotted black lines presents the diagonal and parallel lines offset from the diagonal by $\pm\omega_2$ and $2\omega_2$. Black contours present the real rephasing 2D spectrum at t_2=0 fs.

3.8 Conclusion and Outlook

Herein, we investigated the differences and the similarities between the coherent dynamics occuring in the PSII RC and Chl a both experimentally and theoretically with a focus on three dominant modes: ω_2~740 cm^{-1}, ω_2~340 cm^{-1}, and ω_2~240 cm^{-1}. Our experimental results for these systems are in good agreement with those of theoretical simulations. We have observed that PSII RC has both vibrational (ω_2~740 cm^{-1}) and vibronic (ω_2~340 cm^{-1}, and ω_2~240 cm^{-1}) modes. The ω_2~740 cm^{-1} mode in Chl a exhibits vibrational characteristics, and low frequency modes exhibit deviations from the chair pattern even when they have excursively vibrational origin. The amplitude and phase coherence maps for low frequency modes are significantly different in the two systems.

Further experimental and theoretical studies should be performed to better understand the observed differences in the spectral signatures of coherence in Chl a and the PSII RC. Recent studies show that vibrational and electronic coherent dynamics have unique amplitude and phase characteristics which depend differently on the temperature [9]. One could utilize the temperature dependent 2DES to observe the variations in the amplitude and phase coherence maps as a function of temperature. Another approach is to analyze the coherent dynamics for different waiting time intervals (e.g. 100 fs$< t_2 <$500 fs, 500 fs$< t_2 <$1000 fs) as described in [18]. This analysis seeks a change in the character of the mode for different waiting time intervals. While understanding the origins of the coherent dynamics in the PSII RC and comparing them with those in Chl a informs us about the system, understanding the functional relevance of these dynamics is of a greater importance and remains a challenge. In this regard, numerical simulations have shown that ~240 cm^{-1} and ~340 cm^{-1} modes may play a significant role in the charge transfer in the PSII RC [1]. However, the experimental verification of this prediction remains to be shown. Investigating coherent dynamics in the anion bands of the PSII RC could potentially enable us to remove the ambiguity about the functional relevance of the coherent dynamics. In Chapter 5, I will present our studies on the anion band of the PSII RC (790 nm-820 nm).

References

[1] Franklin D. Fuller. *Observation of Coherences*. Thesis, (2014).

[2] Franklin D. Fuller, Jie Pan, Andrius Gelzinis, Vytautas Butkus, S. Seckin Senlik, Daniel E. Wilcox, Charles F. Yocum, Leonas Valkunas, Darius Abramavicius, and Jennifer P. Ogilvie. Vibronic coherence in oxygenic photosynthesis. *Nature Chemistry*, **6**:706–711, (2014).

[3] Vytautas Butkus, Donatas Zigmantas, Darius Abramavicius, and Leonas Valkunas. Distinctive character of electronic and vibrational coherences in disordered molecular aggregates. *Chemical Physics Letters*, **587**:93–98, (2013).

[4] Andrei V. Pisliakov, Tomas Mancal, and Graham R. Fleming. Two-dimensional optical three-pulse photon echo spectroscopy. ii. signatures of coherent electronic motion and exciton population transfer in dimer two-dimensional spectra. *The Journal of Chemical Physics*, **124**: 234505, (2006).

[5] Daniel B. Turner, Krystyna E. Wilk, Paul M. G. Curmi, and Gregory D. Scholes. Comparison of electronic and vibrational coherence measured by two-dimensional electronic spectroscopy. *Journal of Physical Chemistry Letters*, **2**:1904–1911, (2011).

[6] Vytautas Butkus, Donatas Zigmantas, Leonas Valkunas, and Darius Abramavicius. Vibrational vs. electronic coherences in 2d spectrum of molecular systems. *Chemical Physics Letters*, **545**:40–43, (2012).

[7] Gitt Panitchayangkoon, Dmitri V. Voronine, Darius Abramavicius, Justin R. Caram, Nicholas H. C. Lewis, Shaul Mukamel, and Gregory S. Engel. Direct evidence of quantum transport in photosynthetic light-harvesting complexes. *Proceedings of the National Academy of Sciences*, **108**:20908–20912, (2011).

[8] Vytautas Butkus, Leonas Valkunas, and Darius Abramavicius. Vibronic phenomena and exciton-vibrational interference in two-dimensional spectra of molecular aggregates. *Journal of Chemical Physics*, **140**, (2014).

[9] Vclav Perlik, Craig Lincoln, Frantisek Sanda, and Jurgen Hauer. Distinguishing electronic and vibronic coherence in 2d spectra by their temperature dependence. *The Journal of Physical Chemistry Letters*, **5**:404–407, (2014).

[10] M. G. Muller, M. Hucke, M. Reus, and A. R. Holzwarth. Annihilation processes in the isolated d1-d2-cyt-b559 reaction center complex of photosystem ii. an intensity-dependence study of femtosecond transient absorption,. *The Journal of Physical Chemistry*, **100**:9537–9544, (1996).

[11] Daniel Kaplan Marcel Bouvier Charles F. Yocum Roseanne J. Sension Brent Donovan, Larry A. Walker II. Structure and function in the isolated reaction center complex of photosystem ii. 1. ultrafast fluorescence measurements of psii. *The Journal of Physical Chemistry B*, **101**: 5232–5238, (1997).

[12] Vladimir I. Novoderezhkin, Jan P. Dekker, and Rienk van Grondelle. Mixing of exciton and charge-transfer states in photosystem ii reaction centers: Modeling of stark spectra with modified redfield theory. *Biophysical Journal*, **93**:1293–1311, (2007).

[13] Andrius Gelzinis, Leonas Valkunas, Franklin D. Fuller, Jennifer P. Ogilvie, Shaul Mukamel,

and Darius Abramavicius. Tight-binding model of the photosystem ii reaction center: application to two-dimensional electronic spectroscopy, (2013). URL http://www.escholarship.org/uc/item/15j4z89d.

[14] Erwin J. G. Peterman, Herbert van Amerongen, Rienk van Grondelle, and Jan P. Dekker. The nature of the excited state of the reaction center of photosystem ii of green plants: A high-resolution fluorescence spectroscopy study. *Proceedings of the National Academy of Sciences*, **95**:6128–6133, (1998).

[15] R. Picorel, M. Bakhtiari, T. Lu, T. M. Cotton, and M. Seibert. Surface-enhanced resonance raman-scattering spectroscopy as a surface-topography probe in plant photosynthetic membranes. *Photochemistry and Photobiology*, **56**:263–270, (1992).

[16] D. Abramavicius, L. Valkunas, and S. Mukamel. Transport and correlated fluctuations in the nonlinear optical response of excitons. *EPL (Europhysics Letters)*, **80**:17005, (2007).

[17] D. Abramavicius, V. Butkus, J. Bujokas, and L. Valkunas. Manipulation of two-dimensional spectra of excitonically coupled molecules by narrow-bandwidth laser pulses. *Chemical Physics*, **372**:22–32, (2010).

[18] Christoph Kreisbeck, Tobias Kramer, and Aln Aspuru-Guzik. Disentangling electronic and vibronic coherences in two-dimensional echo spectra. *The Journal of Physical Chemistry B*, **117**:9380–9385, (2013).

Chapter 4

Two-color Rapid Acquisition Coherence Spectroscopy

This chapter presents our work on developing a rapid and high signal-to-noise pulse-shaping based method for the characterization of coherent dynamics, distinguishing between ground and excited state coherences. First, I will discuss the typical problems with the current detection methods of coherence. Next, I will review the coherence concept and how nonlinear spectroscopy is used to study coherent dynamics. I will continue with the principles of the new method we have developed, discussing how it improves the signal to noise ratio in the experiment and reduces the overall data acquisition time. Additionally, I will discuss the information content of the new method and how it assists in distinguishing between ground and excited state coherence. Lastly, I will present technical details about the method and the experiment.

The original version of this chapter may be found at the following reference: S. Seckin Senlik, Veronica R. Policht, and Jennifer P. Ogilvie. **Two-Color Nonlinear Spectroscopy for the Rapid Acquisition of Coherent Dynamics**. *The Journal of Physical Chemistry Letters* **2015** 6 (13), 2413-2420. DOI: 10.1021/acs.jpclett.5b00861 [1].

4.1 Motivation and Background

Recording coherent dynamics with a high signal-to-noise ratio (S/N) is particularly challenging in photosynthetic samples; sample fragility and the risk of exciton-exciton annihilation at high

laser fluences limits the S/N and ultimately necessitates extended data acquisition times. These extended data acquisition times degrade the overall S/N due to slow fluctuations of laser amplitude and frequency content that can mask weak coherence signals and introduce errors in fitting the background population kinetics. The desire to obtain rapid, high S/N characterization of coherent dynamics motivates the development of alternative methods to full 2DES characterization. Several modified versions of 2D experiments have been proposed which effectively increase (S/N) by either reducing the data acquisition time and/or by selective excitation of coherence pathways with suppression of extraneous signals. Osborne et al. have developed a modified 2D infrared experiment where they select a particular inter-pump pulse delay t_1, reducing the dimensionality of the experiment to enable rapid and high S/N measurements of the frequency-frequency correlation function [2]. Two-color excitation has been used extensively to excite specific Raman coherences in coherent anti- Stokes Raman scattering (CARS) experiments, typically using off- resonant excitation [3, 4]. The Wright group has developed a frequency-domain approach of tuning excitation wavelengths to excite specific coherence pathways [5]. Lee et al. have performed a two-color photon echo experiment in which they excited a specific coherence and observed the dependence of the integrated echo signal on the two inter-pulse time delays [6, 7]. Womick et al. developed a two-color four-wave mixing experiment to excite electronic and nuclear coherences while suppressing population pathways [8]. The Davis group has used a similar approach [9–11], and has more recently used pulse-shaped excitation to excite specific coherence pathways in multidimensional experiments [12]. Wen et al. have also recently used pulse-shaping to enhance exciton and biexciton coherences [13].

Here we present Two-color Rapid Acquisition Coherence Spectroscopy (T- RACS), which utilizes an ultrafast pulse-shaper to shape the pump pulses spectra to selectively excite specific coherence pathways while simultaneously imposing a fixed inter-pump pulse time delay, t_1. Fixing t_1, reduces the dimensionality of the experiment, drastically shortening the time required to record coherent dynamics of interest. To demonstrate T-RACSs ability to tease out coherent dynamics, we present data acquired via T-RACS alongside broadband and two-color 2DES data from chloro-

phyll a (Chl a). Chl a is the most abundant chromophore in plant photosynthetic complexes and serves as a good test system for studying and understanding the coherences observed in larger photosynthetic antennae and reaction centers.

4.2 Probing Coherence with Nonlinear Spectroscopy

Coherences are generated when a light-matter interaction creates a coherent superposition of two states; the system evolves in this coherent state, oscillating at the difference in frequency between the two superposition states. In nonlinear spectroscopies, such coherences are generated and probed by sequences of laser pulses, and the response of the system to these sequences is typically understood using perturbation theory [3]. In this perturbative approach any given nonlinear spectroscopy is analyzed in terms of the possible interactions between the system and the dipole operator, taking into consideration the energy level structure of the system and the details of the spectroscopic measurement. In pump-probe spectroscopy, a pump pulse interacts with the system twice to create populations and coherences which evolve until a third light-matter interaction with the probe pulse some waiting time later. 2DES uses a series of three light pulses: two pump pulses separated by variable time delay, t_1 followed by a probe some waiting time, t_2, later (Figure 4.1a). In 2DES each pump pulse contributes a single interaction to create populations and coherences that evolve during t_2. 2DES signal is typically recorded as a function of the delays t_1 and t_2, while the t_3 dependence is often detected directly in the frequency domain to yield ω_3. Fourier transforming the 2DES data with respect to t_1 produces a two-dimensional (ω_1,ω_3) spectrum for a given t_2. Information about how individual transitions behave is mapped along the diagonal (ω_1=ω_3) whereas off-diagonal cross peaks describe couplings and coherences in the system [14–17]. By looking at the two- dimensional (ω_1,ω_3) distribution of the coherence amplitude we can gain considerable insight into the physical origin and dynamics of the system. This can be achieved by Fourier-transforming with respect to t_2 (essentially performing 3DES) to create a 3D frequency solid that can be "sliced" to observe the 2D distribution of particular ω_2 modes of

interest in what are called coherence or Fourier maps (Figure 4.2c) [18–20]. These Fourier maps have been presented as metrics for determining the physical origin of coherences in 3DES signals in a large body of theoretical work; there are several simplified model systems proposed to assign electronic, vibrational, and vibronic coherence origin [20–22, 22–26]. Here we focus on the displaced oscillator model [23, 25] for vibrational coherences to explain observed coherent dynamics in Chl a. Comparing the Fourier maps for the displaced oscillator with experimental data enables the assignment of vibrational origin and distinction between ground and excited state vibrational coherence. This distinction has been achieved previously in pump-probe spectroscopy using phase arguments [27, 28] while in 2DES comparisons of rephasing and nonrephasing amplitudes and phases, as well as Fourier map distributions, have been used [22, 24, 25, 29–32].

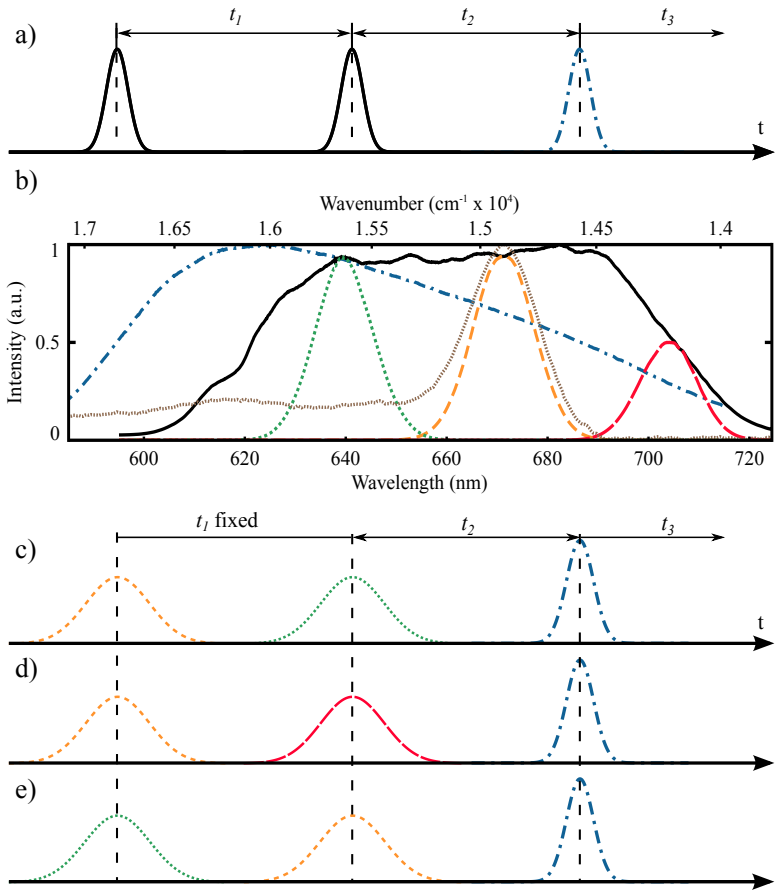

Figure 4.1: Pulse-ordering diagrams for two- dimensional electronic spectroscopy (2DES) and two-color rapid acquisition coherence spectroscopy (T-RACS). (a) Broadband 2DES pulse sequence uses two identical broadband pump pulses (black) followed by a third broadband probe pulse (blue, dot-dash). (b) Absorption spectrum of Chl a in an isopropyl alcohol/glycerol mixture at 77 K (brown, short-dash); peak absorption of the Q_y band is at 14925 cm^{-1} (670 nm). Laser spectra used in broadband 2DES experiments: pump (black, solid) and probe (blue, dot- dashed) spectra; for T-RACS experiments different pairs of the three Gaussian spectra were used as pumps (orange, dash; red, long-dash; green, dotted), followed by a broadband probe (blue, dot-dashed). c)- e) T-RACS pulse sequences employing the respective pump spectra shown in (b) T-RACS sequence c) selectively probes excited-state vibrational coherences, while d) selectively probes ground-state vibrational coherences and e) probes a mixture of ground and excited state coherence pathways [1].

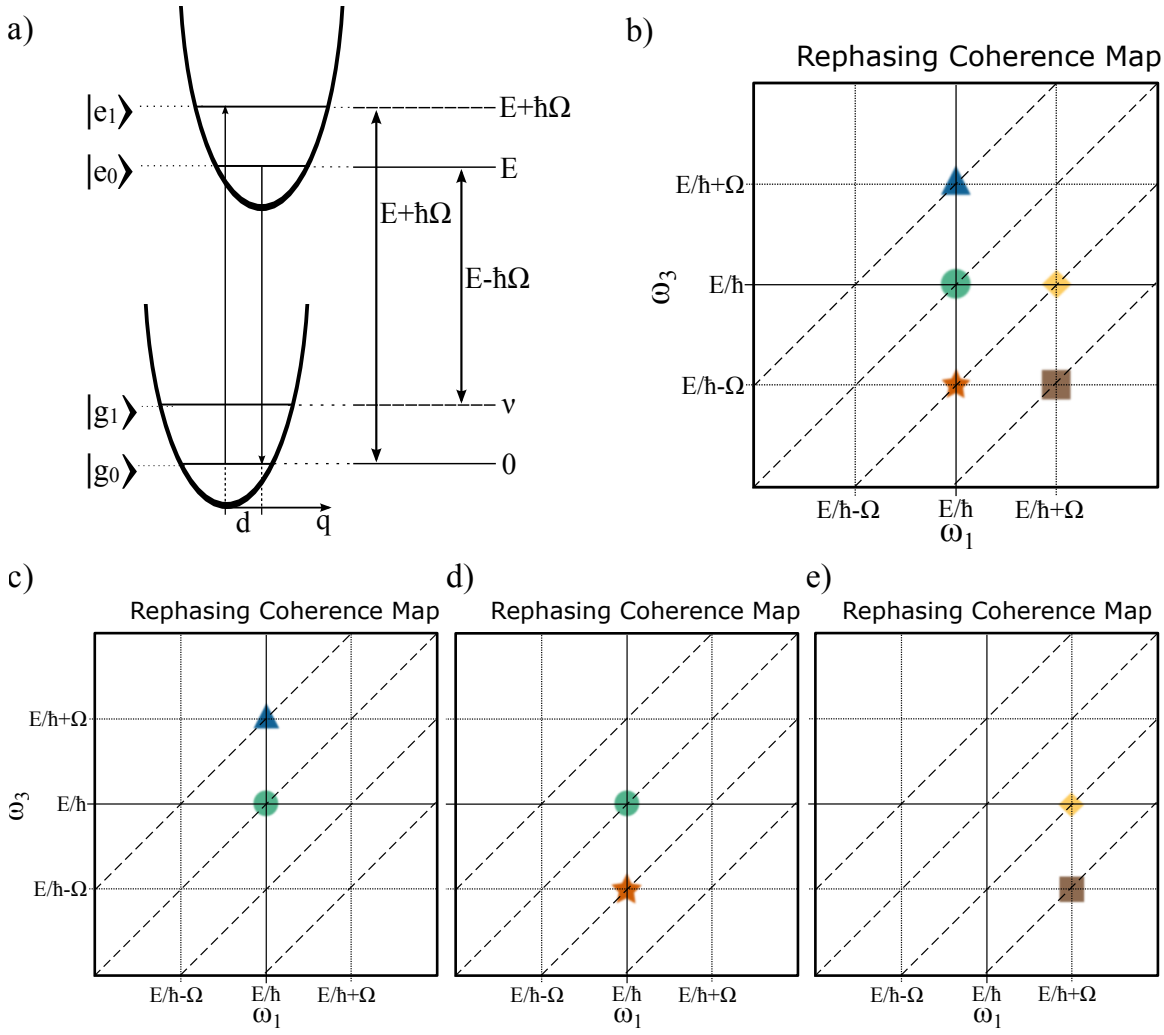

Figure 4.2: a) Displaced oscillator model featuring electronic transition energy E and vibrational level transition frequency Ω. (b) Cartoon rephasing Fourier map for the displaced oscillator model at ω_2=Ω, displaying the characteristic "chair" pattern of the displaced oscillator model. The corresponding Feynman diagrams are detailed in Section 4.8. Of particular interest are signals located at the blue triangle and orange star that correspond to excited and ground state vibrational coherences respectively. All other signatures correspond to a mixture of ground and excited electronic state pathways. (c)-(d) Cartoon rephasing Fourier maps for the respective two-color pulse sequences shown in Figure 4.1(c)-(d). Each two-color experiment selects a subset of the coherent signals detected in the rephasing Fourier map from a broadband 3DES experiment (shown in Figure 4.2b). Signals in c) are exclusively excited-state vibrational coherences, while d) selectively probes ground-state vibrational coherences and e) probes a mixture of excited and ground state contributions as discussed in Figure 4.6 [1].

4.3 Principles of T-RACS

We seek a method that selectively excites particular coherence pathways and enables rapid characterization of the coherences with a high S/N while retaining much of the information content of a full 3DES measurement. To achieve this goal we adopt a two-color excitation scheme where the two pump pulses have no spectral overlap and possess the appropriate frequency difference to excite the coherence of interest. The probe pulse remains unshaped and broadband. We fix the t_1 delay to ensure the desired pulse- ordering (avoiding substantial pulse overlap), and we record the coherence signal as a function of t_2 and ω_3. The pulse sequences for different T-RACS experiments are shown in Figure 4.1c-e. We note that our approach is similar to that of Womick et al., who performed two-color four-wave mixing experiments with a fixed t_1=0 [8]. Here we separate the rephasing and nonrephasing signals and use different color orders to selectively excite particular coherences and probe their physical and ground/excited state origin.

To understand how T-RACS excites and records coherent dynamics, and to compare the information it provides with what is obtained by 3DES, we consider a displaced oscillator system with a single vibrational level of frequency Ω on the ground and excited electronic states separated by energy E (Figure 4.2a). Turner et al. have detailed the double-sided Feynman diagrams that illustrate how intraband coherence on the ground or excited electronic state of the displaced oscillator can be generated by a 2DES rephasing pulse sequence [25]. Within the displaced oscillator model, the rephasing Fourier map has a characteristic "chair" shape [22] and excited and ground state coherences can be clearly separated as shown in Figure 4.2b with a triangle and star respectively. T-RACS experiments can be designed to excite a subset of the "chair" signals of the displaced oscillator system. As long as the bandwidth of the individual pump pulses is less than Ω the choice of pump pulse spectra and their relative ordering determine which set of coherence pathways will be excited. Figure 4.2c-e shows the subset of specific coherence pathways for a displaced oscillator that are excited by different rephasing T-RACS experiments (respective pulse-sequences shown in Figure 4.1c-e). The corresponding double-sided Feynman diagrams are detailed in Section 4.8, along with the nonrephasing signals. For a given T-RACS pulse sequence, the first pump pulse

creates a coherence between ground and excited states that must oscillate at a frequency contained within its bandwidth (neglecting coherence transfer events). Thus the bandwidth of the first pulse effectively windows the coherence signals along the ω_1 axis. The bandwidth and central frequency of the second pump pulse determines which intraband coherences will be excited and evolve at ω_2. Since T-RACS resolves ω_3, and rephasing and nonrephasing signals can be readily separated, T-RACS can readily resolve the different coherent signals present in a 3DES-derived Fourier map as depicted in Figure 4.2c-e. Thus it can be used to assign the physical origin of the observed coherence. In the case of vibrational coherence, it also enables identification of ground and excited state contributions and their respective frequencies.

4.4 Observations of Coherence in Chlorophyll a by 3DES and T-RACS

To demonstrate the ability to selectively excite and study particular coherences with T-RACS we perform studies of Chl a in isopropanol/glycerol solution. These studies also enable a comparison of the relative speed, information content and signal-to-noise ratio (S/N) of the 3DES and T-RACS methods. The pulse spectra for both the 3DES and T-RACS experiments are shown in Figure 4.1b. The pump-pulse spectra for the T-RACS experiments have been chosen to selectively excite coherence at ω_2=~740 cm^{-1} to match a vibrational mode reported in resonance Raman [33], [34], [35], [36] fluorescence line-narrowing [34] and pump-probe [37] experiments and also observed in our recent study of the photosystem II reaction center [19]. The t_2 dependent signals for broadband 3DES and T-RACS (for pulse sequence in Figure 4.1e) are shown in Figures 4.3a and c respectively for t_1=0 fs. The rephasing (red, solid) and nonrephasing (blue, dashed) 3DES signal (Figure 4.3a) are dominated by population dynamics that must be fit and subtracted out in order to analyze the overlaid coherent oscillations which appear as a weakly periodic amplitude modulation. The Frobenius spectrum (taken by summing the square of the signal amplitude over dimensions ω_1 and ω_3 and then taking the square root) of the rephasing signal from the broadband 2DES ex-

periment (Figure 4.3b) features many coherences. Several of these (ω_2=265, 348, and 747 cm^{-1}) are prominent above the noise floor. In contrast to the broadband 3DES experiment, the T-RACS trace in Figure 4.3c is dominated by a single frequency oscillation with no obvious exponential dependence, indicating that the two-color pump pulse sequence selects the desired coherence and suppresses contributions from population pathways. The Frobenius spectrum in Figure 4.3d features one large amplitude peak near ω_2=742 cm^{-1}; all the other modes present in the broadband 3DES case have been effectively suppressed. Here we show the rephasing and nonrephasing signals for t_1=0 fs in order to highlight the population dynamics during t_2 present in the 3DES data. T-RACS experiments with $t_1 > =0$ have lower S/N as shown in Figure 4.7, but have well-defined pulse-ordering when t_1 is greater than the pump pulse duration, enabling cleaner separation of coherent pathways.

4.5 Speed, Signal-to-noise Ratio and Selectivity

The coherences extracted from the broadband 3DES experiments shown in Figure 4.3b required 110 minutes of data acquisition time. In contrast, the T-RACS experiments, scanned over the same number of t_2 points with the same averaging required only 7 minutes, more than 15 times shorter. We note that the use of a pulse- shaper, which enables data acquisition in the rotating-frame [38, 39], significantly reduces the number of t_1 points required to resolve the ω_1 frequency axis. Without this sampling reduction, 2DES experiments that do not acquire data in the rotating frame typically record several hundred t_1 points [40, 41]. In this case T-RACS offers approximately two orders of magnitude faster acquisition of coherent dynamics than 3DES. We also note that the rapid acquisition enabled by T-RACS makes scanning longer t_2 delays straightforward should increased spectral resolution of the coherence frequency be desired. The rephasing (nonrephasing) Frobenius spectrum (Figure 4.3d) of the T-RACS experiment boasts a S/N that is 32 (29) times higher than that acquired by 3DES (Figure 4.3b). The increase of S/N of the T-RACS method over 3DES can be attributed to the substantial reduction in data acquisition time that reduces laser

power and spectral fluctuations. As expected the two-color excitation of T-RACS imparts spectral selectivity compared to the broadband 2DES technique. This is demonstrated by the ratio of the selected coherence to the next largest peak amplitude in the Frobenius spectrum (Figure 4.3d). The amplitude of the 742 cm^{-1} (738 cm^{-1}) peak in the rephasing (nonrephasing) signal is 21 (23) times larger than the next largest peak in the T-RACS experiments, whereas the same ratio for the largest peak within $640 \leqslant \omega_2 \leqslant 840$ cm^{-1} in the rephasing (nonrephasing) broadband 2DES technique is only 3 (2.5). We note that in the present example the ~740 cm^{-1} coherence is relatively isolated from other modes; the case of selectively exciting one out of several coherences within a few tens of wavenumbers of one another has not been tested here.

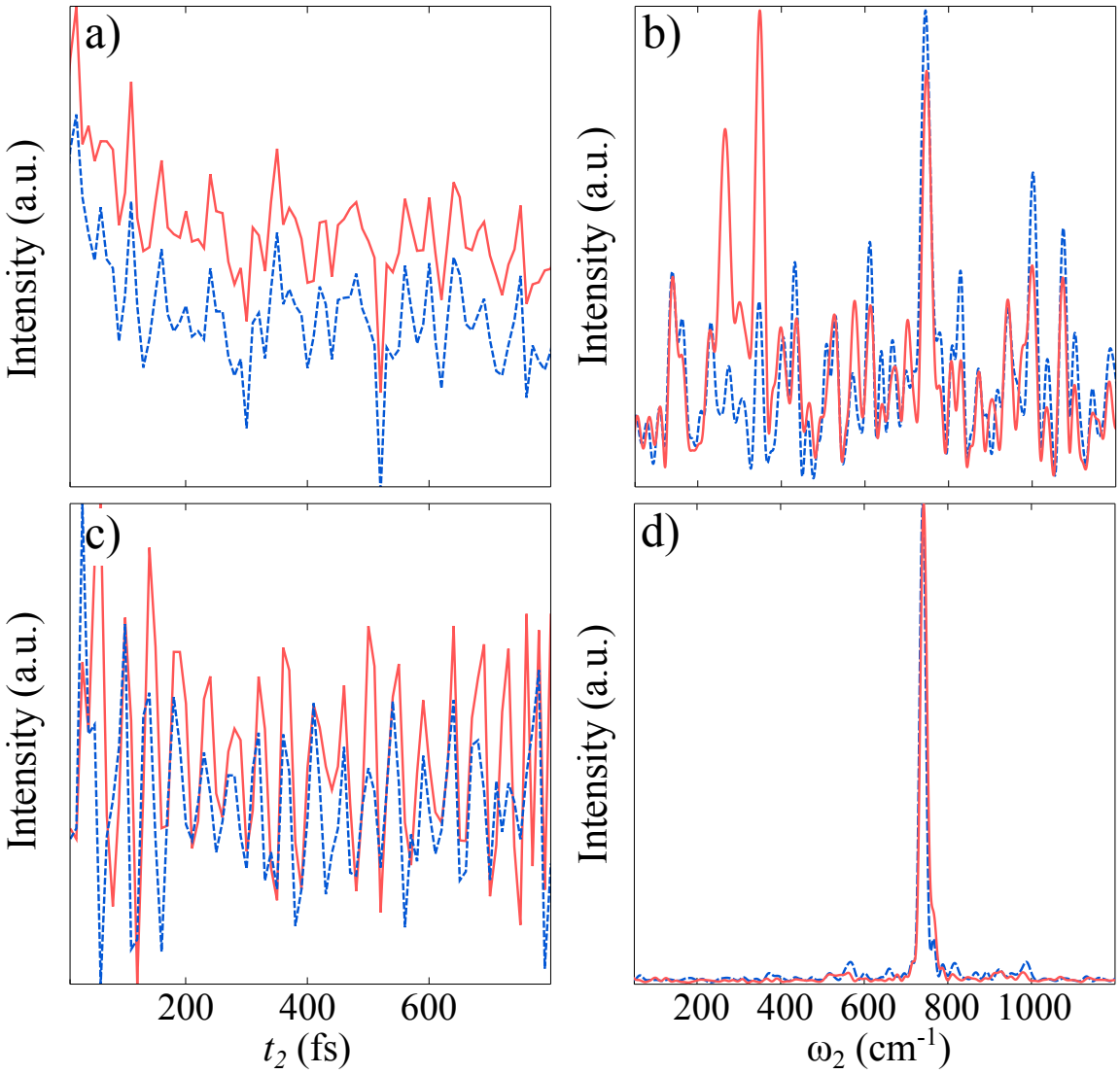

Figure 4.3: Waiting time t_2 traces for the real part of rephasing (red) and nonrephasing (blue, dashed) signals and their corresponding Frobenius spectra for the broadband 3DES (a,b) and a T-RACS (c,d) experiment which used the pulse sequence in Figure 4.1e. All the waiting time traces are taken with t_1=0 fs to highlight the increased contrast of the oscillations when population kinetics are suppressed by using two-color excitation [1].

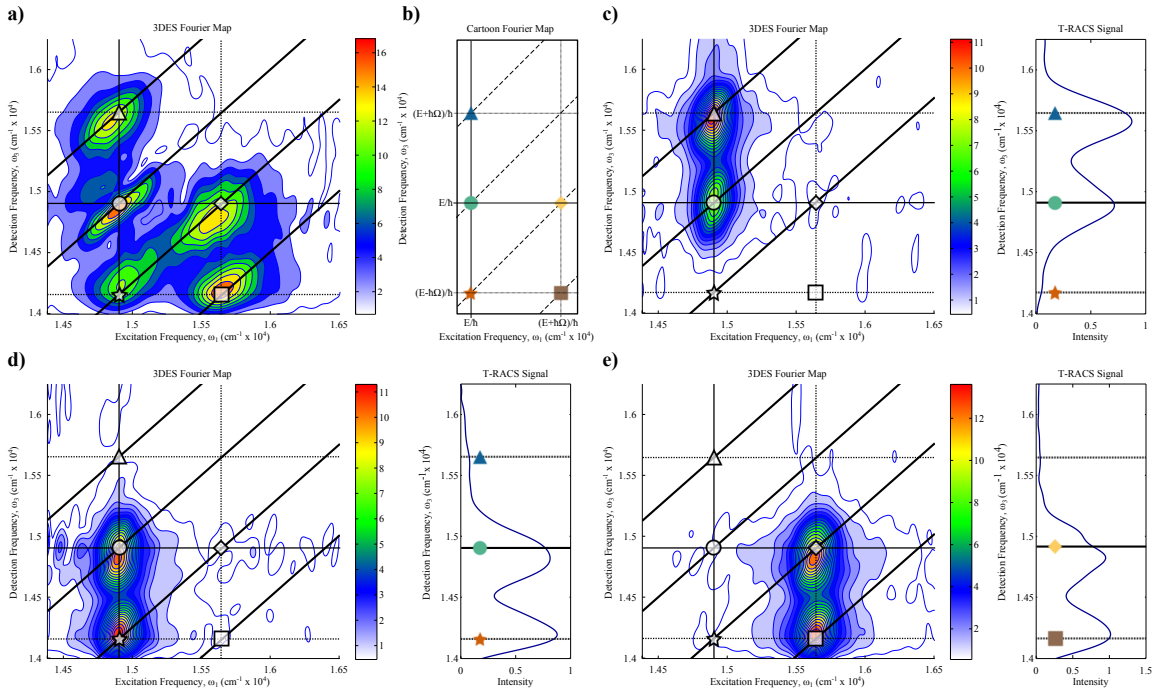

Figure 4.4: Rephasing Fourier map for ω_2=747 cm^{-1}, derived from the broadband 3DES data, showing the characteristic chair pattern for a displaced oscillator. b) Expected signals contributing to the rephasing Fourier map within the displaced oscillator model. Of particular interest are the excited state (blue triangle) and ground state (orange star) coherence signals. Corresponding double-sided Feynman diagrams are given in Section 4.8 (Figure 4.6). c)-e) Rephasing Fourier maps from two-color 3DES and corresponding T-RACS signals for the respective pulse sequences shown in Figure 4.1c)-e). Dotted lines indicate ω_1 ,ω_3=$E/\hbar - \Omega$ and $E/\hbar + \Omega$, solid lines indicate ω_1,ω_3=$E/\hbar$; in ω_3, these lines indicate the position of the blue triangle and orange star that (within the displaced oscillator model) correspond to excited state and ground state coherence, respectively. Dotted lines indicate the ω_3 position of the blue triangle and orange star that (within the displaced oscillator model) indicate excited state and ground state coherence respectively. The coherence frequency (ω_2) for two-color 3DES (T-RACS) for pulse- sequences c)-e) were determined to be: c) 736 cm^{-1} (740 cm^{-1}), d) 748 cm^{-1} (746 cm^{-1}), e) 742 cm^{-1} (742 cm^{-1}). Contours are plotted in increments of 10% (a) and 5% for c-e, starting from 4% of the maximum intensity [1].

4.6 Information Content of T-RACS

To investigate the ability of the T-RACS method to selectively probe specific coherences and to discern their physical origin we present Chl a data from broadband 3DES, spectrally-shaped two-color 3DES, and T-RACS measurements in Figure 4.4a shows the Fourier map for ω_2=747 cm^{-1} derived from the rephasing broadband 3DES data. This Fourier map displays the characteristic chair pattern expected for a displaced oscillator. In Figure 4.4c-e we show Fourier maps and T-RACS data for the corresponding pulse sequences shown in Figure 4.1c-e. The Fourier maps require scanning t_1 (as in standard 2DES and 3DES measurements), while the T-RACS data was recorded for set t_1=60 fs. The Fourier maps resemble the expected maps for a displaced oscillator shown in Figure 4.2c-e, demonstrating that the use of two-color excitation and color order selects the expected subset of the coherence signals produced by broadband excitation. Fourier maps derived from broadband 3DES data reveal the overall distribution of coherence amplitude as a function of (ω_1,ω_3), which is particularly useful for initial coherence studies in systems where little is known about the physical origin of the coherences and/or the frequencies to be expected. In contrast, Fourier maps generated from the pulse-shaped two-color 3DES feature a subset of the signals within the broadband 3DES Fourier map, where the spectral amplitude of the first pump pulse essentially applies a filter to the ω_1 axis of the broadband 3DES Fourier map. The frequency of the second pulse and the choice of phase-matching (rephasing or nonrephasing) selects the subset of coherence signals to be resolved along ω_3.

Although T-RACS does not resolve the ω_1 axis, it is clear from Figures 4.4c-e that the T-RACS data contains similar information to the Fourier maps recorded with the pulse-shaped two-color pump spectra. By resolving the ω_3 axis, the T-RACS data shows the same distinct signals separated by Ω; there is little additional information to be gained by resolving ω_1 when relatively narrowband two-color excitation is used. The reduced acquisition time and higher S/N compared to 3DES make T-RACS an attractive alternative that retains the information content that can be used to assign the physical origin of the coherence (for example, ground or excited state vibrational coherence). Chl a has been well studied by resonance Raman [33, 34], fluorescence line narrowing (FLN) [34–

36], hole-burning [42], and pump-probe [37] spectroscopies. While here we have focused on the ~740 cm^{-1} mode to demonstrate the T- RACS approach, we have observed other modes as well and will discuss their physical origin in a subsequent publication. The rephasing Fourier maps for the ~740 cm^{-1} mode (shown in Figure 4.4a, 4.4c, and 4.4d as derived from broadband and two- color 3DES) exhibit signal at both the "triangle" and the "star" position, indicating excited and ground state contributions in agreement with Du et al.52. The same conclusion can be drawn from the T-RACS data in Figure 4.4c, 4.4d. Comparing the frequencies obtained in the rephasing T-RACS data and Fourier maps for the excited-state coherence pulse sequence (Figure 4.2c) with those of the ground-state coherence pulse sequence (Figure 4.2d) we find a consistent red shift of the excited state coherence frequency with respect to the ground state value.

4.7 Comparing Ground and Excited State Dephasing

To resolve differences in ground and excited state coherence frequencies and compare their relative dephasing times we performed higher resolution T-RACS scans. The improved S/N and speed of T- RACS enables high frequency resolution measurements since long t_2 scans can be readily made. The excited and ground state signals were recorded using the pulse sequences shown in Figure 4.1c and d respectively, at t_1=60 fs. Representative rephasing time domain data showing the excited and ground state coherences are plotted in Figure 4.5a, 4.5b respectively, at ω_3 values that were selected for their high S/N. Figure 4.5c shows the corresponding Frobenius spectra for the excited and ground state coherences. The higher resolution of the 5 ps scan reveals an additional small amplitude vibrational mode to the blue side of the main peak in both the excited and ground state data. For the excited state data we find frequencies of 738$\pm$3 cm^{-1} and 748$\pm$3 cm^{-1} for the dominant and smaller modes respectively, which compare well with the reported frequencies of 740$\pm$4 cm^{-1} and 750$\pm$4 cm^{-1} from FLN experiments [35]. On the ground state we find frequencies of 743$\pm$3 cm^{-1} and 754$\pm$3 cm^{-1}, which also compare well with the reported frequencies of 744$\pm$2 cm^{-1} and 750$\pm$2 cm^{-1} from the same FLN experiments [35]. Assuming Lorentzian lineshapes,

the excited and ground state dominant modes have similar dephasing times of 1420±200 fs and 1490±200 fs respectively. For the T-RACs experiment that reports mixed ground and excited state coherence (Figure 4.2e) we find an intermediate value of 742±4 cm^{-1} in the rephasing T-RACS data, consistent with our expectations for a mixture of ground and excited state. These frequencies were also consistent with the results obtained by two-color 3DES as reported in Figure 4.4c-d and with the nonrephasing T-RACS data presented in Figure 4.8. We note that while the use of the displaced oscillator model works well for the ~740 cm^{-1} mode, there are aspects of the data that cannot be well accounted for by this simple model. These aspects are discussed in Section 4.8 (Figures 4.9-4.10).

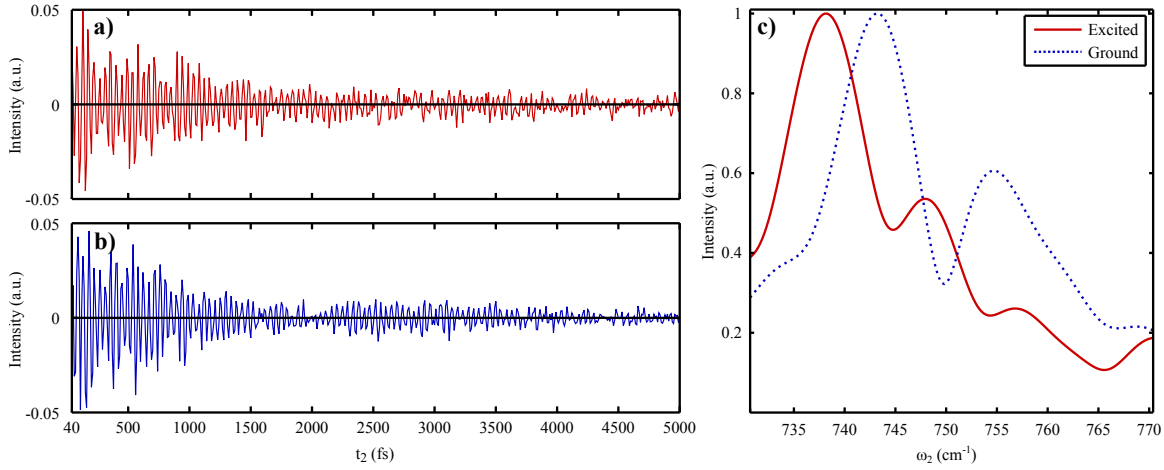

Figure 4.5: a) T-RACS rephasing signal at t_1=60 fs, ω_3=15673 cm^{-1} for the excited state pulse sequence of Figure 4.1c. b) T-RACS rephasing signal at t_1=60 fs, ω_3=14285 cm^{-1} for the ground state pulse sequence of Figure 4.1d. c): The Frobenius spectra of the excited state (red solid) and ground state (blue dashed) T-RACS data [1].

In conclusion we have demonstrated a rapid and high S/N pulse-shaping-based approach for recording coherent dynamics. Compared to recording coherences using broadband 3DES, T-RACS offers enhanced S/N and a significant reduction in data acquisition time: 15-fold compared to 3DES methods that operate in the rotating-frame, and ~two-orders of magnitude compared to standard 3DES methods. This method is most easily implemented with a pulse-shaper, though we note that this approach could also be applied with other methods of spectral amplitude control. Although T-RACS is a reduced dimensionality experiment, through the appropriate choice of pulse-sequence and resolution of the ω_3 dependence of the signal, it retains much of the information about the physical origin of the coherence that is available from 3DES measurements, such as the ability to distinguish excited-state and ground-state coherence.It can also be used to determine the excited and ground state coherence frequencies with high spectral resolution and high S/N, and has the benefit over FLN of enabling measurements over a broad temperature rang. In systems where coherent dynamics have not previously been studied, a combination of 3DES and T-RACS may be most effective. Broadband 3DES serves well to survey the Frobenius spectrum of all coherent modes, while T-RACS could be used to perform rapid, higher S/N studies of selected coherent dynamics of interest. We have used both 2DES and T-RACS to demonstrate that Chl a exhibits clear coherent dynamics. Using T-RACS we have studied the ~740 cm^{-1} mode in detail, showing that T-RACS can separate ground and excited state coherences and determine their frequencies and dephasing times. We note that our observations of strong coherent dynamics in Chl a are in contrast to recent reports of only weak coherent signatures in 2DES studies of bacteriochlorophyll a. The ease with which coherent dynamics can be characterized by T-RACS should make it a valuable tool to address current open questions about the role of coherence and electronic-vibrational coupling in energy transfer and charge separation in natural and artificial light-harvesting materials.

4.8 Appendix

4.8.1 Sample Properties

All experiments performed here used a hybrid pulse-shaping/diffractive optics method discussed in Chapter 2. The pump and probe spectra for both the broadband 3DES and T-RACS experiments are shown in Figure 4.1b and are produced by two home-built NOPAs. We used Chl a samples derived from Anacystis nidulans algae purchased from Sigma Aldrich. Our sample was prepared in a solvent of isopropanol and glycerol at a 1:1 ratio. We measured a sample optical density OD=0.23 in a 380μm thick custom sample cell, loaded into a cryostat and held at 77 K .

4.8.2 Experimental Methods

The laser sources used in the experiments were derived from a Ti:Sapphire oscillator (MaiTai SP) seeding a regenerative amplifier to produce 40 fs pulses centered at 800 nm (Spectra Physics Spitfire Pro) running at 500 Hz. The 800 nm light is fed into two noncollinear optical parametric amplifiers (NOPA) [43], which individually produce tunable, broadband light for our pump and probe beams. For all experiments described here, the pump and probe NOPAs were tuned to a central wavelength of 660 nm and 650 nm, respectively, with the spectra shown in Figure 4.1b. The pump NOPA light was partially compressed using a home-built grism (grating prism compressor)[44] before being fully compressed by an acousto-optic pulse shaper (Dazzler, Fastlite). The Dazzler was also used for phase-cycling, to control all t_1 delays, and to spectrally shape the pump pulses used in the two-color experiments. The broadband probe NOPA light was compressed using another home built grism. The t_2 delay was generated using a conventional retro-reflecting stage.

4.8.3 Data Analysis:Broadband Two-dimensional Electronic Spectroscopy

The broadband 2DES experiments performed here used pump and probe spectra shown in Figure 4.1b. After compression the pump and probe were 12 and 15 fs long. The inter-pump pulse

delay was scanned through 0⩽ t_1 ⩽390 fs in 10 fs steps while scanning the waiting time, -200⩽ t_2 ⩽2000 fs. We restricted the coherence analysis to 40⩽ t_2 ⩽2000 fs to avoid coherent artifacts at $t_2 = 0$ fs. We used a six-phase-cycling scheme to isolate rephasing and nonrephasing signals and to suppress various interference scatter terms for each t_1 delay, including the probe scatter terms [45]. A mechanical chopper placed in the probe NOPA beam enables pump scatter subtraction and reduces the duty cycle to 90%. Each 2D spectrum is collected by averaging for 750 milliseconds per t_1 delay which, for 40 t_1 values, is 30 seconds of averaging per 2D spectrum. The 2D spectra were phased using the projection-slice theorem [16] as described previous chapter. The same phasing parameters were used for the T-RACS experiment. To extract the coherent dynamics from the 2DES data we fit the dominant population dynamics with a biexponential fit which we subtracted from the overall signal to isolate the weak oscillatory coherence signals. The remaining signal is Fourier transformed with respect to t_2, representing the 2DES data as a three-dimensional frequency solid. A way of quantifying the frequency content during the waiting time (t_2) dynamics is to take the Frobenius Norm of the 3D frequency solid, summing over the absolute magnitude, squared, of each 2D point (ω_1,ω_3) and then taking the square root.

$$A_{Frobenius}(\omega_2) = \sqrt{\sum_{i=1}\sum_{j=1}(\mid S(\omega_{1,i}, \omega_2, \omega_{3,j}))\mid^2} \tag{4.1}$$

No fitting algorithm was necessary for processing two-color 2DES and T-RACS data as there are no population kinetics. The Frobenius spectra for two-color 2DES and T-RACS experiments were obtained following Fourier transformation of the signal with respect to t_2.

4.8.4 Data Analysis:T-RACS

To selectively excite specific coherences we use spectrally-shaped pump pulses. The pulse-shaper produces pump pulses with one of two truncated narrow-band portions of the broadband input pulse (Figure 4.1b). The choice of pump pulse spectra shown in Figure 4.1b is informed by the spectral distribution of coherences centered at ω_1=$E/\hbar$ and ω_1=$E/\hbar + \Omega$ in Figure 4.2b where E

corresponds to the main electronic transition being probed and is the frequency of the vibrational mode being probed. We choose two pump spectra that include $E/\hbar$ and $E/\hbar+\Omega$, respectively, but which are narrow bandwidth enough to avoid spectral overlap. The shaped pump pulses (Figure 4.1b) used in the experiments in Figures 4.3 and 4.4 have 11-12 nm of bandwidth (a duration of ~60 fs) with a central frequency dependent on the coherence being probed. The shaped pulse spectra shown in Figure 4.1b were used to selectively excite coherences oscillating at ω_2=740 cm^{-1}. For each T-RACS study of a given coherence, three experiments are performed with alternate pump pulse ordering (see Figure 4.1c-e) to select different coherence pathways. Here we have chosen t_1=60 fs to avoid pump pulse overlap while maintaining a large signal (signal amplitude decreases with larger pump-pulse separation as shown in Figure 4.7). By choosing t_1=60 fs, we ensure that we are looking at a single subset of possible pathways from Figure 4.2b; even though we are able to separate the rephasing and nonrephasing signals, at t_1=0 fs we are exciting and recording signals from multiple subsets of Figure 4.2b. The same phase-cycling scheme and averaging time as was used for the 2DES measurement was applied to the T-RACS data to enable a fair comparison of the S/N of the two approaches. No fitting algorithm was necessary for processing T-RACS data as there are no population kinetics. The Frobenius spectra for T-RACS experiments were obtained following Fourier transformation of the signal with respect to t_2.

4.8.5 Double-sided Feynman Diagrams Contributing to T-RACS Signals in the Displaced Oscillator Model

Figure 4.6 details the light-matter pathways contributing to coherence signals for a simple displaced oscillator (Figure 4.2a) [25], representing each pathway with Double-sided Feynman Diagrams (DSFD). The pathways are subdivided by the particular pulse sequence used (see corresponding spectra for pulses in Figure 4.1b) and roughly correspond to pathways featuring vibrational coherences on the excited state (a), ground state (b), and a mixture of excited and ground states (c) for the rephasing and nonrephasing signals (Note that the pulse sequences considered in Figure 4.6a, 4.6b, 4.6c correspond to those in Figure 4.1c, 4.1d, and 4.1e respectively). Car-

toon Fourier maps represent the 2D (ω_1,ω_3) distribution of the possible pathways described by the DSFDs. A more thorough way to talk about how the signals are enumerated in Figure 4.6 is in terms of energy levels and which transitions are involved. We assume that our system is initially in the ground electronic and vibrational state; at 77 K, k_bT=6.4x10^{-3} eV corresponding to ~51 cm^{-1}, much less than the vibrational frequency we are probing. Given this assumption, we can excite a coherence between the ground state and one of two transitions: the electronic transition, $|\ g_0\rangle \rightarrow |\ e_0\rangle$, or the Franck-Condon allowed $|\ g_0\rangle \rightarrow |\ e_1\rangle$. Either possibility can be selected by our choice of first pump pulses centered at $E/\hbar$ or $E/\hbar + \Omega$ respectively. We note that for lower frequency modes than the ~740 cm^{-1} mode we consider here, inhomogeneous broadening may prohibit this selective excitation. We are interested in pathways that will leave the system in a coherence on either the ground or excited electronic state during t_2, which informs our choice of central frequency of second pump pulse at $E/\hbar$, $E/\hbar + \Omega$, or $E/\hbar - \Omega$. With well separated pump pulses, we can be certain that for a given pulse sequence we are looking at signals that correspond to the DSFD showed in Figure 4.6 and we can use our ability to subdivide the signal pathways to learn about the dynamics of system and even resolve frequency shifts between ground and excited vibrational modes.

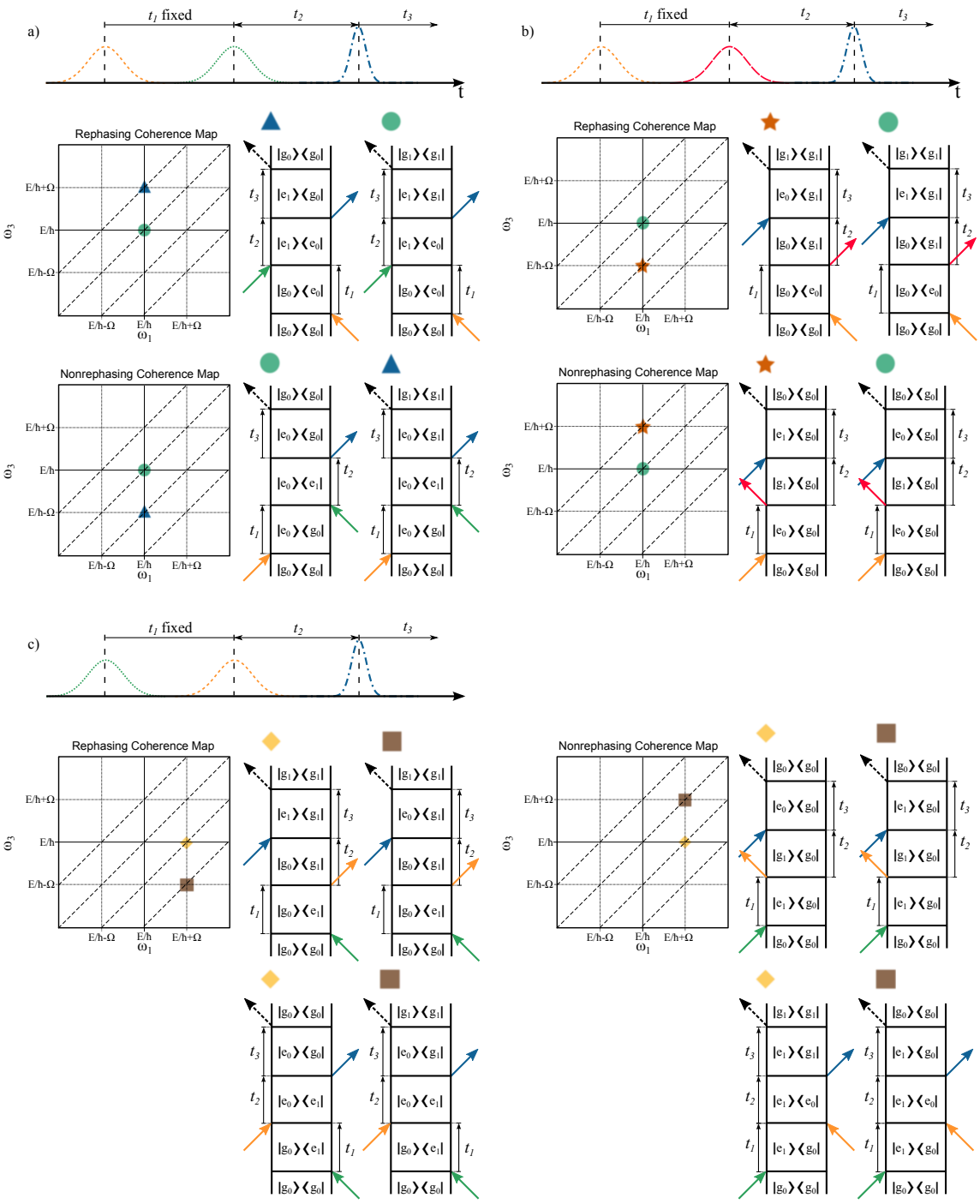

Figure 4.6: Differentiating signals from vibrational coherence on the excited and ground electronic states via T-RACS. Pulse sequences from Figure 4.1c-e for probing excited state (a), ground state (b), and both excited and ground state (c) coherences shown with resulting cartoon Fourier maps for a displaced oscillator model (Figure 4.2a). Rephasing and nonrephasing signals are generated by phase-matching conditions $k_s = -k_1 + k_2 + k_3$ and $k_s = k_1 - k_2 + k_3$, respectively, and are represented by Double-sided Feynman Diagrams (DSFD). The first pump pulse limits the excitation frequency and the second pump pulse limits which coherence is excited [1].

4.8.6 The role of t_1 delay in T-RACS experiments

The role of t_1 delay in T-RACS experiments The importance of imposing a t_1 delay between the two-color pump pulses in a T-RACS experiment depends on the experimental implementation that is used. In our experiment, we employ a hybrid diffractive-optic/pulse-shaping approach, described in detail in Chapter 2. A unique feature of this approach is the use of a pulse-shaper that creates the two-color pump pulse sequence and also enables phase-cycling. In this approach, rephasing and nonrephasing signals are collected simultaneously and can be separated by phase-cycling, even at t_1=0 fs. Figure 4.7 shows the Frobenius spectra of the rephasing and nonrephasing T-RACS signal for several different choices of t_1. As expected, the signal decays as t_1 increases. For all values of t_1 the rephasing and nonrephasing data report consistent frequencies within a few cm^{-1}. For other experimental geometries, it may be necessary to impose a nonzero t_1 to separate rephasing and nonrephasing T-RACS signals with the desired pulse-ordering. In the pump-probe geometry, rephasing and nonrephasing signals have the same phase-matching direction, being collinear with the probe pulse [46], [39], [47]. Although they cannot be separated by phase-matching, phase-cycling can be used [47]. Additional phase-cycling beyond what is used in a standard pump-probe geometry 2DES experiment will be necessary for separating rephasing and nonrephasing T-RACS signals with the desired color-ordering. Alternatively, a combination of phase-cycling and fixed t_1 delay of roughly the pump pulse duration could be used. In the standard BOXCARS implementation of 2DES (for example the diffractive-optic approach [40], [41]), the rephasing and nonrephasing signals emerge at different corners of the box. To facilitate collection of both signals at a single corner, the usual approach is to interchange the roles of the two pump pulses, scanning each backwards in time to record rephasing and nonrephasing signals in separate scans. With the two-color excitation used in T-RACS, interchanging the role of the two pump pulses alters the pulse-sequence and accesses different coherence pathways (depicted in Figure 4.2c-e). Without the possibility of phase-cycling, a standard BOXCARS 2DES setup cannot separate rephasing and nonrephasing T-RACS signals during pump pulse overlap. A simple implementation of T-RACS with a standard BOXCARS 2DES setup could involve adding bandpass filters to each pump arm to

select the desired two-color pump pulse sequence. To obtain rephasing and nonrephasing signals for a given T-RACS pulse sequence, the filters would need to be interchanged. Our hybrid pulse-shaping/diffractive optics-based approach avoids these complications by simultaneously collecting rephasing and nonrephasing signals.

4.8.7 Additional T-RACS Experiments Demonstrating the Breakdown of the Displaced Oscillator Model

The 2DES data from Chl a shows a distinct negative feature above the diagonal as seen in the absorptive 2D spectrum in Figure 4.9. This negative feature can be attributed to excited state absorption (ESA), which is not accounted for in the simple displaced oscillator model (Figure 4.2a) that does not include higher lying electronic states. Additional T-RACS experiments to those discussed above also show deviations from the displaced oscillator model. Using a sequence of spectrally-shaped pump pulses with central frequencies corresponding to $E/\hbar - \Omega$ and $E/\hbar$ (for pump one and pump two, respectively) we see coherence signals, shown in Figure 4.10, unexplained and unaccounted for within the displaced oscillator model. Using the same spectral shaping as used in Figure 4.1d but with inverted pump ordering, we see coherence amplitude in both the rephasing (Figure 4.10a) and nonrephasing (Figure 4.10b) signals for both two-color 2DES and T-RACS. The presence of some of these signals can be explained by inhomogeneous broadening and ESA; however these two contributions alone do not sufficiently explain the origin of these signals.

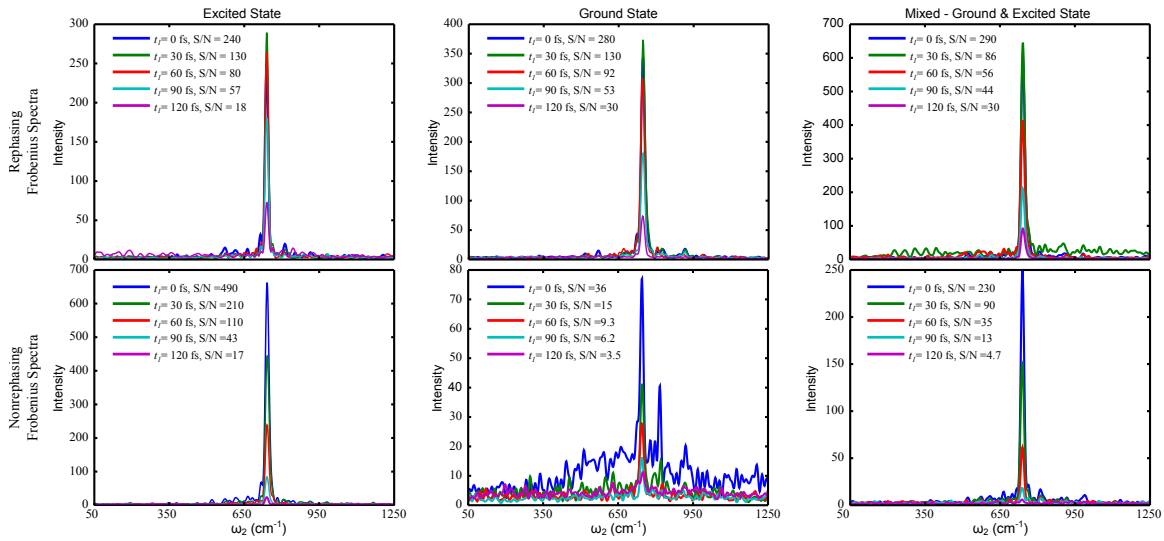

Figure 4.7: The rephasing (top row) and nonrephasing (bottom row) Frobenius spectra for five inter-pump pulse separation times, t_1=0, 30, 60, 90, 120 fs, for the three pulse sequences used (Figure 4.1c-e). Each plot shows a single peak around the 740 cm^{-1} coherence being studied; increasing pump-pulse separation, t_1, corresponds to a decrease in signal amplitude as well as a decrease in signal-to-noise (inset). There is no discernable t_1-dependence to the coherence frequency, ω_2 [1].

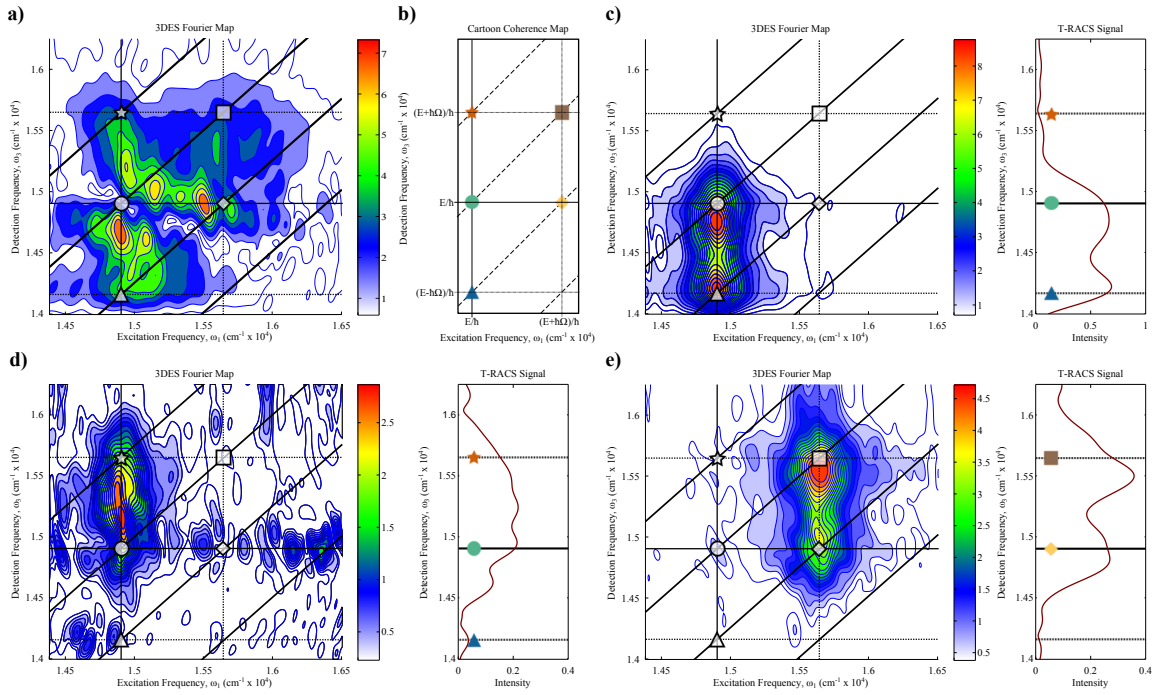

Figure 4.8: a) Nonrephasing Fourier map for ω_2=744 cm^{-1}, derived from the broadband 3DES data, roughly showing the characteristic chair pattern for a displaced oscillator but with much lower signal-to-noise than the rephasing signal shown in Figure 4.4a. b) Expected signals contributing to the nonrephasing Fourier map within the displaced oscillator model. Of particular interest are the excited state (blue triangle) and ground state (red star) coherence signals. Corresponding double-sided Feynman diagrams are given Figure 4.6. c)-e) Nonrephasing Fourier maps from two-color 3DES and corresponding T-RACS signals for the respective pulse sequences shown in Figure 4.1c)-e). Dotted lines indicate ω_1,ω_3=$E/\hbar - \Omega$ and $E/\hbar + \Omega$, solid lines indicate ω_1,ω_3=$E/\hbar$; along ω_3 the position of the blue triangle and orange star (within the displaced oscillator model) indicate excited state and ground state coherence respectively. Coherence frequencies (ω_2) for two-color 3DES (T-RACS) shown here are: c) 738 cm^{-1} (740 cm^{-1}), d) 745 cm^{-1} (746 cm^{-1}), e) 739 cm^{-1} (738 cm^{-1}). Contours are plotted in increments of 10% (a) and 5% for c-e, starting from 8% of the maximum intensity [1].

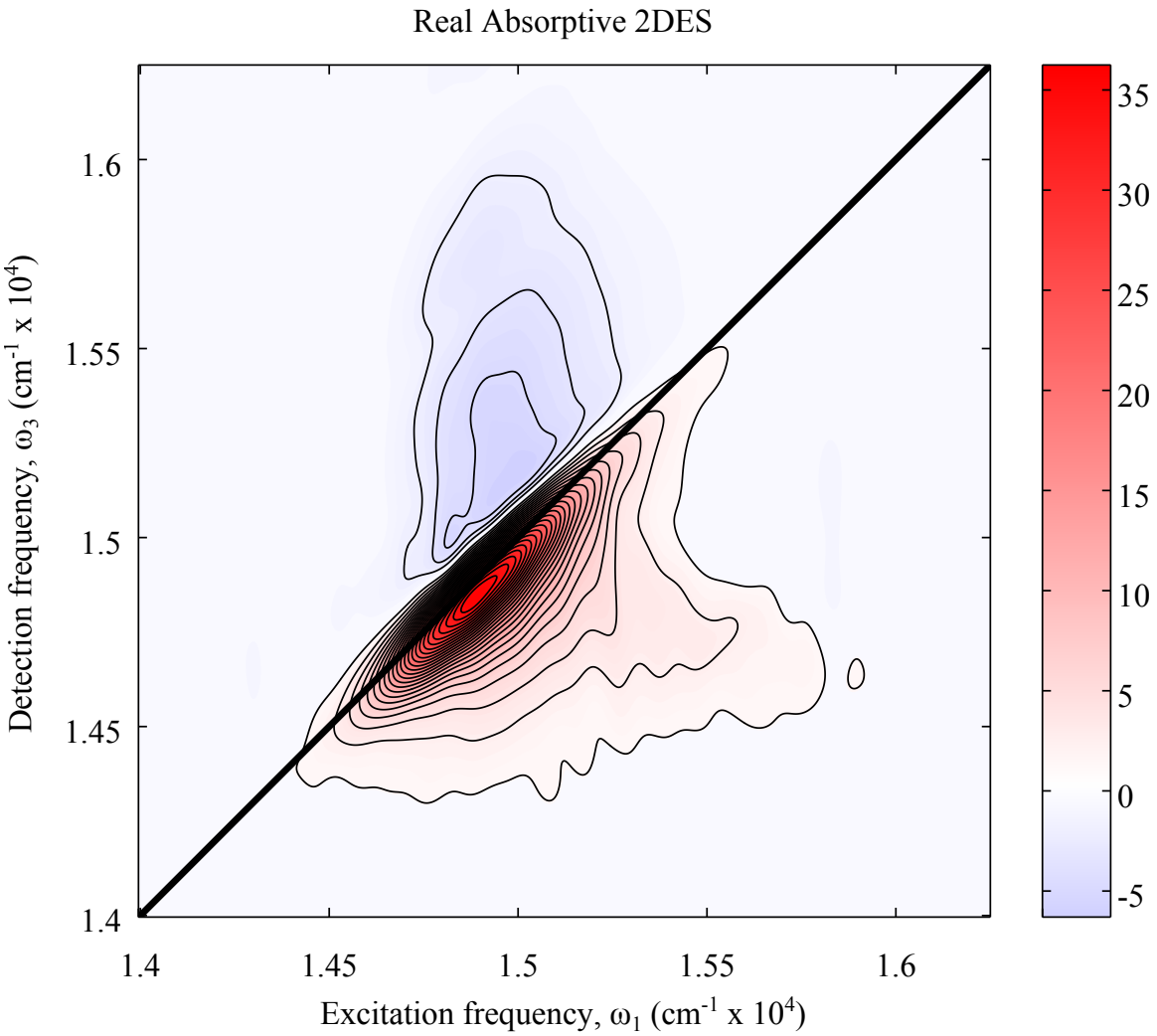

Figure 4.9: Absorptive 2DES spectrum of Chl a at 77 K, at t_2= 800 fs. Contours are plotted in increments of 3% [1].

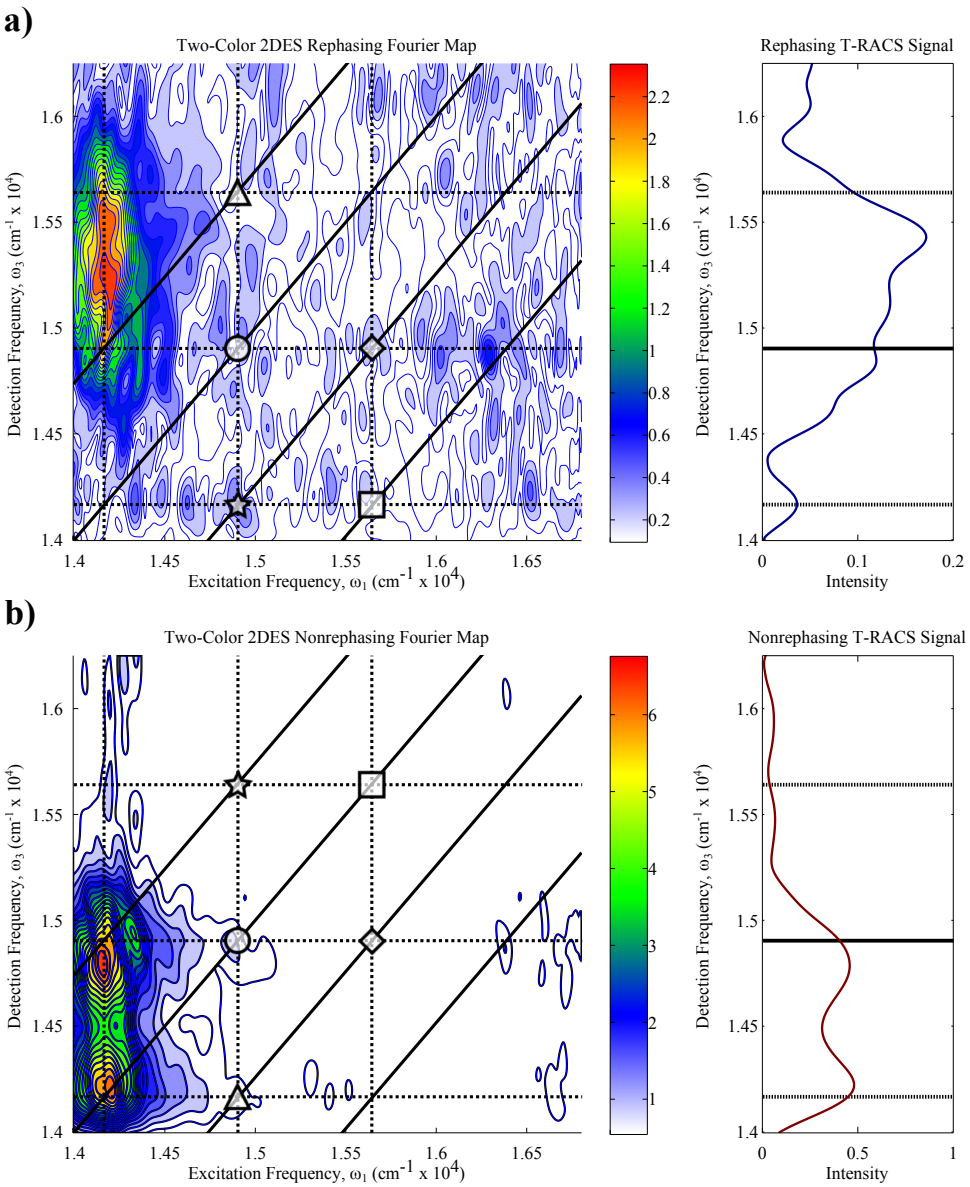

Figure 4.10: Two-color 2DES Fourier map and T-RACS signal for rephasing (top row) and non-rephasing (bottom row) signals with the first and second pump centered at $E/\hbar - \Omega$ and $E/\hbar$, respectively. The expected location of coherence signals for a displaced oscillator are shown with symbols. Contours are plotted in increments of 5% starting from 4% and 8% of the maximum intensity for the rephasing (a) and nonrephasing (b) data respectively [1].

References

[1] S. Seckin Senlik, Veronica R. Policht, and Jennifer P. Ogilvie. Two-color nonlinear spectroscopy for the rapid acquisition of coherent dynamics. *The Journal of Physical Chemistry Letters*, **6**:2413–2420, (2015).

[2] Derek G. Osborne and Kevin J. Kubarych. Rapid and accurate measurement of the frequency-frequency correlation function. *Journal of Physical Chemistry A*, **117**:5891–5898, (2013).

[3] S. (Shaul) Mukamel. *Principles of nonlinear optical spectroscopy*. Oxford University Press, New York, (1995).

[4] David Cotter Paul N. Butcher. *The Elements of Nonlinear Optics*, volume 9 of *Cambridge Studies in Modern Optics*. Cambridge University Press, Cambridge, (2003).

[5] John C. Wright. *Multiresonant Coherent Multidimensional Spectroscopy*, volume 62 of *Annual Review of Physical Chemistry*, pages 209–230. (2011).

[6] Hohjai Lee, Yuan-Chung Cheng, and Graham R. Fleming. Coherence dynamics in photosynthesis: Protein protection of excitonic coherence. *Science*, **316**:1462–1465, (2007).

[7] Ian Seungwan Ryu, Hui Dong, and Graham R. Fleming. Role of electronic-vibrational mixing in enhancing vibrational coherences in the ground electronic states of photosynthetic bacterial reaction center. *Journal of Physical Chemistry B*, **118**:1381–1388, (2014).

[8] Jordan M. Womick, Stephen A. Miller, and Andrew M. Moran. Toward the origin of exciton electronic structure in phycobiliproteins. *Journal of Chemical Physics*, **133**, (2010).

[9] G. H. Richards, K. E. Wilk, P. M. G. Curmi, H. M. Quiney, and J. A. Davis. Coherent vibronic coupling in light-harvesting complexes from photosynthetic marine algae. *Journal of Physical Chemistry Letters*, **3**:272–277, (2012).

[10] G. H. Richards, K. E. Wilk, P. M. G. Curmi, H. M. Quiney, and J. A. Davis. Excited state coherent dynamics in light-harvesting complexes from photosynthetic marine algae. *Journal of Physics B-Atomic Molecular and Optical Physics*, **45**, (2012).

[11] G. H. Richards, K. E. Wilk, P. M. G. Curmi, and J. A. Davis. Disentangling electronic and vibrational coherence in the phycocyanin-645 light-harvesting complex. *Journal of Physical Chemistry Letters*, **5**:43–49, (2014).

[12] Jonathan O. Tollerud, Christopher R. Hall, and Jeffrey A. Davis. Isolating quantum coherence using coherent multi-dimensional spectroscopy with spectrally shaped pulses. *Optics Express*, **22**:6719–6733, (2014).

[13] Patrick Wen and Keith A. Nelson. Selective enhancements in 2d fourier transform optical spectroscopy with tailored pulse shapes. *Journal of Physical Chemistry A*, **117**:6380–6387, (2013).

[14] Gregory S. Engel, Tessa R. Calhoun, Elizabeth L. Read, Tae-Kyu Ahn, Tomas Mancal, Yuan-Chung Cheng, Robert E. Blankenship, and Graham R. Fleming. Evidence for wavelike energy transfer through quantum coherence in photosynthetic systems. *Nature*, **446**:782–786, (2007).

[15] Elizabeth L. Read, Gregory S. Engel, Tessa R. Calhoun, Tom Manal, Tae Kyu Ahn, Robert E. Blankenship, and Graham R. Fleming. Cross-peak-specific two-dimensional electronic spec-

troscopy. *Proceedings of the National Academy of Sciences*, **104**:14203–14208, (2007).

[16] D. M. Jonas. Two-dimensional femtosecond spectroscopy. *Annual Review of Physical Chemistry*, **54**:425–463, (2003).

[17] Kristin L. M. Lewis and Jennifer P. Ogilvie. Probing photosynthetic energy and charge transfer with two-dimensional electronic spectroscopy. *Journal of Physical Chemistry Letters*, **3**: 503–510, (2012).

[18] Franz Milota, Valentyn I. Prokhorenko, Tomas Mancal, Hans von Berlepsch, Oliver Bixner, Harald F. Kauffmann, and Juergen Hauer. Vibronic and vibrational coherences in two-dimensional electronic spectra of supramolecular j-aggregates. *Journal of Physical Chemistry A*, **117**:6007–6014, (2013).

[19] Franklin D. Fuller, Jie Pan, Andrius Gelzinis, Vytautas Butkus, S. Seckin Senlik, Daniel E. Wilcox, Charles F. Yocum, Leonas Valkunas, Darius Abramavicius, and Jennifer P. Ogilvie. Vibronic coherence in oxygenic photosynthesis. *Nature Chemistry*, **6**:706–711, (2014).

[20] Vytautas Butkus, Donatas Zigmantas, Darius Abramavicius, and Leonas Valkunas. Distinctive character of electronic and vibrational coherences in disordered molecular aggregates. *Chemical Physics Letters*, **587**:93–98, (2013).

[21] Aurelia Chenu, Niklas Christensson, Harald F. Kauffmann, and Tomas Mancal. Enhancement of vibronic and ground-state vibrational coherences in 2d spectra of photosynthetic complexes. *Scientific Reports*, **3**, (2013).

[22] Vytautas Butkus, Donatas Zigmantas, Leonas Valkunas, and Darius Abramavicius. Vibrational vs. electronic coherences in 2d spectrum of molecular systems. *Chemical Physics Letters*, **545**:40–43, (2012).

[23] Vytautas Butkus, Leonas Valkunas, and Darius Abramavicius. Vibronic phenomena and exciton-vibrational interference in two-dimensional spectra of molecular aggregates. *Journal of Chemical Physics*, **140**, (2014).

[24] Dassia Egorova. Self-analysis of coherent oscillations in time-resolved optical signals. *Journal of Physical Chemistry A*, **118**:10259–10267, (2014).

[25] Daniel B. Turner, Rayomond Dinshaw, Kyung-Koo Lee, Michael S. Belsley, Krystyna E. Wilk, Paul M. G. Curmi, and Gregory D. Scholes. Quantitative investigations of quantum coherence for a light-harvesting protein at conditions simulating photosynthesis. *Physical Chemistry Chemical Physics*, **14**:4857–4874, (2012).

[26] Niklas Christensson, Harald F. Kauffmann, Tonu Pullerits, and Tomas Mancal. Origin of long-lived coherences in light-harvesting complexes. *Journal of Physical Chemistry B*, **116**: 7449–7454, (2012).

[27] M. H. Vos, F. Rappaport, J. C. Lambry, J. Breton, and J. L. Martin. Visualization of coherent nuclear motion in a membrane-protein by femtosecond spectroscopy. *Nature*, **363**:320–325, (1993).

[28] M. H. Vos, M. R. Jones, C. N. Hunter, J. Breton, and J. L. Martin. Coherent nuclear-dynamics at room-temperature in bacterial reaction centers. *Proceedings of the National Academy of Sciences of the United States of America*, **91**:12701–12705, (1994).

[29] Daniel B. Turner, Krystyna E. Wilk, Paul M. G. Curmi, and Gregory D. Scholes. Compar-

ison of electronic and vibrational coherence measured by two-dimensional electronic spectroscopy. *Journal of Physical Chemistry Letters*, **2**:1904–1911, (2011).

[30] Yin Song, Christoph Hellmann, Natalie Stingelin, and Gregory D. Scholes. The separation of vibrational coherence from ground- and excited-electronic states in p3ht film. *Journal of Chemical Physics*, **142**, (2015).

[31] Justin R. Caram, Andrew F. Fidler, and Gregory S. Engel. Excited and ground state vibrational dynamics revealed by two-dimensional electronic spectroscopy. *Journal of Chemical Physics*, **137**, (2012).

[32] Joachim Seibt and Tonu Pullerits. Beating signals in 2d spectroscopy: Electronic or nuclear coherences? application to a quantum dot model system. *Journal of Physical Chemistry C*, **117**:18728–18737, (2013).

[33] Marc Lutz. Resonance raman spectra of chlorophyll in solution. *Journal of Raman Spectroscopy*, **2**:497–516, (1974).

[34] Alison Telfer, Andrew A. Pascal, Luc Bordes, James Barber, and Bruno Robert. Fluorescence line narrowing studies on isolated chlorophyll molecules. *Journal of Physical Chemistry B*, **114**:2255–2260, (2010).

[35] E. J. G. Peterman, S. O. Wenk, T. Pullerits, L. O. Palsson, R. van Grondelle, J. P. Dekker, M. Rogner, and H. van Amerongen. Fluorescence and absorption spectroscopy of the weakly fluorescent chlorophyll a in cytochrome b(6)f of synechocystis pcc6803. *Biophysical Journal*, **75**:389–398, (1998).

[36] Margus Rtsep, Juha Linnanto, and Arvi Freiberg. Mirror symmetry and vibrational structure in optical spectra of chlorophyll a. *The Journal of Chemical Physics*, **130**:194501, (2009).

[37] Juan Du, Takahiro Teramoto, Kazuaki Nakata, Eiji Tokunaga, and Takayoshi Kobayashi. Real-time vibrational dynamics in chlorophyll a studied with a few-cycle pulse laser. *Biophysical Journal*, **101**:995–1003, (2011).

[38] Kenan Gundogdu, Katherine W. Stone, Daniel B. Turner, and Keith A. Nelson. Multidimensional coherent spectroscopy made easy. *Chemical Physics*, **341**:89–94, (2007).

[39] Sang-Hee Shim and Martin T. Zanni. How to turn your pump-probe instrument into a multidimensional spectrometer: 2d ir and vis spectroscopies via pulse shaping. *Physical Chemistry Chemical Physics*, **11**:748–761, (2009).

[40] M. L. Cowan, J. P. Ogilvie, and R. J. D. Miller. Two-dimensional spectroscopy using diffractive optics based phased-locked photon echoes. *Chemical Physics Letters*, **386**:184–189, (2004).

[41] T. Brixner, T. Mancal, I. V. Stiopkin, and G. R. Fleming. Phase-stabilized two-dimensional electronic spectroscopy. *Journal of Chemical Physics*, **121**:4221–4236, (2004).

[42] J. K. Gillie, G. J. Small, and J. H. Golbeck. Nonphotochemical hole burning of the native antenna complex of photosystem-i (psi-200). *Journal of Physical Chemistry*, **93**:1620–1627, (1989).

[43] T. Wilhelm, J. Piel, and E. Riedle. Sub-20-fs pulses tunable across the visible from a blue-pumped single-pass noncollinear parametric converter. *Optics Letters*, **22**:1494–1496, (1997).

[44] S. Kane and J. Squier. Grism-pair stretchercompressor system for simultaneous second- and third-order dispersion compensation in chirped-pulse amplification. *Journal of the Optical Society of America B*, **14**:661–665, (1997).

[45] Franklin D. Fuller, Daniel E. Wilcox, and Jennifer P. Ogilvie. Pulse shaping based two-dimensional electronic spectroscopy in a background free geometry. *Optics Express*, **22**: 1018–1027, (2014).

[46] Sarah M. Gallagher Faeder and David M. Jonas. Two-dimensional electronic correlation and relaxation spectra: theory and model calculations. *The Journal of Physical Chemistry A*, **103**: 10489–10505, (1999).

[47] Jeffrey A. Myers, Kristin L. M. Lewis, Patrick F. Tekavec, and Jennifer P. Ogilvie. Two-color two-dimensional fourier transform electronic spectroscopy with a pulse-shaper. *Optics Express*, **16**:17420–17428, (2008).

Chapter 5

Anion Band Studies

There has been considerable ongoing debate about the possible role of coherent dynamics in the function of the PSII RC. These questions remained unresolved due to the spectroscopic complexity of the system and the lack of clear spectral signatures of the constituent excitons, the charge separation intermediates, and the photoproduct states. The Q_y band (~680 nm) and the Pheophytin Q_x band (~580 nm) include spectral signatures for charge separation, $P680^+$ and Pheo a^-, as well as $P680^*$ (excited state absorption (ESA) of P680) and Pheo a^* (ESA of pheophytin). The spectral signatures of ESA and the markers for charge separation are similar which makes it difficult to directly observe the formation of the charge separated state (photo product). Similarly, the two anion bands located at ~460 nm and ~790-820 nm have spectral signatures for charge separation [1–3]. Unfortunately, Chl a^* (ESA of Chl a) has a broad absorption feature throughout this spectral range also making the interpretation of the signal difficult [1]. Unlike the other major bands in the PSII RC, there are few transient absorption studies related to the near-IR anion band (~790-820 nm) [1, 4, 5]. The recent observation of the coherent dynamics in the PSII RC has attracted a considerable interest and raised the question as to whether or not the formation of the charge separated state is coherent. In this chapter, we present the studies of the near-IR anion band in an effort to observe coherent formation of the photoproduct.

The functional role of coherent dynamics in the bacterial reaction centers (BRC) has attracted considerable interest for the last two decades. Many researchers have studied their importance in the primary charge transfer process [6–9]. Novoderezhkin and co-workers modeled the pri-

mary charge separation where they included the coupling between nuclear motions (vibrational coherences) and the primary charge separation. Their model was quite successful at explaining the observed features in the transient absorption measurements [8], and their conclusion was that two vibrational modes play key role in the high efficiency of charge separation in the BRC. While the BRCs and the PSII RC are different systems, the coherent dynamics in the PSII RC might be functionally similar to those in the BRCs.

In our previous work that reported coherences in the PSII RC, we reported theoretical simulations to investigate the origin and functionality of the observed coherent dynamics [10]. We used a dimeric special pair explicitly coupled to discrete vibrations, and a single charge transfer state was also included in the simulations. The population of the charge transfer state was calculated under several coupling conditions (e.g. vibrational modes at different frequencies, weakly damped and strongly damped vibrational modes) to test the functionality of these modes on the charge transfer. Figure 5.1 (depicted from [10]) shows a subset of the simulation results for the population of the charge transfer state. The simulations for the model where the coherent modes are weakly damped, revealed that ~340 cm^{-1} and ~250 cm^{-1} modes increase the population of the charge transfer state while ~740 cm^{-1} mode doesn't exhibit a similar behavior. One should note that, simulations show that the charge transfer state (product state) exhibit oscillations in intensity for all three cases regardless of their functionality. While the modeling of the coherent dynamics in the PSII RC shows that some of these modes are important in the charge separation [10], the experimental testing of their influence is a difficult task which still remains a challenge. The difficulty arises from the similar spectral signatures associated with different physical mechanisms in the ~790-820 nm spectral range. In the following, I will demonstrate why answering this question is a difficult task.

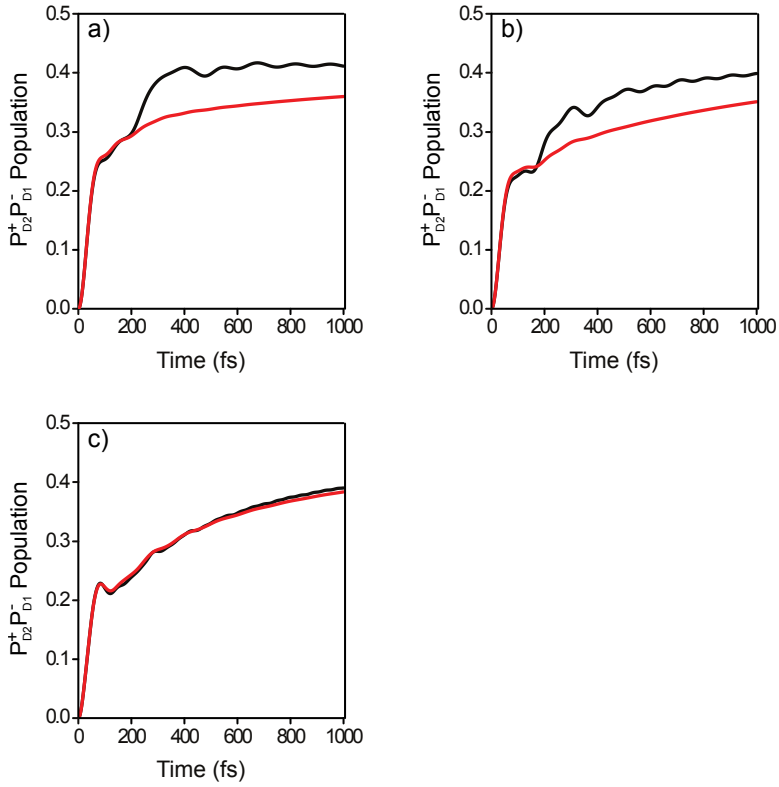

Figure 5.1: Simulated population dynamics of the charge transfer state for the weakly damped (red) and strongly damped (black) vibrational modes for three different modes a)~250 cm^{-1} mode, b)~340 cm^{-1}, c)~740 cm^{-1}[10].

Figure 5.2a shows a simplified energy level structure of the PSII RC when the primary charge separation is coupled to nuclear motion (vibrational coherence). The ground and excited state energy surfaces are modeled as the displaced harmonic oscillator, where the charge separated state (photo product state) is represented by S_{CS}. The eigenbasis of the displaced harmonic oscillator is given by: $\{|g_m\rangle, |e_n\rangle, m, n = 0, 1, 2..\infty\}$ at energies $\{\epsilon_{g_m} = (m + 1/2)\hbar\omega_0, \epsilon_{e_n} = \omega_{eg} + (n + 1/2)\hbar\omega_0\}$ where ω_{eg} is the transition energy between ground and excited state (see Chapter 3 for a more detailed description). The intermediate levels for the charge separation haven't been shown in this simple model. The charge separation begins with the excitation of the system, followed by a creation of coherence(and/or population) on the excited state energy surface. Next, this excitation is converted to a charge separated state. This conversion can be probed by monitoring the transition from the product state from S_{CS} to F_{CS}. Experimentally, the transition wavelength range corresponds to the anion band ~790-820 nm. The transient absorption signal (or two dimensional electronic spectroscopy signal) of this transition is expected to exhibit oscillatory behavior at frequency ω_0 during the waiting time in addition to signals from population dynamics, similar to the simulations shown in Figure 5.1. The experimental observation of the coherent dynamics in the anion band might be an indication of that this vibrational mode is important for the charge separation mechanism. However, observation of coherent dynamics do not guarantee that this particular mode enhance the charge separation; additional studies should be done. Moreover, similar models (e.g. models including vibronic and/or electronic coherences) can be employed to describe the system more accurately. Here, I illustrated how a vibrational mode can yield modulations in the anion band. As noted above, Chl a has ESA features through this spectral range which can exhibit similar spectral signatures to those of product state formation. I used the model, which is depicted in Figure 5.2b, to demonstrate the ESA of Chl a. The model includes the displaced harmonic oscillator with an additional excited state energy surface (F). In this model, the pump pulses create a coherence(and/or population) on the excited state energy surface followed by a transition from the excited state energy surface to the vibrational levels on F during a transient absorption measurement (or 2DES measurement). Unfortunately, this transition will show oscillatory behav-

ior during the waiting time, where the frequency of the oscillation will equal to ω_0. Overall, the detected signal in the ~790-820 nm range will be the summation of signals arising from the formation of product states due to the charge separation event and from the ESA of Chl a. Similarly the coherent dynamics, if they exist, might have different origins: formation of product state, ESA of Chl a, or a mixture of both signal. While the observation of coherent dynamics in ~790-820 nm spectral range don't confirm/guarantee their origin or functionality, the coherent dynamics in the anion band should be observed if they exist. Given the difficulty and complexity of the spectral signatures in the anion band, I aimed to present a ground work to examine the anion band by utilizing transient absorption spectroscopy and T-RACS. My goal is to characterize the spectral signatures of Chl a ESA and the anion band, and to examine if coherent dynamics modulate these different spectral signatures.

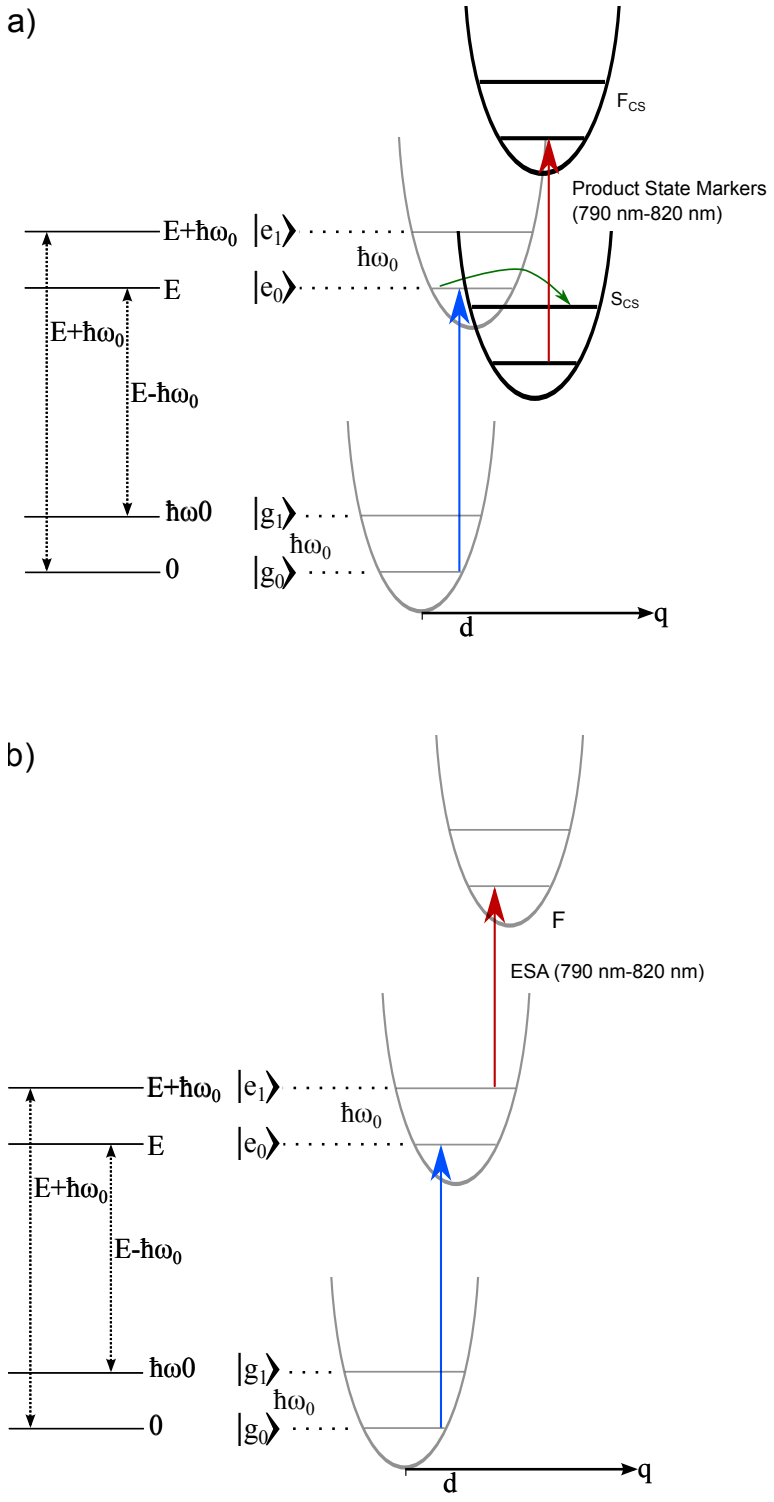

Figure 5.2: a) The model where a discrete vibrational coherence is coupled to charge transfer pathway for the PSII RC. b) The model including the excited state absorption for Chl a. The blue arrow shows the steps for preparation of coherence in the excited state energy surface. The red arrow shows the markers for the formation of product state (charge separation) and excited state absorption in a) and b) respectively. ω_0 is the frequency characterizing the displaced harmonic oscillator model. E corresponds to the Q_y band in the PSII RC.

5.1 Transient Absorption Studies on the Anion Band

Wasielewski and co-workers examined the near-IR PSII RC anion band by utilizing the transient absorption spectroscopy in late 80s and early 90s. They used a pulse centered at 610 nm with 100 uJ energy and white light with 500 fs duration to stimulate the system and probe the changes in system respectively [1, 3]. They first reported transient absorption measurements at 15 K, followed by studies at room temperature. Figure 5.4a, depicted from [1], shows the transient absorption spectrum reported at 10 ps. They assigned the positive features between 760 nm and 840 nm in the signal to the formation of Pheophytin$^-$(~790 nm) and the formation of P680$^+$ (~820 nm), and the absorption of Chl a$^+$. Figure 5.4b, depicted from [1], shows the evolution of the transient absorption signal at 820 nm, which exhibits a monoexponentially rising character. This feature was assigned to the P680$^+$. To the best of our knowledge, there is no other similar experimental study focusing on the anion band since Wasielewski's work.

Our attempts to observe population dynamics with transient grating absorption spectroscopy and 2D electronic spectroscopy were unsuccessful due to the low signal to noise ratio of the dispersed signal in the weak anion band region. The major challenge is the requirement of the "global phasing" procedure to obtain the real part of the relevant signals. The global phasing attempts were inconsistent and unsuccessful due to low signal to noise and the high amplitude of pump scatter on the red edge of the measured signal. Therefore, we utilized transient absorption to study the PSII RC anion band to probe the population dynamics in the system.

Here we report frequency resolved transient absorption measurement of the PSII RC in the anion band followed by the excitation of the Q_y band. See 5.2.1 for details of the measurements. Figure 5.5 shows the transient absorption spectrum at a waiting time, t_2=2 ps. The negative feature observed at the blue edge of spectrum is assigned to be stimulated emission from Q_y band. The broad positive feature which spans from 740 nm to 860 nm is consistent with the contribution from the formation of Pheophytin$^-$ and P680$^+$, as well as ESA of Chl a$^+$. Figure 5.6 shows the change of the transient absorption signal as a function of waiting time, t_2, for three probe wavelengths: 820 nm, 804 nm, and 790 nm. 820 nm and 790 nm are chosen to exhibit P680$^+$ and Pheophytin$^-$

formation, whereas 804 nm is chosen to show typical behavior in the 790-820 nm spectral range. Unlike the earlier reports by Wasielewski in this spectral range, we do not observe a pure rise consistent with the formation of a product state. Instead, our observation can be described by the summation of the ESA of Chl a (an exponentially decaying signal) and the formation of product state (rising signal). The strongest clue for this assignment is the non zero transient absorption signal at 50 ps. We have been investigating the difference between our observations and earlier reports; while the experimental conditions (e.g. temperature, pump pulse wavelength) are different between experiments, further experimental studies should be done to investigate this band. We note that the pulse energies used by Wasielewski are considerably higher than in our experiments.

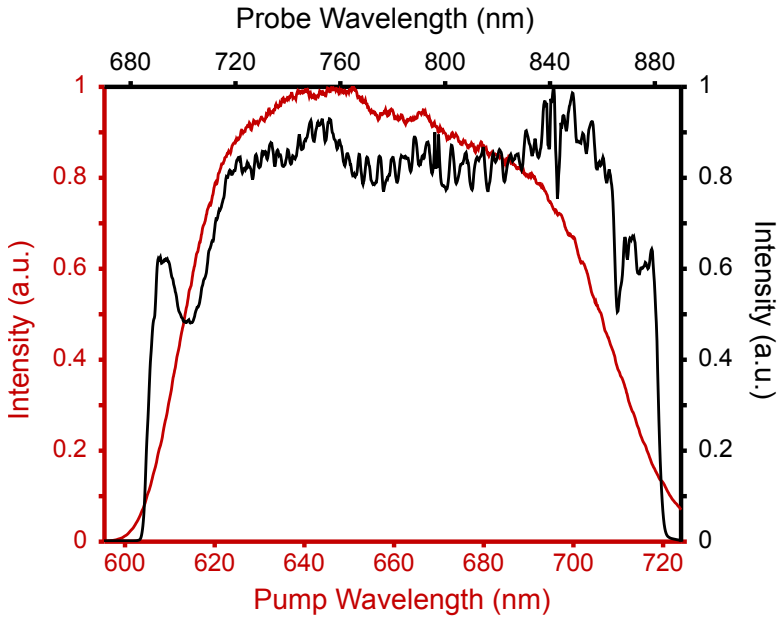

Figure 5.3: The spectrum of probe (black) and pump (red) pulses used in transient absorption measurements.

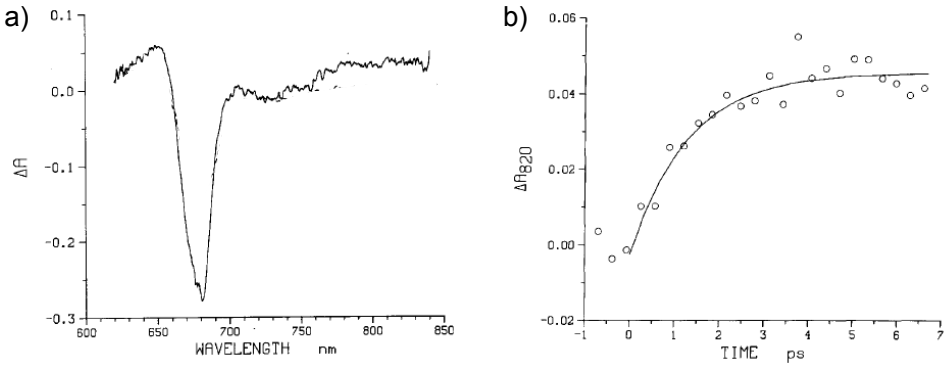

Figure 5.4: a) The PSII RC transient absorption spectrum reported at 10 ps [1]. b)The transient absorption changes at 820 nm for PSII RC [1].

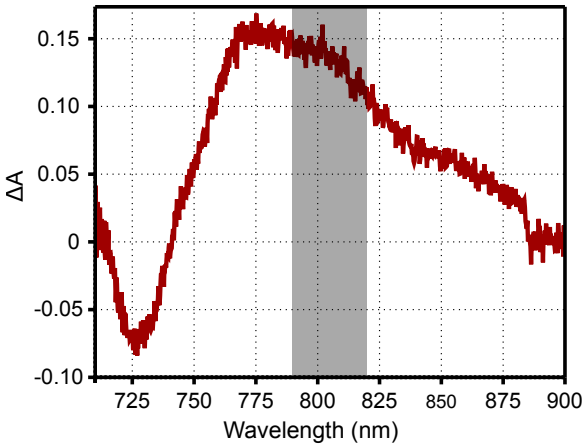

Figure 5.5: The PSII RC transient absorption spectrum measured at 2 ps. The grey area represents the anion band spectral range

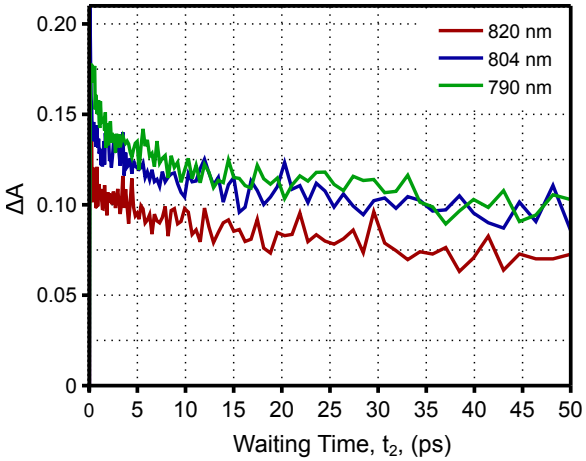

Figure 5.6: The change of transient absorption signal as a function of waiting time, t_2, for three probe wavelengths: 820 nm (red), 804 nm (blue), 790 nm (green)

5.2 Observation of Coherent Dynamics in the Anion Band

We employed the experimental apparatus, which is described in Chapter 2, and the T-RACS method, which is described in Chapter 4, to examine coherent dynamics in the anion band. For examining different modes separately, we performed successive T-RACS measurements for different pump pulse sequences with the appropriate frequency difference to observe particular coherences. We choose two pump spectra that include $E/\hbar$ and $E/\hbar + \Omega$ where E corresponds to the main electronic transition being excited and Ω is the frequency of the mode being excited. We set our pulse order to the one described in Figure 4b to observe excited state coherence. The time delay between pump pulses is set to t_1=0 fs to achieve the highest signal to noise ratio. This configuration yields the detection of signal in which both the ground and the excited states are involved. A more detailed discussion of pump pulse sequence is presented in Chapter 4. Section 5.2.2 provides details of the measurement and data analysis.

Figure 5.7-5.15 show pump pulse spectra, the rephasing and nonrephasing Frobenius spectra as well as coherence maps for different T-RACS measurements. The rephasing and nonrehasing coherence maps examining the ~250 cm^{-1}, 350 cm^{-1}, 750 cm^{-1},and 950 cm^{-1} modes show significant amplitude along the detection axis. The amplitude of the peaks change significantly depending on the detection wavelength and the pulse sequence employed. The T-RACS experiments employing the 750 cm^{-1} and 950 cm^{-1} modes shows significant amplitude in the anion band range, ~790-820 nm, as shown in Figure 5.12 and Figure 5.14 respectively. Another interesting feature is the pattern observed along the detection axis. Figure 5.12d exhibits two major peaks along the detection axis for ω_2=~740 cm^{-1}. A first peak is located at ~735 nm and another at ~780 nm. The 780 nm peak is elongated along λ_3 while the 735 nm one doesn't show much elongation. A similar behavior is observed in Figure 5.12c also. Figure 5.13d shows amplitude for several modes, however only the ~740 cm^{-1} mode is observed in longer wavelengths while the others are observed in shorter wavelengths.

In a typical T-RACS experiment, as shown in Chapter 4 and above, narrow band pump pulses are used to selectively excite one mode/or multiple modes within the excitation range of pump

pulses used. Here, we extend our approach on T-RACS, which is based on narrow band pump pulses to employ relatively broadband pump pulses for the excitation. The motivation behind this modification is to excite and observe all the modes simultaneously, while suppressing population contributions. Figure 5.16 shows the spectral shapes used to create pump pulses. The original input pulse delivered by the NOPA is split such that one pulse covers frequencies from $E/\hbar$+110 cm^{-1} to the lowest frequency of the input pulse whereas the other pulse covers the remaining frequencies of the input pulse. Two pump pulses do not spectrally overlap and the contributions from populations are suppressed. Figure 5.16b show the Frobenius spectra for the rephasing and nonrephasing signal, which show the major modes observed. The rephasing coherence map, Figure 5.16c, shows significant amplitude for many modes in the ~720-760 nm range. The modes in ~850-950 cm^{-1} range also has amplitude in the anion band range. Figure 5.16d shows the nonrephasing coherence map for the same experiment. The modes between 200 cm^{-1} and 400 cm^{-1} have not been observed in the nonrephasing signal. In the nonrephasing coherence map, ~740 cm^{-1} mode and ~950 cm^{-1} modes have significantly higher amplitude than other modes in the anion band range. Additionally, the black dashed line in Figure 5.16d presents a border line, where the modes $\geqslant$500 cm^{-1} are not observed below this line.

Here, we report the observation of coherent dynamics in the putative anion band region (~790-820 nm) of the PSII RC. We do not yet have a clear understanding of the origin of the coherence due to the complexity and overlap of many spectral signatures of different physical origin. This work presents a first observation of coherent dynamics in the PSII RC in this spectral range. Additional experimental and theoretical studies remained to be performed to increase our understanding about the origin of coherent dynamics in this spectral range and ultimately the importance of coherence in the function of the PSII RC. I will discuss some of the future studies in the following chapter.

5.2.1 Appendix 1

We used the experimental apparatus described in Chapter 2 to collect the data presented in this section. Pulses delivered by the NOPA and DOPA were used as pump and probe respectively. The

spectra of both pulses are shown in Figure 5.3. The duration of pump and probe were measured to be 12 fs and 13 fs respectively.

5.2.2 Appendix 2

The probe pulse delivered from the DOPA, which is centered at 800 nm, was compressed to 13 fs and kept the same for all measurements. Pump pulses with less than 2 nJ energy correspond to less than 4% excitation per reaction center in PSII RC sample to avoid exciton annihilation effects. The T-RACS measurements at t_2=(200,210,...,2000) fs, form a two dimensional data stack, $S(t_1$=$0, t_2, \lambda_3)$. To extract the information about coherent dynamics we performed Fourier transform along the waiting time, t_2. This transformation yields the rephasing(nonrephasing) coherence maps which show the correlation between detection wavelength, λ_3, and the frequency of the observed modes, ω_2. The Frobenius spectra for T-RACS experiments were obtained following the Fourier transformation above using detection wavelengths between 735-833 nm.

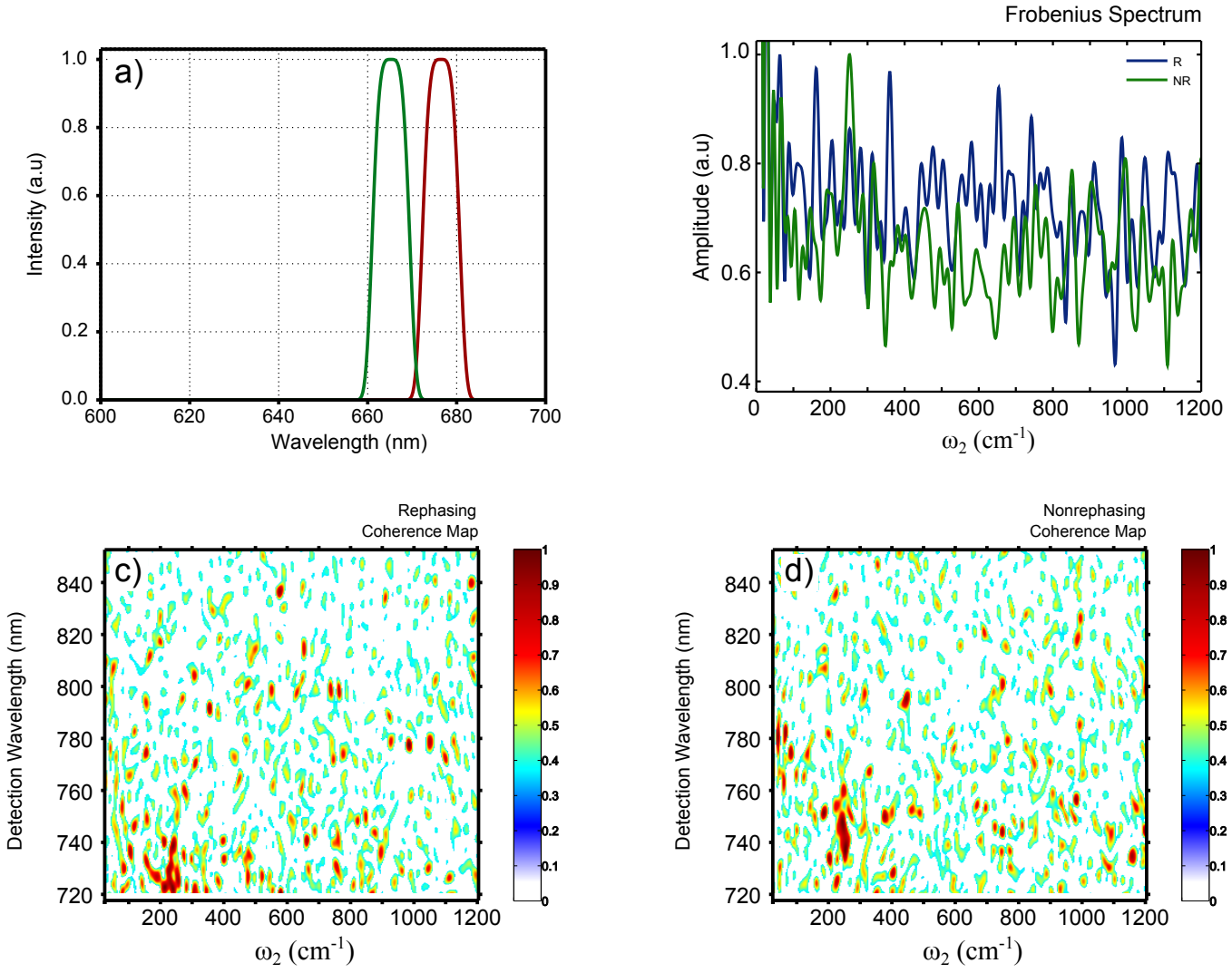

Figure 5.7: a) The amplitude shapes used to create pump pulses in TRACS to excite ground and excited coherences (250 cm^{-1} mode). b) Frobenius spectrum calculated for the rephasing (blue) and the nonrephasing signal (green). c) The Rephasing coherence map showing the distribution of amplitude of coherences as a function of detection wavelength. The regions with less than 0.35 peak amplitude is set to shown as white. d) The Nonrephasing coherence map showing the distribution of amplitude of coherences as a function of detection wavelength. The regions with less than 0.35 peak amplitude are set to shown as white.

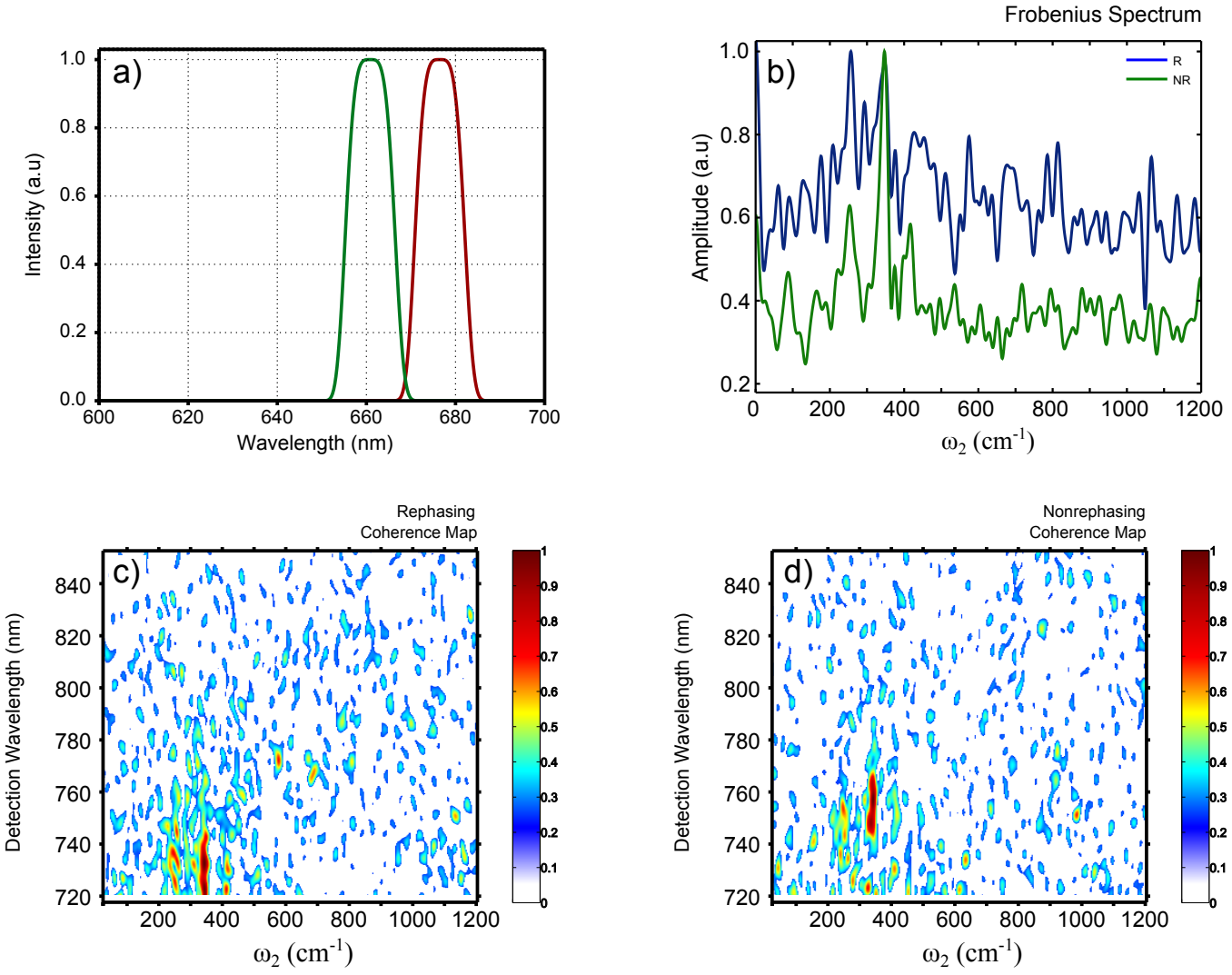

Figure 5.8: a) The amplitude shapes used to create pump pulses in TRACS to excite ground and excited coherences (350 cm^{-1} mode). b) Frobenius spectrum calculated for the rephasing (blue) and the nonrephasing signal (green). c) The Rephasing coherence map showing the distribution of amplitude of coherences as a function of detection wavelength. The regions with less than 0.25 peak amplitude is set to shown as white. d) The Nonrephasing coherence map showing the distribution of amplitude of coherences as a function of detection wavelength. The regions with less than 0.25 peak amplitude are set to shown as white.

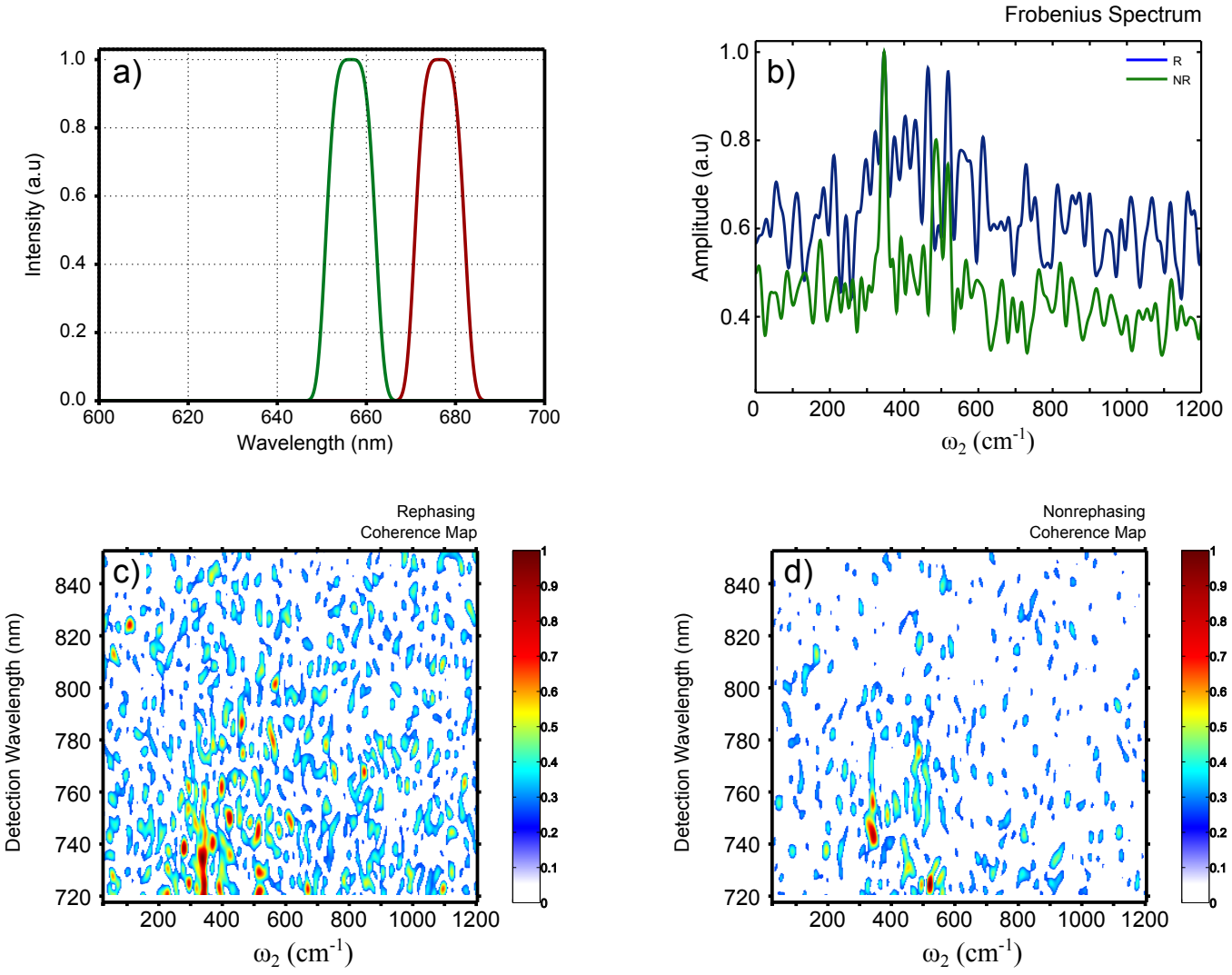

Figure 5.9: a) The amplitude shapes used to create pump pulses in TRACS to excite ground and excited coherences (450 cm^{-1} mode). b) Frobenius spectrum calculated for the rephasing (blue) and the nonrephasing signal (green). c) The Rephasing coherence map showing the distribution of amplitude of coherences as a function of detection wavelength. The regions with less than 0.25 peak amplitude is set to shown as white. d) The Nonrephasing coherence map showing the distribution of amplitude of coherences as a function of detection wavelength. The regions with less than 0.25 peak amplitude are set to shown as white.

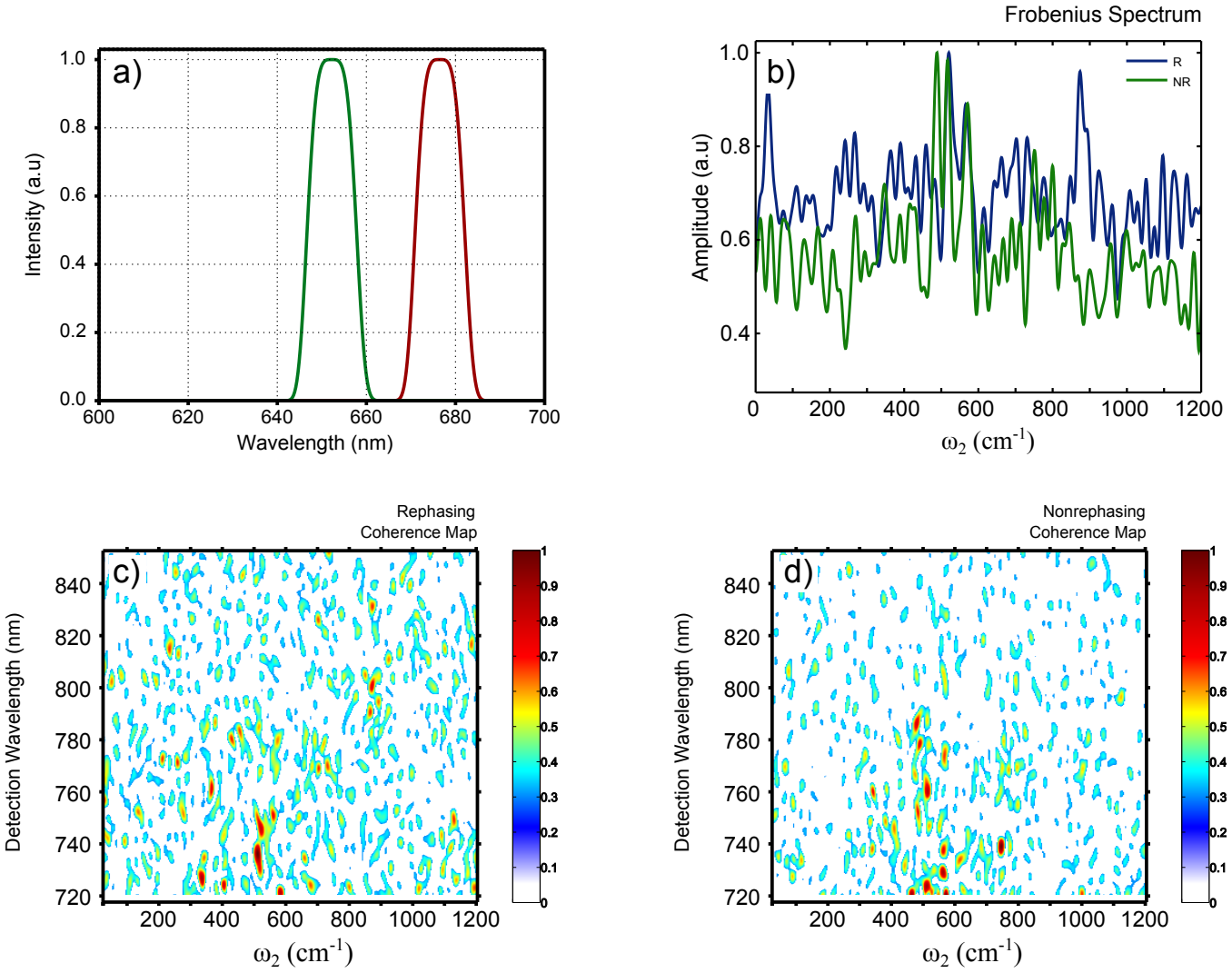

Figure 5.10: a) The amplitude shapes used to create pump pulses in TRACS to excite ground and excited coherences (550 cm^{-1} mode). b) Frobenius spectrum calculated for the rephasing (blue) and the nonrephasing signal (green). c) The Rephasing coherence map showing the distribution of amplitude of coherences as a function of detection wavelength. The regions with less than 0.30 peak amplitude is set to shown as white. d) The Nonrephasing coherence map showing the distribution of amplitude of coherences as a function of detection wavelength. The regions with less than 0.30 peak amplitude are set to shown as white.

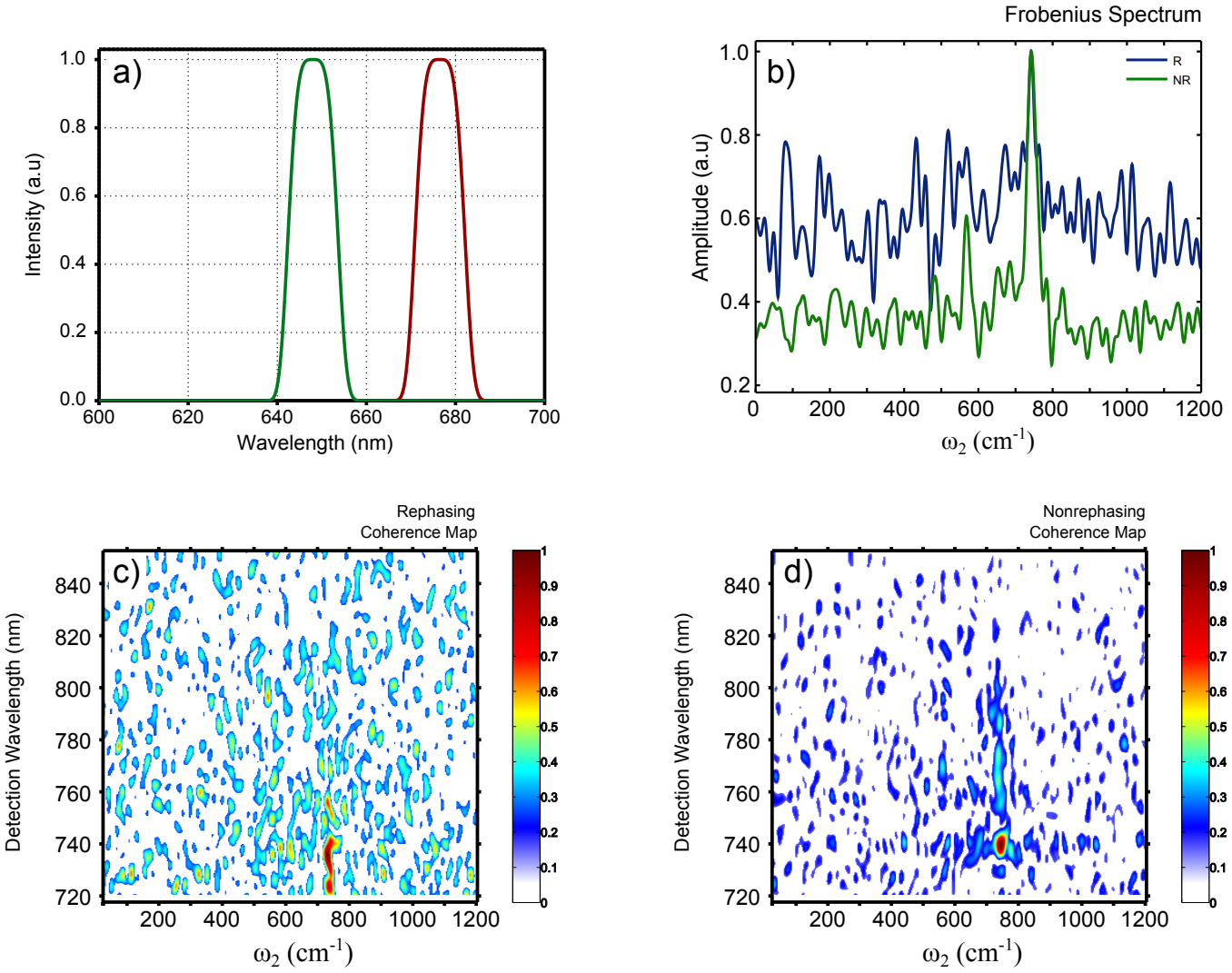

Figure 5.11: a) The amplitude shapes used to create pump pulses in TRACS to excite ground and excited coherences (650 cm^{-1} mode). b) Frobenius spectrum calculated for the rephasing (blue) and the nonrephasing signal (green). c) The Rephasing coherence map showing the distribution of amplitude of coherences as a function of detection wavelength. The regions with less than 0.25 peak amplitude is set to shown as white. d) The Nonrephasing coherence map showing the distribution of amplitude of coherences as a function of detection wavelength. The regions with less than 0.15 peak amplitude are set to shown as white.

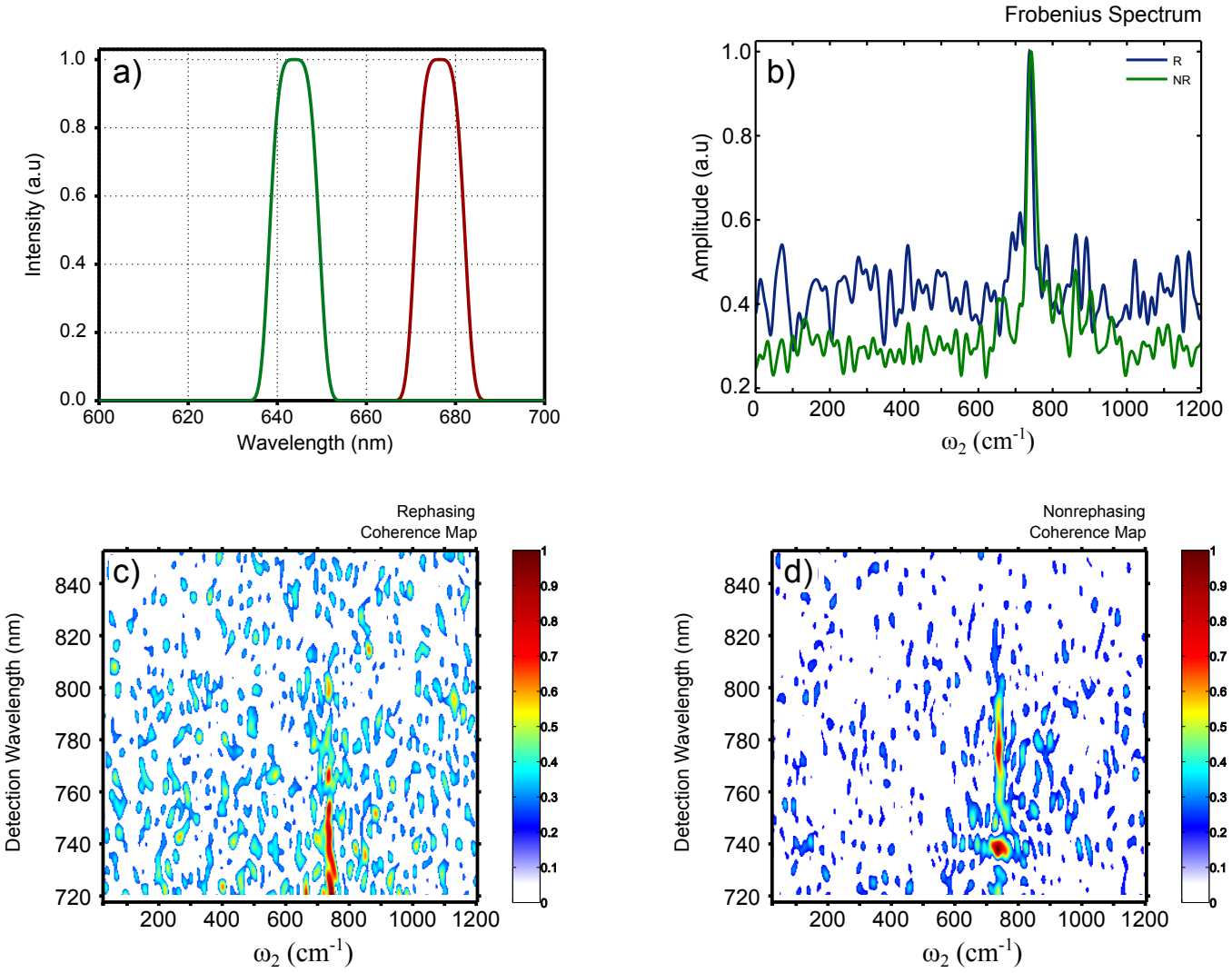

Figure 5.12: a) The amplitude shapes used to create pump pulses in TRACS to excite ground and excited coherences (750 cm^{-1} mode). b) Frobenius spectrum calculated for the rephasing (blue) and the nonrephasing signal (green). c) The Rephasing coherence map showing the distribution of amplitude of coherences as a function of detection wavelength. The regions with less than 0.25 peak amplitude is set to shown as white. d) The Nonrephasing coherence map showing the distribution of amplitude of coherences as a function of detection wavelength. The regions with less than 0.20 peak amplitude are set to shown as white.

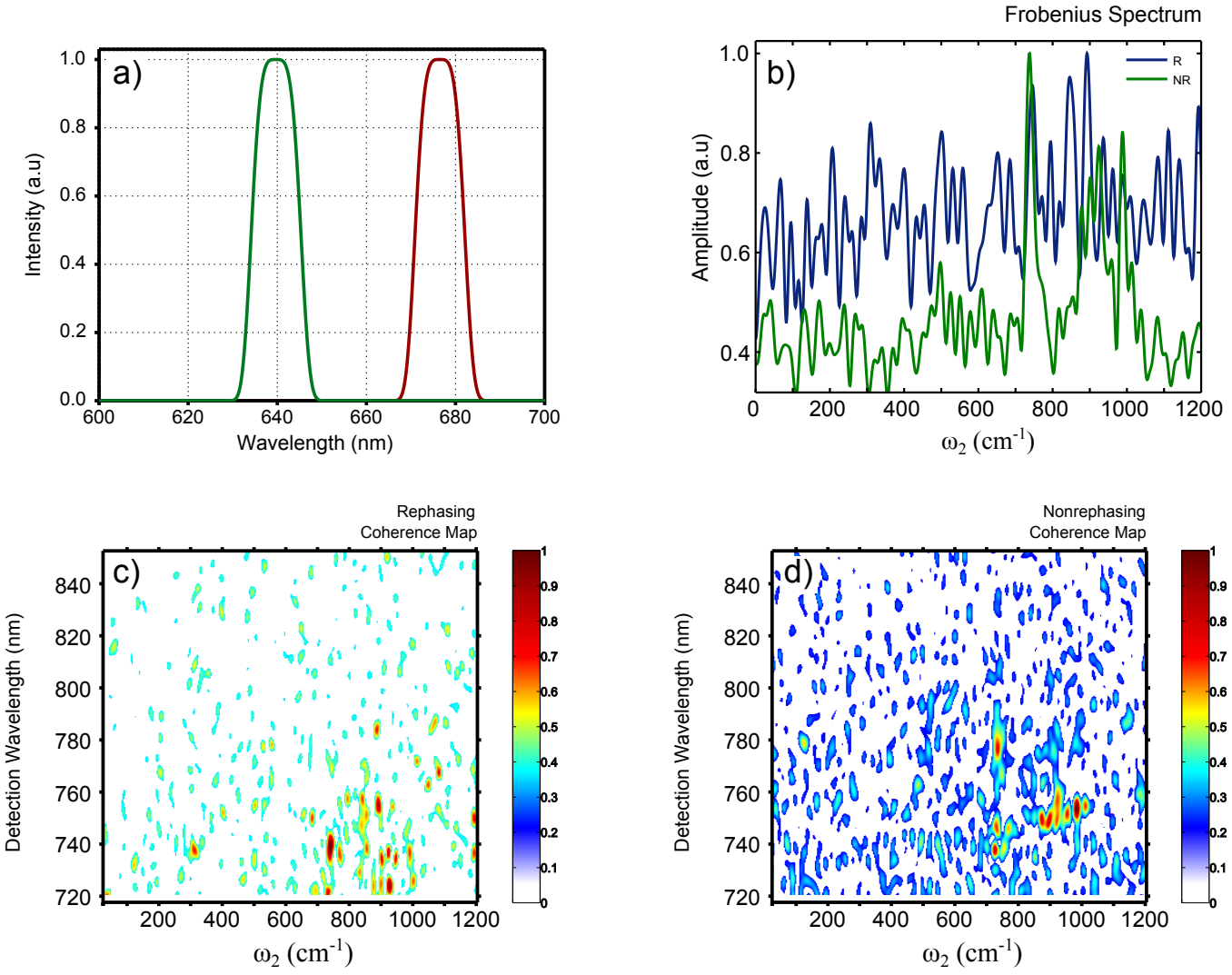

Figure 5.13: a) The amplitude shapes used to create pump pulses in TRACS to excite ground and excited coherences (850 cm^{-1} mode). b) Frobenius spectrum calculated for the rephasing (blue) and the nonrephasing signal (green). c) The Rephasing coherence map showing the distribution of amplitude of coherences as a function of detection wavelength. The regions with less than 0.35 peak amplitude is set to shown as white. d) The Nonrephasing coherence map showing the distribution of amplitude of coherences as a function of detection wavelength. The regions with less than 0.20 peak amplitude are set to shown as white.

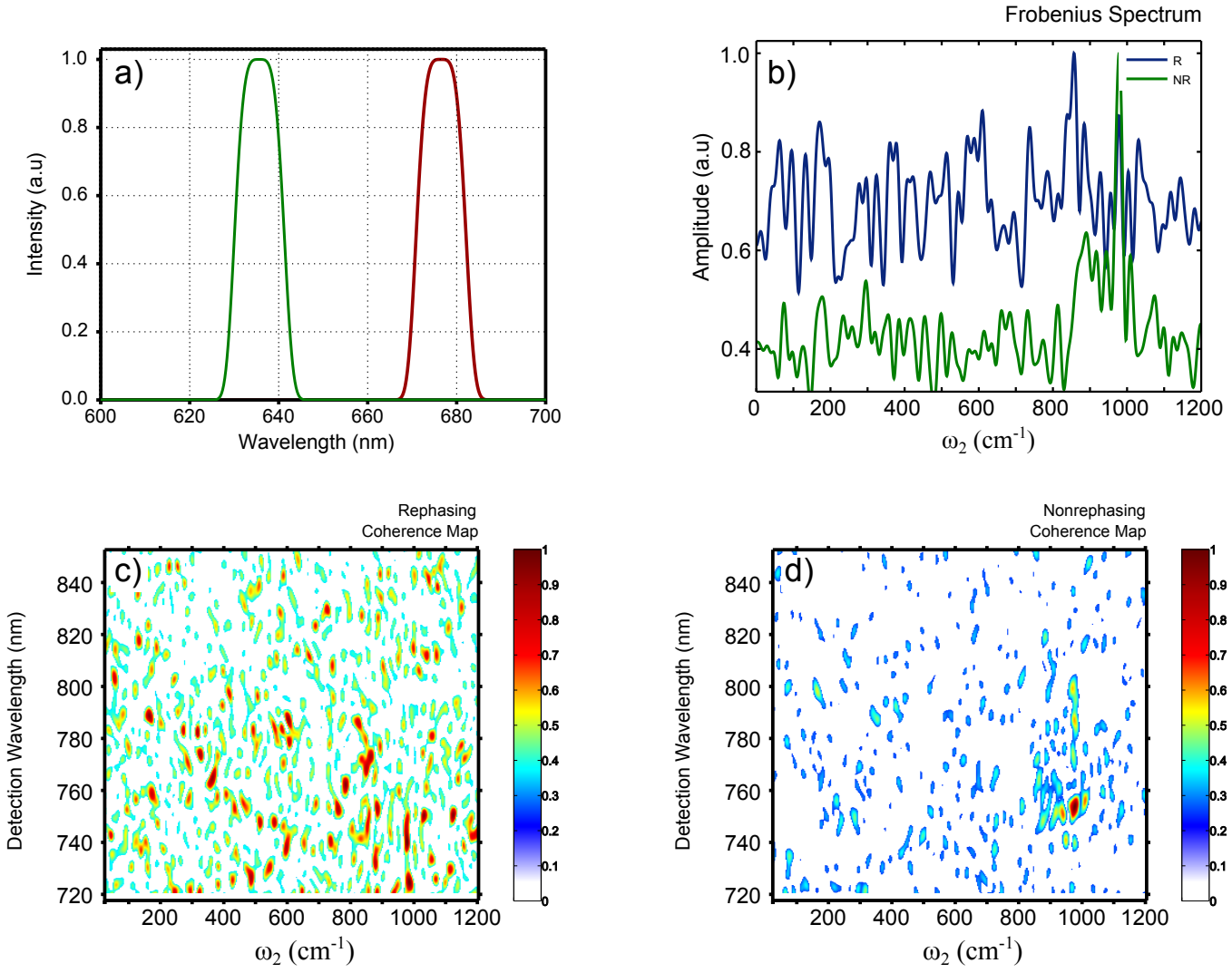

Figure 5.14: a) The amplitude shapes used to create pump pulses in TRACS to excite ground and excited coherences (950 cm^{-1} mode). b) Frobenius spectrum calculated for the rephasing (blue) and the nonrephasing signal (green). c) The Rephasing coherence map showing the distribution of amplitude of coherences as a function of detection wavelength. The regions with less than 0.35 peak amplitude is set to shown as white. d) The Nonrephasing coherence map showing the distribution of amplitude of coherences as a function of detection wavelength. The regions with less than 0.25 peak amplitude are set to shown as white.

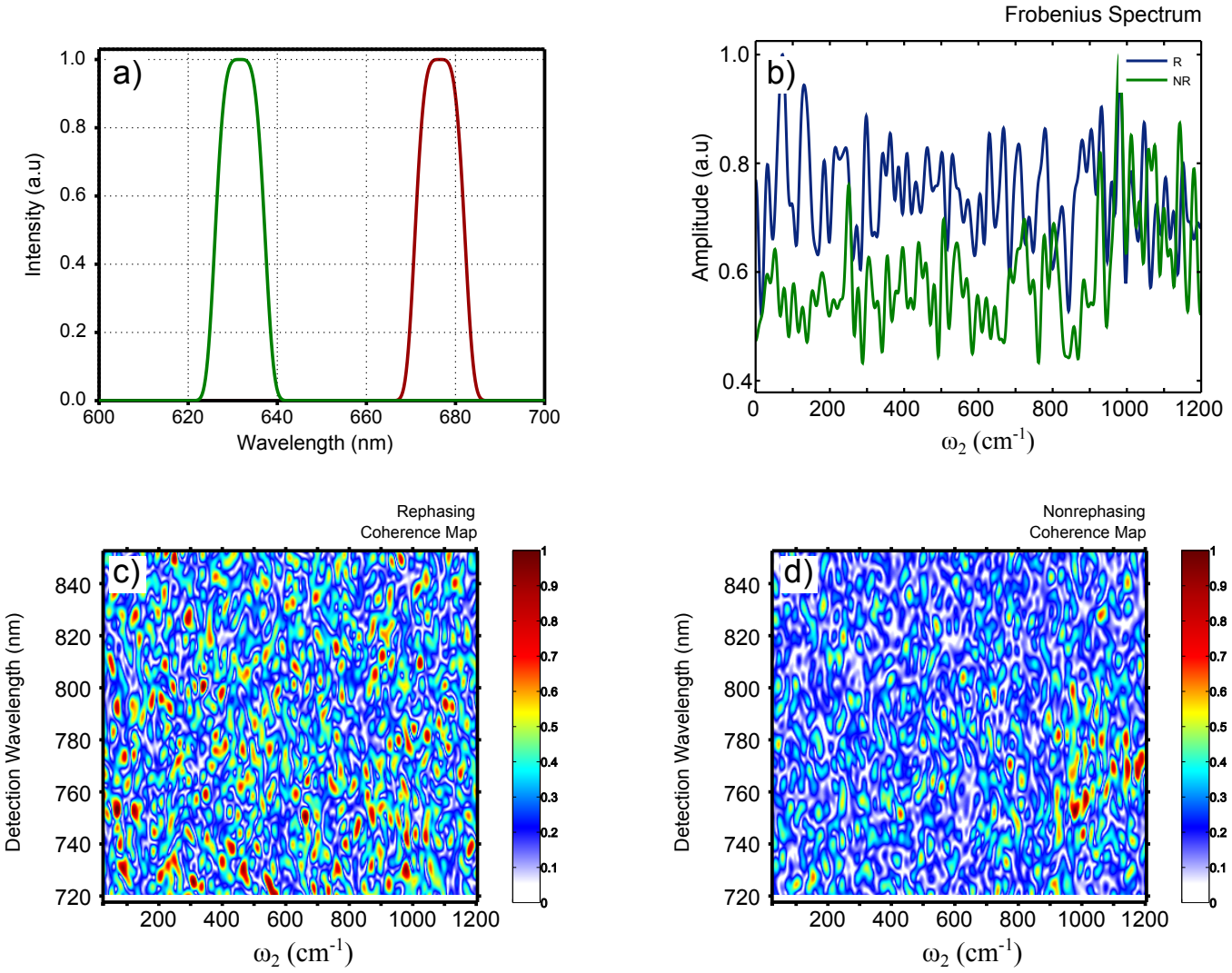

Figure 5.15: a) The amplitude shapes used to create pump pulses in TRACS to excite ground and excited coherences (1050 cm^{-1} mode). b) Frobenius spectrum calculated for the rephasing (blue) and the nonrephasing signal (green). c) The Rephasing coherence map showing the distribution of amplitude of coherences as a function of detection wavelength. The regions with less than 0.35 peak amplitude is set to shown as white. d) The Nonrephasing coherence map showing the distribution of amplitude of coherences as a function of detection wavelength. The regions with less than 0.35 peak amplitude are set to shown as white.

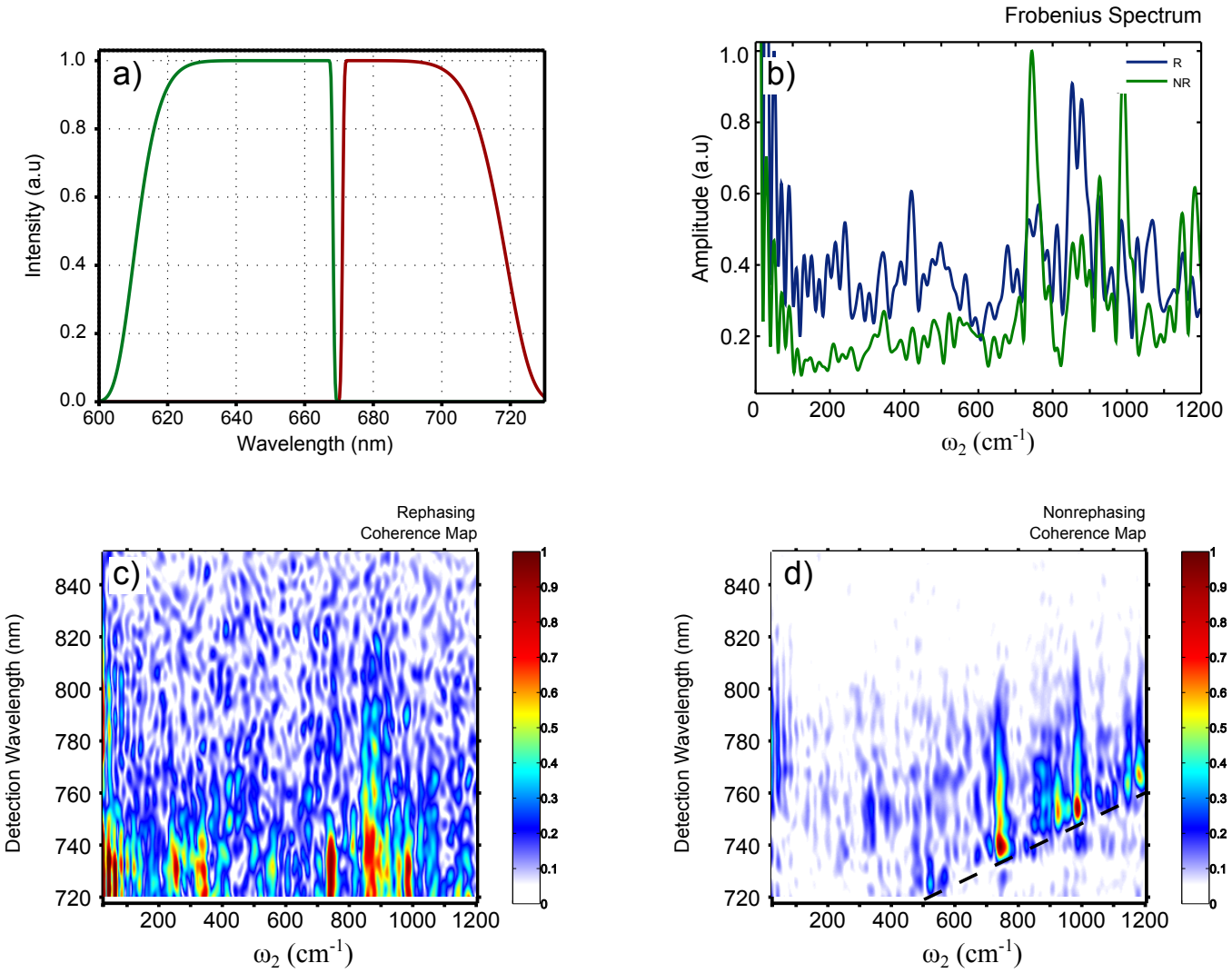

Figure 5.16: a) The amplitude shapes used to create pump pulses in TRACS to excite multiple modes. b) Frobenius spectrum calculated for the rephasing (blue) and the nonrephasing signal (green). c) The Rephasing coherence map showing the distribution of amplitude of coherences as a function of detection wavelength. The regions with less than 0.05 peak amplitude is set to shown as white. d) The Nonrephasing coherence map showing the distribution of amplitude of coherences as a function of detection wavelength. The regions with less than 0.05 peak amplitude are set to shown as white.

References

[1] Michael R. Wasielewski, Douglas G. Johnson, Michael Seibert, and Govindjee. Determination of the primary charge separation rate in isolated photosystem ii reaction centers with 500-fs time resolution. *Proceedings of the National Academy of Sciences of the United States of America*, **86**:524–528, (1989).

[2] I. Fujita, M. S. Davis, and J. Fajer. Anion radicals of pheophytin and chlorophyll a: their role in the primary charge separations of plant photosynthesis. *Journal of the American Chemical Society*, **100**:6280–6282, (1978).

[3] Scott R. Greenfield and Michael R. Wasielewski. Excitation energy transfer and charge separation in the isolated photosystem ii reaction center. *Photosynthesis Research*, **48**:83–97, (1996).

[4] M. S. Davis, A. Forman, and J. Fajer. Ligated chlorophyll cation radicals: Their function in photosystem ii of plant photosynthesis. *Proceedings of the National Academy of Sciences of the United States of America*, **76**:4170–4174, (1979).

[5] Michael R. Wasielewski, Douglas G. Johnson, Govindjee, Christopher Preston, and Michael Seibert. Determination of the primary charge separation rate in photosystem ii reaction centers at 15 k. *Photosynthesis Research*, **22**:89–99, (1989).

[6] John N. Gehlen, Massimo Marchi, and David Chandler. Dynamics affecting the primary charge transfer in photosynthesis. *Science*, **263**:499–502, (1994).

[7] Koji Ando and Hitoshi Sumi. Nonequilibrium oscillatory electron transfer in bacterial photosynthesis. *The Journal of Physical Chemistry B*, **102**:10991–11000, (1998).

[8] Vladimir I. Novoderezhkin, Andrey G. Yakovlev, Rienk van Grondelle, and Vladimir A. Shuvalov. Coherent nuclear and electronic dynamics in primary charge separation in photosynthetic reaction centers: a redfield theory approach. *The Journal of Physical Chemistry B*, **108**:7445–7457, (2004).

[9] Haiyu Wang, Su Lin, James P. Allen, JoAnn C. Williams, Sean Blankert, Christa Laser, and Neal W. Woodbury. Protein dynamics control the kinetics of initial electron transfer in photosynthesis. *Science*, **316**:747–750, (2007).

[10] Franklin D. Fuller, Jie Pan, Andrius Gelzinis, Vytautas Butkus, S. Seckin Senlik, Daniel E. Wilcox, Charles F. Yocum, Leonas Valkunas, Darius Abramavicius, and Jennifer P. Ogilvie. Vibronic coherence in oxygenic photosynthesis. *Nature Chemistry*, **6**:706–711, (2014).

Chapter 6

Conclusion and Outlook

Former studies in our group reported 2DES studies of the PSII RC, focusing on the energy and charge transfer dynamics,and coherent dynamics [1–3]. In this dissertation, I have presented my work to improve detection, characterization, and understanding of the functionality of coherent dynamics in the PSII RC. First, I performed 2DES on Chl a and the PSII RC to examine similarities and differences between three dominant coherent modes observed in both systems. I observed that the low frequency modes in the PSII RC exhibit vibronic character while the high frequency one exhibits largely vibrational character. My observations of the coherent dynamics in Chl a showed that there are deviations from previously proposed models which expects a "chair" shape for coherence maps. Additionally, theoretical simulations have supported our observations in both systems.

Secondly, I developed a novel method (T-RACS) which is based on pulse shaping to record coherent dynamics in complex systems. T-RACS decreases the total experiment time and increases the signal to noise ratio for the detection of coherent dynamics. I showed that the T-RACS method can distinguish features associated with the ground and the excited state by employing appropriate pulse sequences. Additionally, the decrease in total experiment time allowed me to record coherent dynamics at longer waiting times; and subsequently to determine the excited and ground state frequencies with higher resolution. This achievement gave T-RACS benefits over FLN of enabling measurements over a broad temperature range [4]. We proposed that a combination of T-RACS and 3DES may be more effective to observe coherent dynamics in systems where the coherent obser-

vation have not previously been reported. Although T-RACS is a lower dimensional measurement, the reduction in total experiment time and enhanced signal to noise ratio made it a valuable tool to study the role of coherent dynamics in the photosynthetic systems.

Finally, I studied the 790-820 nm spectral region of the PSII RC, which has anion band markers of charge separation, by utilizing the transient absorption spectroscopy and T-RACS. These studies are the first frequency resolved transient absorption measurement of the PSII RC in this region followed by the excitation of the Q_y band. The dynamics I have observed can be explained by the overlap of excited state absorption of Chl a and the formation of the markers of charge separation [5]. While our observations show deviations from earlier reports, the difference in excitation conditions (e.g. pump wavelength, power, experiment temperature) might explain this difference; and further experimental studies are planned to investigate this region in more detail. I have performed successive T-RACS measurements to examine coherent dynamics in the anion band. The first set of T-RACS experiments employed pulse sequences to selectively excite specific coherence pathways which are close to several central frequencies: 250 cm^{-1}, 350 cm^{-1}, 450 cm^{-1}, 550 cm^{-1}, 650 cm^{-1}, 750 cm^{-1}, 850 cm^{-1}, 950 cm^{-1}, 1050 cm^{-1}. These experiments revealed the existence of coherent dynamics in a broad spectral range from 720 nm to 820 nm. While the intensity of the observed modes changes dramatically along the detection axis, ~750 cm^{-1} and ~950 cm^{-1} modes exhibit larger amplitude in the 790-820 nm range compared to other modes. I also extended the narrow band pump pulse approach in T-RACS, and employed pump pulses with broader bandwidths, while ensuring that there was no spectral overlap between pump pulses. This extension enabled us to excite all the modes simultaneously while suppressing population dynamics. We have observed the coherent dynamics with higher S/N in this approach. We note that the observation of coherent dynamics in this spectral range do not guarantee their functional role in charge separation. Further studies to separate the overlapping spectral contribution in this band are needed to properly assign the coherent dynamics. Control studies of Chl a in the 790-820 nm region may help in this regard.

The work presented in this thesis answers some of the question about the coherent dynamics in the PSII RC and describes a novel method to study them. Further experimental and theoretical

work should be done to confirm the results here and answer remaining open questions. The comparison of coherent dynamics in the PSII RC and Chl a could be extended by performing 2DES measurements on other major bands. For example, the anion band at ~460 nm could also help to corroborate our near-IR anion band work. The effect of temperature on the phase of the coherent dynamics could be used to the study origin of these peaks as recently suggested [6]. The 2DES experiments with different polarization schemes which requires some modifications to our current setup, could enhance the our capabilities to investigate coherent dynamics. The 2DES studies on other aggregates of Chl a as well as the PSII core complex could form a valuable amount of information where we can see how certain features changes from the monomer level to the higher complex molecular level. Additionally, the comparison study could also be extended by utilizing T-RACS. Although we have observed coherence in the Q_y band of the PSII RC and the Chl a, T-RACS studies could yield frequency content information with higher resolution, and additional insight into origin of the peaks.

Finally, the functional relevance of the coherent dynamics may be explored by the use of site directed mutants of the PSII RC. It may be possible, by comparing the coherent dynamics of an array of mutants with different charge separation quantum yields, to correlate the presence of coherent dynamics with more or less effective charge separation.

The experimental verification of the functional importance of the observed coherent modes still remains a challenge. Follow up experiments focusing on the coherent dynamics of Chl a in the 700-900 nm spectral range may help us better understand coherent dynamics we observed in this region. A coherent control experiment can be used to study the functionality of the coherent modes. In these experiments, a pulse train in which consecutive pulses are separated by the period of the coherent mode of interest preferentially drive the system and the population of the photo product state is probed [7, 8]. The change in the kinetics of the product state according to pulse spacing in the pulse train could help our understanding on the functionality of the modes. However the existence of exited state absorption in the same spectral range will still make the interpretation of the signal difficult as the pulse train can cause similar spectral changes in the ESA of Chl a.

References

[1] Franklin D. Fuller, Jie Pan, Andrius Gelzinis, Vytautas Butkus, S. Seckin Senlik, Daniel E. Wilcox, Charles F. Yocum, Leonas Valkunas, Darius Abramavicius, and Jennifer P. Ogilvie. Vibronic coherence in oxygenic photosynthesis. *Nature Chemistry*, **6**:706–711, (2014).

[2] Kristin L. M. Lewis and Jennifer P. Ogilvie. Probing photosynthetic energy and charge transfer with two-dimensional electronic spectroscopy. *Journal of Physical Chemistry Letters*, **3**:503–510, (2012).

[3] Jeffrey A. Myers, Kristin L. M. Lewis, Franklin D. Fuller, Patrick F. Tekavec, Charles F. Yocum, and Jennifer P. Ogilvie. Two-dimensional electronic spectroscopy of the d1-d2-cyt b559 photosystem ii reaction center complex. *The Journal of Physical Chemistry Letters*, **1**: 2774–2780, (2010).

[4] S. Seckin Senlik, Veronica R. Policht, and Jennifer P. Ogilvie. Two-color nonlinear spectroscopy for the rapid acquisition of coherent dynamics. *The Journal of Physical Chemistry Letters*, **6**:2413–2420, (2015).

[5] Scott R. Greenfield and Michael R. Wasielewski. Excitation energy transfer and charge separation in the isolated photosystem ii reaction center. *Photosynthesis Research*, **48**:83–97, (1996).

[6] Vclav Perlk, Craig Lincoln, Frantiek anda, and Jrgen Hauer. Distinguishing electronic and vibronic coherence in 2d spectra by their temperature dependence. *The Journal of Physical Chemistry Letters*, **5**:404–407, (2014).

[7] Erik M. Grumstrup, Justin C. Johnson, and Niels H. Damrauer. Enhanced triplet formation in polycrystalline tetracene films by femtosecond optical-pulse shaping. *Physical Review Letters*, **105**:257403, (2010).

[8] Richard S. Judson and Herschel Rabitz. Teaching lasers to control molecules. *Physical Review Letters*, **68**:1500–1503, (1992).